LEVEL II

①

REPORT DOCUMENTATION PAGE	READ INSTRUCTIONS BEFORE COMPLETING FORM

1. REPORT NUMBER 80-3D	2. GOVT ACCESSION NO. AD-A092 459	3. RECIPIENT'S CATALOG NUMBER

4. TITLE (and Subtitle) A Cylindrical Cloud Model for Microwave and Infra-red Radiative Transfer-Applications to Defense Meteorological Satellite Program Microwave Sounders	5. TYPE OF REPORT & PERIOD COVERED THESIS/DISSERTATION
	6. PERFORMING ORG. REPORT NUMBER

7. AUTHOR(s) Grant Clifford Aufderhaar	8. CONTRACT OR GRANT NUMBER(s)

9. PERFORMING ORGANIZATION NAME AND ADDRESS AFIT STUDENT AT: The University of Utah	10. PROGRAM ELEMENT, PROJECT, TASK AREA & WORK UNIT NUMBERS

11. CONTROLLING OFFICE NAME AND ADDRESS AFIT/NR WPAFB OH 45433	12. REPORT DATE March 1980
	13. NUMBER OF PAGES 147

14. MONITORING AGENCY NAME & ADDRESS(if different from Controlling Office)	15. SECURITY CLASS. (of this report) UNCLASS
	15a. DECLASSIFICATION DOWNGRADING SCHEDULE

16. DISTRIBUTION STATEMENT (of this Report)

APPROVED FOR PUBLIC RELEASE; DISTRIBUTION UNLIMITED

DTIC
DEC 0 4 1980
E

17. DISTRIBUTION STATEMENT (of the abstract entered in Block 20, if different from Report)

18. SUPPLEMENTARY NOTES

APPROVED FOR PUBLIC RELEASE: IAW AFR 190-17

FREDRIC C. LYNCH, Major, USAF
Director of Public Affairs

Air Force Institute of Technology (ATC)
Wright-Patterson AFB, OH 45433

19. KEY WORDS (Continue on reverse side if necessary and identify by block number)

20. ABSTRACT (Continue on reverse side if necessary and identify by block number)

ATTACHED

AD A092439

DDC FILE COPY

ABSTRACT

Analytic solutions to the thermal radiative transfer equation for one and two-dimensional cylindrical geometries for an isothermal cloud cylinder are derived using a truncated spherical harmonics expansion for the intensity and scattering phase function. Higher order approximations are generated by utilizing the recursion properties of the modified Bessel functions. Computational results are presented and physically discussed for a hypothetical atmosphere in the infrared 10 μm wavelength and in a realistic atmosphere in the microwave 50-60 GHz frequencies. Comparisons are made with a discrete-ordinate plane-parallel model and finite cubic and rectangular models in the infrared region and with a discrete-ordinate plane-parallel model in the microwave region. Results demonstrate that finite clouds have emissivities less than those of plane-parallel clouds and that optically thick cylindrical clouds should not be considered as black clouds. Further, the effect of the angle of observation of the satellite on remote sensing of a cloud pattern is demonstrated to be significant. Case studies are presented utilizing Defence Meteorological Satellite Program microwave sounder data along with standard meteorological data. Calculations for nonprecipitating and clear cases were similar and in good agreement with observations. Precipitating cloud cases were simulated well by the cylinder model, while the plane-parallel model failed in cases with higher rainfall rates.

Finally, temperature profile retrievals were performed using the Air Force Global Weather Central statistical method. The method was shown to fail in case studies where there was a precipitating cloud in the field of view.

A CYLINDRICAL CLOUD MODEL FOR MICROWAVE AND INFRARED RADIATIVE

TRANSFER-APPLICATIONS TO DEFENSE METEOROLOGICAL SATELLITE

PROGRAM MICROWAVE SOUNDERS

by

Grant Clifford Aufderhaar

A dissertation submitted to the faculty of The
University of Utah in partial fulfillment of the requirements
for the degree of

Doctor of Philosophy

Department of Meteorology

The University of Utah

March 1980

THE UNIVERSITY OF UTAH GRADUATE SCHOOL

SUPERVISORY COMMITTEE APPROVAL

of a dissertation submitted by

GRANT CLIFFORD AUFDERHAAR

I have read this dissertation and have found it to be of satisfactory quality for a doctoral degree.

_____Jan. 9, 1980_____   _____
Date

Kuo-Nan Liou
Chairman, Supervisory Committee

I have read this dissertation and have found it to be of satisfactory quality for a doctoral degree.

_____Jan. 9, 1980_____   _____
Date

S. K. Kao
Member, Supervisory Committee

I have read this dissertation and have found it to be of satisfactory quality for a doctoral degree.

_____Jan 9, 1980_____   _____
Date

Frank Stenger
Member, Supervisory Committee

I have read this dissertation and have found it to be of satisfactory quality for a doctoral degree.

_____Jan 9, 1980_____   _____
Date

Elford G. Astling
Member, Supervisory Committee

I have read this dissertation and have found it to be of satisfactory quality for a doctoral degree.

_____Jan. 9, 1980_____   Peter Barber (KNL)
Date

Peter W. Barber
Member, Supervisory Committee

18c
9-78

$\zeta_\smile - 3\,\mathbb{D}$

The purpose of this questionnaire is to ascertain the value and/or
contribution of research accomplished by students or faculty of the
Air Force Institute of Technology (ATC). It would be greatly appreciated
if you would complete the following questionnaire and return it to:

AFIT/NR
Wright-Patterson AFB OH 45433

Research Title: A Cylindrical Cloud Model for Microwave and Infra-
red Radiative Transfer-Applications to Defense Meteorological
Satellite Program Microwave Sounders

Author: Grant Clifford Aufderhaar

Research Assessment Questions:

1. Did this research contribute to a current Air Force project?

    a.   Yes   b.   No

2. Do you believe this research topic is significant enough that it would
have been researched (or contracted) by your organization or another agency
if AFIT had not?

    a.   Yes   b.   No

3. The benefits of AFIT research can often be expressed by the equivalent
value that your agency achieved/received by virtue of AFIT performing the
research. Can you estimate what this research would have cost if it had
been accomplished under contract or if it had been done in-house in terms
of manpower and/or dollars?

    a.   Man-years _____.   b. $_____

4. Often it is not possible to attach equivalent dollar values to research,
although the results of the research may, in fact, be important. Whether or
not you were able to establish an equivalent value for this research (3 above),
what is your estimate of its significance?

    2. Highly   b. Significant   c. Slightly   d. Of No
       Significant   Significant   Significance

5. AFIT welcomes any further comments you may have on the above questions,
or any additional details concerning the current application, future potential,
or other value of this research. Please use the back of this questionnaire
for your statement(s).

NAME   GRADE   POSITION

ORGANIZATION   LOCATION

USAF SCN 75-20B

THE UNIVERSITY OF UTAH GRADUATE SCHOOL

FINAL READING APPROVAL

To the Graduate Council of The University of Utah:

I have read the dissertation of _____ GRANT CLIFFORD AUFDERHAAR _____ in its
final form and have found that (1) its format, citations, and bibliographic style are
consistent and acceptable; (2) its illustrative materials including figures, tables, and
charts are in place; and (3) the final manuscript is satisfactory to the Supervisory
Committee and is ready for submission to the Graduate School.

Jan. 9, 1980
Date

Kuo-Nan Liou
Member, Supervisory Committee

Approved for the Major Department

S. K. Kao
Chairman/ Dean

Approved for the Graduate Council

James L. Clayton
Dean of The Graduate School

TABLE OF CONTENTS

Table of Contents (continued)

LIST OF TABLES

LIST OF FIGURES

List of Figures (continued)

List of Figures (continued)

.

xi

ACKNOWLEDGEMENTS

I wish to express my deepest gratitude to Professor Kuo-Nan Liou for his invaluable assistance, guidance, and encouragement during the course of this study. Also, I would like to acknowledge the contribution of Dr. Szu-Cheng Ou toward the successfull completion of the present research. Special thanks go to the other members of my graduate committee, Professor Shih-Kung Kao, Dr. Peter Barber, Dr. Elford Astling and finally to Professor Frank Stinger whose inspiration provided me the wherewithall to attempt a project of this sort.

My appreciation also goes to Major Richard Savage and Captain Joseph Gahlingher of AFGWC for providing the SSM/T microwave data used in this study.

My fellow students have been a constant source of encouragement and inspiration during my stay at the University of Utah. I would especially like to single out my good friends Fred Lewis, Gerard Wittman, Paul Nipko, Hwa-Young Yeh, Dave McLawhorn, Rich Coleman, Ed Tomlinson and Ashton Peyrefitte. I would also like to thank Robert Feddes whose patience and knowledge were of indeterminable help during these studies, and Kristi Gebhart for her diligent help and work at the conclusion of this effort.

I must mention and thank Lt. Col. Robert DeMichaels and Lt. Col. Ronald Tudor and Dr. Robert Clark for their inspiration at the beginning and during my meteorological career.

Finally, the support of my family has never waned during these past years. My Father and Mother, Norman and Eleanor Aufderhaar and my sister and brother, Susan and Conrad have stuck with me through all my trials and tribulations.

I wish to express my deepest gratitude to my wife, Linda, for her love, understanding, and support during the many difficult times which arose in the course of my research.

CHAPTER 1

INTRODUCTION

In recent years, one of the unresolved problems in the fields of atmospheric radiation and satellite sensing has been the transfer of radiation in finite cloud layers in conjunction with the interpretation of satellite sounding data. Additional problems include the development of sounding techniques for cloud inference, and the understanding of the generation of heating and cooling in the atmosphere. There are many circumstances in the Earth's atmosphere by which finite clouds and cloud bands are formed. Inference of the composition and structure of clouds and the atmosphere utilizing satellite sounding techniques requires a comprehensive understanding of the interaction of these finite cloud layers with the radiation field of atmosphere.

Several recent studies have been carried out to investigate the transfer of radiation in finite clouds using cartesian coordinates. McKee and Cox (1976), Davies (1978), and Davis et. al. (1979) reported the significant effect of the cubic geometry on the reflection, transmission and absorption of solar radiation. Weinman and Davies (1978) investigated the cubic geometry influence on the transfer of microwave radiation at a frequency of 37 GHz. More recently, Liou and Ou (1979), using an infrared window wavelength of 10 μm, found that finite geometry significantly affects cloud emissivity and infrared cooling rates. None of these studies, however, have applied the

finite cloud transfer model to realistic atmospheres which include the absorption contribution of atmospheric gases and actual satellite sounding problems in which observed data are available. Moreover, transfer of radiation in coordinate systems other than rectangular has not been theoretically explored and investigated in atmospheric remote sounding and radiative transfer problems.

The first objective of this study is to develop a theoretical finite cloud model using a cylindrical geometry applicable to frequently occurring cloud and precipitation bands in the microwave and infrared radiation regions and to apply the cylindrical model to realistic atmospheric conditions. The second objective is to modify the cylindrical cloud/precipitation model to interpret the observed brightness temperatures sensed by the DMSP (Defense Meteorological Satellite Program) microwave sounder (SSM/T) which was launched in June, 1979, for carefully selected clear, cloudy and precipitating cases. In connection with these cases and depending on the availability of radiosonde temperature profiles, temperature retrieval exercises based on the observed brightness temperatures are carried out utilizing a statistical method.

The initial impetus for radiative transfer in cylindrical geometry was provided by Mark (1945) in the solution in the neutron transport or Boltzman equation. From Mark's work, investigation was begun in the neutron transport field in a number of different geometries. The spherical harmonics approach for the Boltzman equation in a one-dimensional cylindrical medium was investigated by Davison (1957) and Kofink (1959). Heasley and Warming (1966) applied a moment method to the one-dimensional cylindrical problem in

radiative transfer, and Heasley (1977) formulated the transfer equation as a second-order differential equation resulting in a set of tridiagonal difference equations. The work presented in this dissertation more directly follows the lead presented by Kofink (1959) in the neutron transport field, applying a modification of his method to one-dimensional cylindrical radiative transfer. Radiative transfer in a two-dimensional cylindrical medium is then developed for various orders of approximation.

In Chapter 2, the detailed characteristics of the DMSP microwave radiometer (SSM/T) are presented. Chapter 3 is devoted to an analysis of the optical parameters peculiar to the frequencies used by the SSM/T. In Chapter 4, thermal radiative transfer in plane-parallel atmospheres utilizing the discrete-ordinate method is reviewed briefly. Chapter 5 reports the theoretical development for radiative transfer in cylindrical media, utilizing a spherical harmonics approach. Chapter 6 presents computational results utilizing the two-dimensional cylindrical model. Comparisons are made with results presented by Liou and Ou (1979) using the infrared 10 um window region for cubic and rectangular cloud models. Comparisons are also made with results reported by Nipko (1979) using the microwave 60 GHz SSM/T frequencies for the plane-parallel model. In Chapter 7, data sets, which include the SSM/T microwave sounder data and conventional meteorological data, are chosen for two days. By employing the temperature and humidity profiles and/or cloud information, radiative transfer calculations are carried out and compared with observed satellite data. Finally, temperature profile retrievals are performed using a statistical method.

CHAPTER 2

DMSP BLOCK 5D SSM/T SOUNDER CHARACTERISTICS

The SSM/T microwave scanning radiometer was launched in June, 1979, in a sun-synchronous polar orbit, by the U. S. Air Force as part of the Defense Meteorological Satellite Program (DMSP) Block 5D package. Other equipment of meteorological interest on board the spacecraft include visual and infrared imagery channels and a scanning infrared spectroradiometer. The microwave instrument scans across the track of the satellite (Figure 1), sensing a near circle of 174 km diameter at nadir, and an ellipse with a major axis of 304 km and minor axis of approximately 213 km at maximum scan angle (Figure 2) of 36° from nadir. The scan parameter information in Table 1 may be used in conjunction with Figure 2 to visualize how the sounder "sees" the earth-atmosphere system as it moves along its track. Seven operational frequencies (Table 2) were chosen in the vicinity of a strong oxygen absorption band near 60 GHz, so that the weighting functions associated with the various channels peak at different altitudes within the Earth's atmosphere, thus providing sufficient vertical resolution for temperature profile retrieval. Channel 1, 50.50 GHz, is a "window" channel and senses at or near the Earth's surface. Channels 2, 3 and 4 (53.20, 54.35 and 54.90 GHz) have weighting functions that peak at increasing heights in the troposphere. The weighting functions of Channels 5, 6 and 7 peak in the stratosphere with Channel 5 peaking
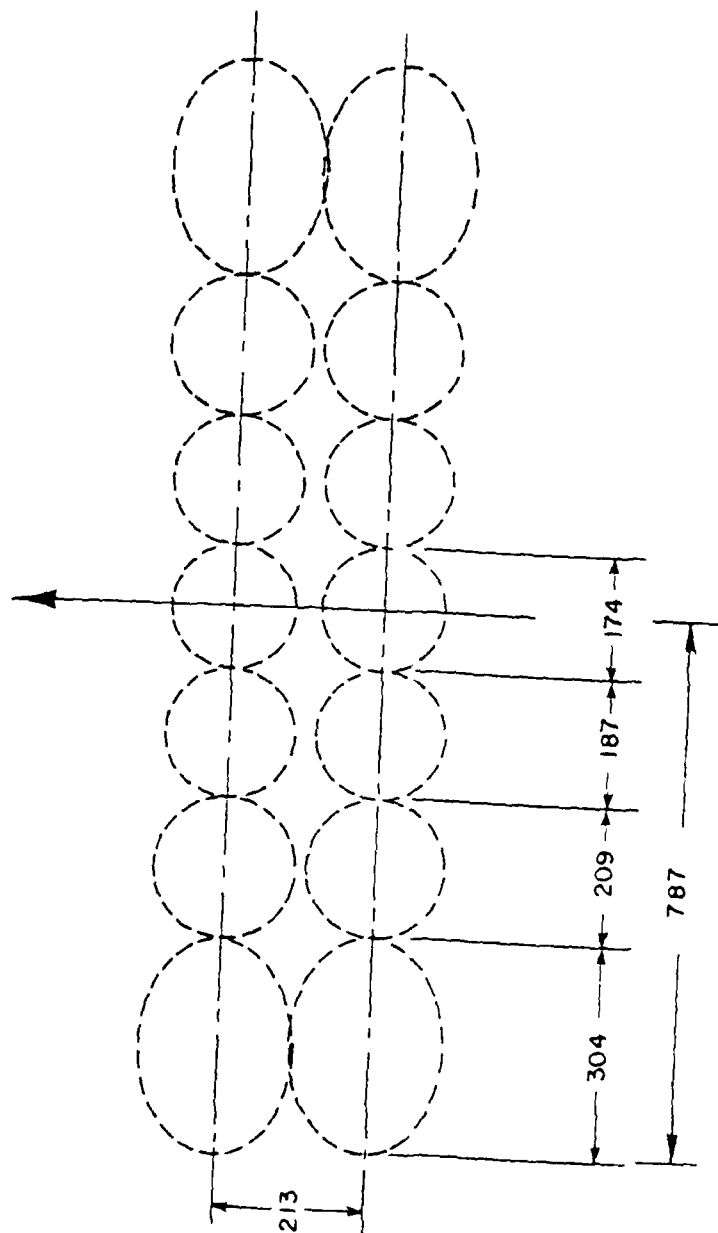
Figure 1. SSM/T subtrack scan pattern.
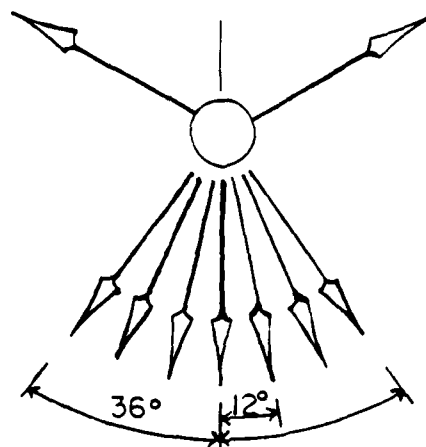
Figure 2. SSM/T Scan Geometry. Source: Rigone and Stogryn (1977)

Table 1. Scan Parameters

Scan Type	Cross-Track Nadir
Cross-Track Positions	7
Calibration Positions	2-Cold Space and 300°K
Instantaneous Field of View	14°
Total Cross-Track Scan	36°
Total Scan Period	32 Seconds
Integration Time (Cross-Track and Calibration Positions) . . .	2.7 Seconds
Sync Mode	Auto Mode or On-Sync

Source: Rigone and Stogryn (1977)

Table 2.   Channel Parameter Design Specifications

Channel	Polarization	Frequency (GHz)	Bandwidth (MHz)	NETD (°K)
1		50.5	400	0.6
2	Principally Horizontal	53.2	400	0.4
3		54.35	400	0.4
4		54.9	400	0.4
5	Orthogonal to Channels 1-4	58.4	115	0.5
6		58.825	400	0.4
7		59.4	250	0.4

Source: Rigone and Stogryn (1977)

highest in the atmosphere near 28 km. The weighting functions result
from consideration of atmospheric absorption due to water vapor and
molecular oxygen and indicate the approximate location in the atmos-
phere from which we assume most of the energy in a particular fre-
quency, that reaches the top of the atmosphere, originates. The
weighting functions presented in Figure 3 also have transmissivity
corrections for antenna gain characteristics included, as described
by Nipko (1979).
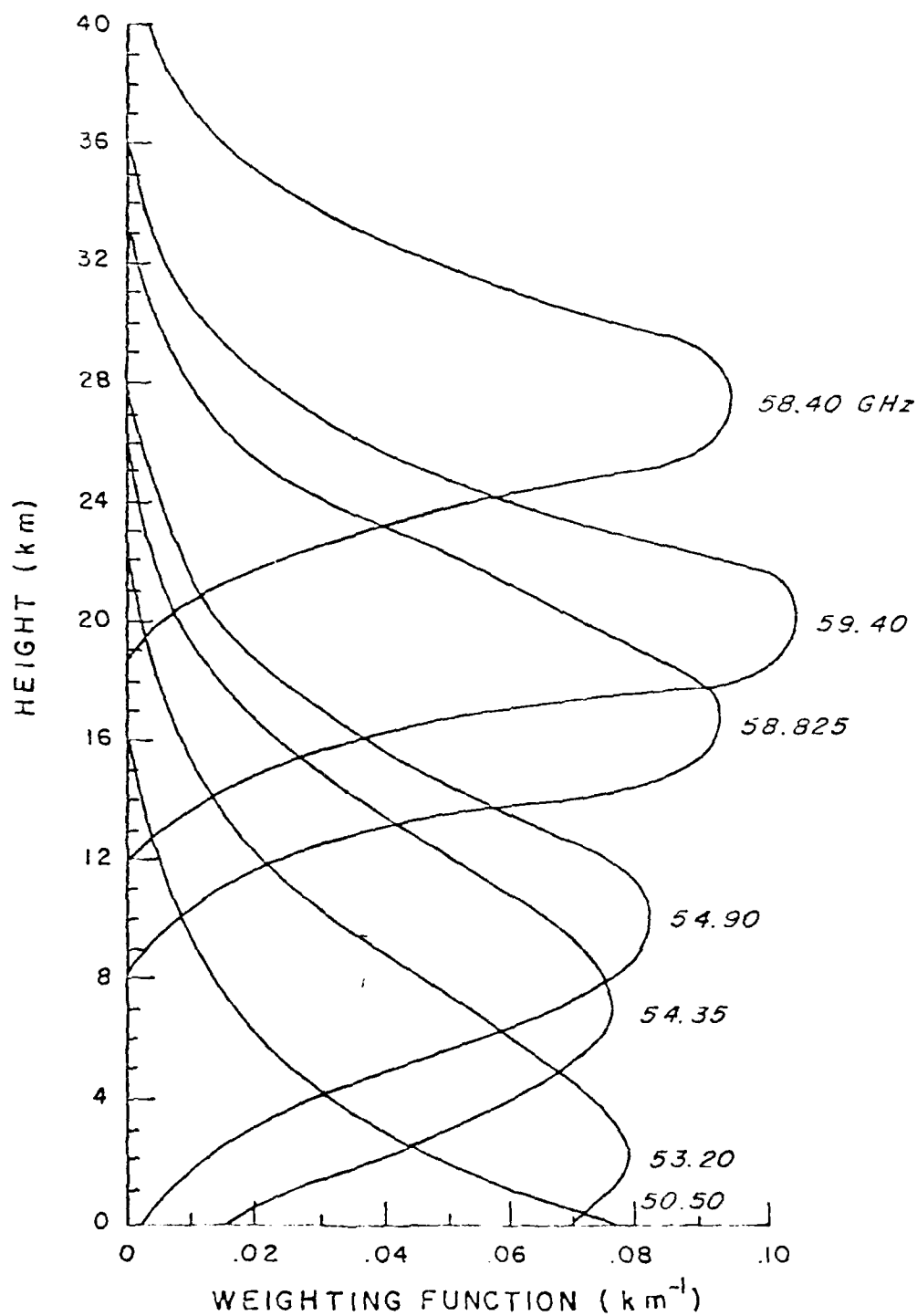
Figure 3. SSM/T weighting functions (nadir) with antenna gain characteristics included (ε=.97).

CHAPTER 3

ATMOSPHERIC OPTICAL PARAMETERS FOR SSM/T FREQUENCIES

Microwave frequencies between 50.0 and 60.0 GHz are gener-
ally considerably affected by several different atmospheric constitu-
ents. Gases in the atmosphere absorb and emit microwave radiation,
and liquid water, such as cloud droplets and rain, absorb, emit and
scatter radiation.

3.1 Gaseous Constituents

The primary gaseous absorbers in the microwave region are H_2O
vapor and O_2. Atmospheric nitrogen gradually becomes a more signifi-
cant absorber at frequencies greater than 120 GHz, but has little in-
fluence in the vicinity of 60 GHz. Other gaseous constituents occur
in very low concentrations and, in general, their effects are very
small.

The O_2 absorption spectrum in the microwave region is due to the
molecule's magnetic dipole moment. Figure 4 presents the absorption
coefficient of dry air versus frequency. The absorption coefficient
(decibels/km) shows a dramatic peak near 60 GHz and a secondary maxi-
mum near 120 GHz. Both peaks are attributable to molecular oxygen.
The characteristics of this absorption spectrum were first investigated
by Van Vleck during World War II and were published in 1947. Other
investigators have built on his studies (a detailed biography was pre-
sented by Rosenblum (1961)), culminating in a paper by Meeks and
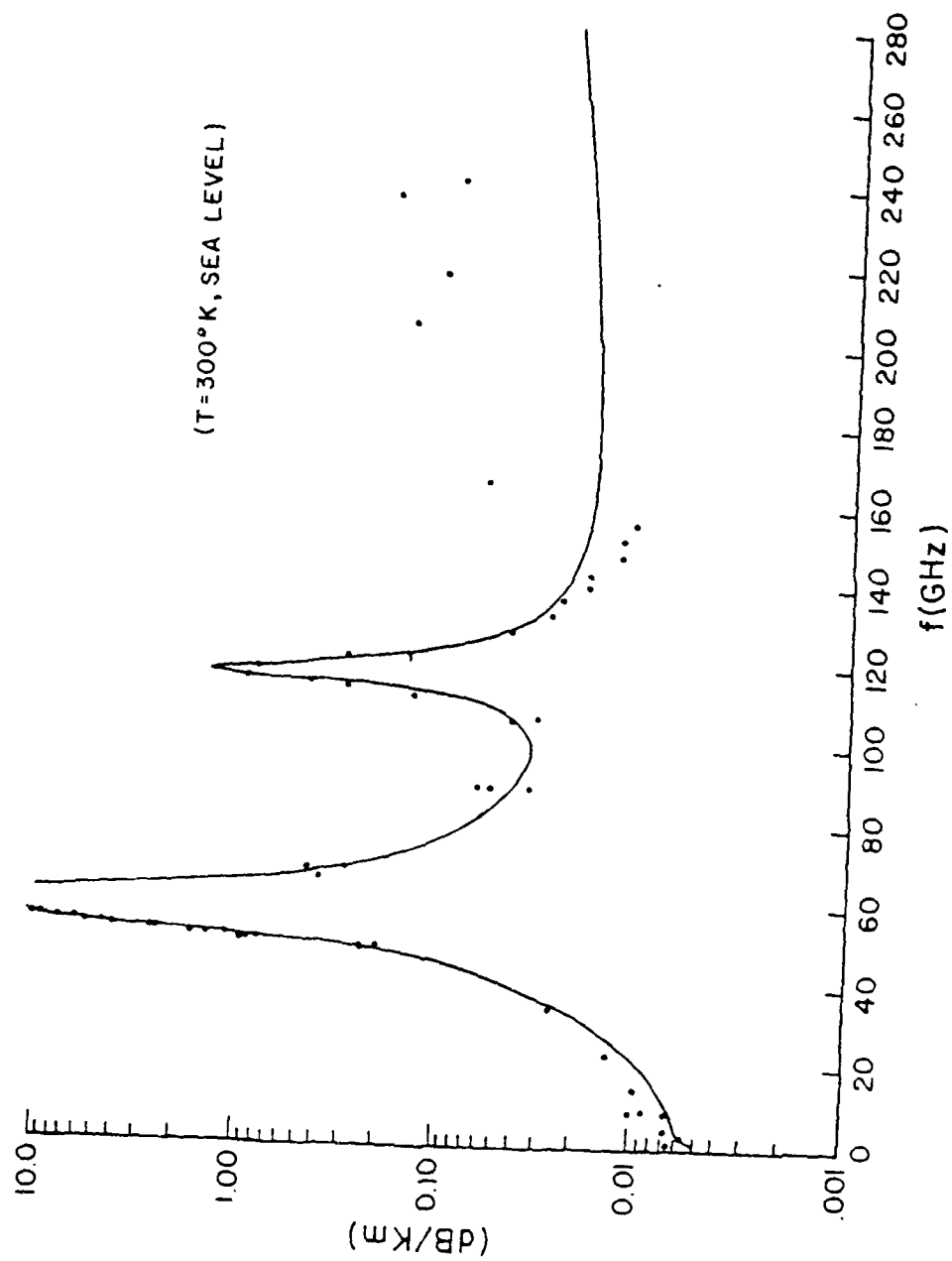
Figure 4. Absorption coefficient of dry air.

Lilley (1963). For this study, the absorption coefficients for O_2 were calculated using Meeks and Lilley parameters.

Figure 5 presents water vapor absorption (dB/km) versus frequency in the microwave region. You can see that the values of absorption increase gradually through the range of frequencies under investigation. It is apparent that the absorption due to water vapor is less than that of molecular oxygen for all the channels chosen for the SSM/T sounder. Note, however, that even though the oxygen coefficient is higher, the two values are roughly equivalent for the window channel (50.50 GHz).

Studies of water vapor absorption (due to an electric dipole moment), (see Figure 5), again, have their roots in World War II projects. Initial studies were published by Van Vleck (1947), Becker and Autler (1946), and King, et al. (1947). Rosenblum's article gives an excellent summary of work done up to 1961. H_2O vapor absorption coefficients were calculated using the method of Barrett and Chung (1962). Computer programs for determination of both of these coefficients were kindly provided by Falcone (personal communication).

3.2 Cloud Droplets and Rain

Mie (1908) found an exact solution for the scattering and absorption due to homogeneous spherical particles, given the complex index of refraction, wavelength of the incident radiation and the particle size. Although larger rain drops are known to deviate somewhat from the spherical shape, Mie's results still enjoy widespread popularity and use, and remain probably the best currently available theoretical
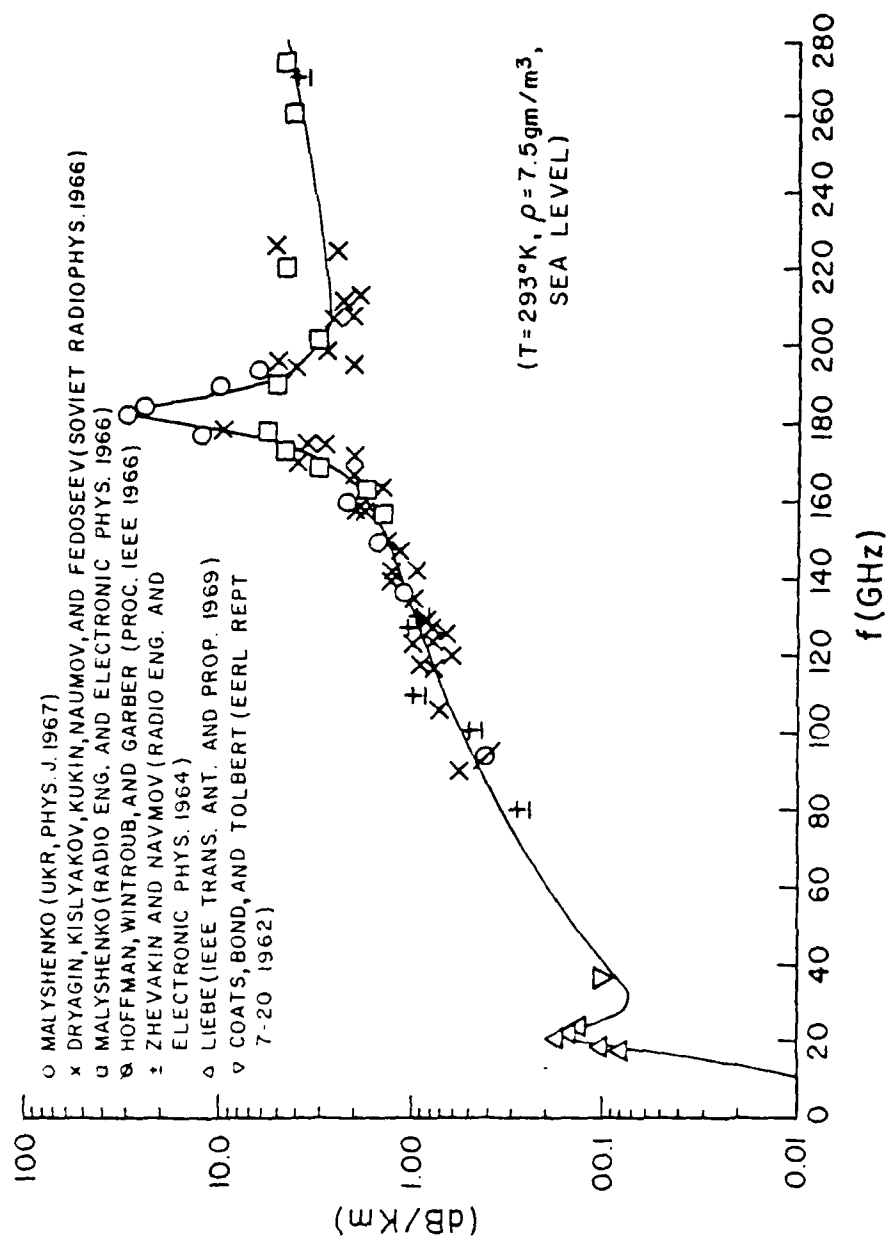
Figure 5. Water vapor absorption.

tool for analyzing the effects of cloud droplets and rain in the atmosphere. The Mie results have been adapted for computer use and the program used for these calculations is a modification for a Univac system of the program developed by Liou and Hansen (1971). Outputs of the program are β_e, the extinction coefficient (km^{-1}), $\tilde{\omega}_\nu$, the single scattering albedo, and the coefficients of the Legendre polynomial approximation to the phase function. It is important to recall that the extinction coefficient and single scattering albedo calculated by Mie's theory are due to condensed water only. These values are then modified to include effects of the gaseous atmosphere within the cloud prior to using them in the radiative transfer equations. Tables of the Lengendre polynomial phase function coefficients, extinction coefficients and single scattering albedos for each SSM/T channel were presented by Nipko (1979).

3.2.1 Indices of Refraction

Savage (1976) determined the complex indices of refraction (based on a least squares fit to the data of Saxton and Lane (1962) given by Hollinger (1973)) for pure liquid water at temperatures of +10° and -10° C for several frequencies (see Table 3). The indices of refraction for SSM/T channels (Table 4) were derived from Table 3 by linear interpolation (Nipko, 1979). 0° C values were used exclusively in this study.

3.3 Drop Size Distributions

Mie theory predicts the absorption and scattering cross sections for a single spherical particle. Various investigators have general-ized these results to those for a distribution of particles by

Table 3. Refractive Index $(m=m_r-im_i)$ of Pure Liquid Water

Frequency (GHz)	T=10°C		T=0°C		T=-10°C	
	m_r	m_i	m_r	m_i	m_r	m_i
19.35	5.87	2.96	5.20	2.94	4.64	2.81
37.00	4.32	2.60	3.83	2.37	3.46	2.12
50.30	3.76	2.29	3.37	2.03	3.08	1.78
89.50	3.00	1.67	2.76	1.42	2.60	1.20
100.00	2.89	1.56	2.68	1.31	2.54	1.10
118.00	2.75	1.39	2.58	1.15	2.46	0.96
130.00	2.68	1.30	2.53	1.07	2.43	0.89
183.00	2.49	1.00	2.39	0.81	2.33	0.66
231.00	2.40	0.82	2.33	0.66	2.29	0.53

After Savage (1976)

Table 4. Refractive Index of Pure Liquid Water (SSM/T)

	Channel Frequencies (GHz)						
	50.50	53.20	54.35	54.90	58.40	58.82	59.40
m_r	3.37	3.32	3.31	3.30	3.24	3.24	3.23
m_i	2.03	1.98	1.97	1.96	1.90	1.90	1.89

After Nipko (1979)

integrating over the distribution. This area per volume relationship has dimensions of inverse length and is called the scattering (or absorption of extinction) coefficient. Two models have been selected to represent clouds for the purpose of comparing with previous studies. Experimental data presented by Mason (1971) after results given by Dunn (1948) were used to provide a drop size distribution for non-precipitating clouds. The data used were for a cumulus congestus cloud. The second representation chosen was a cloud model developed by Marshall and Palmer (1948). This drop size distribution is written

$$N(r) = 0.16 \exp(-2r\delta) \tag{3-1}$$

where $\delta = 41 \ R^{-.21}$ and R denotes the rainfall rate in mm/hr. Gunnard and Marshall (1958), and Sekhon and Srivastaval (1970) have verified Marshall and Palmer's exponential expression based on raindrops and snowflakes collected during field experiments.

3.4 Atmospheric Profile and Cloud Models Used

The atmospheric profile used in this study was derived from the northern hemisphere mid-latitude Spring/Fall climatology contained in the U.S. Standard Atmospheric Supplements, 1966. The temperature and height values were interpolated to 40 standard pressure levels. Saturation mixing ratio values for levels below 250 mb were obtained from a Skew-T diagram. Mixing ratios above 250 mb were assumed to be a constant 3 parts per million. The Spring/Fall profile is presented in Figure 6.

A measure of the liquid water content in an atmosphere was obtained by the following means:
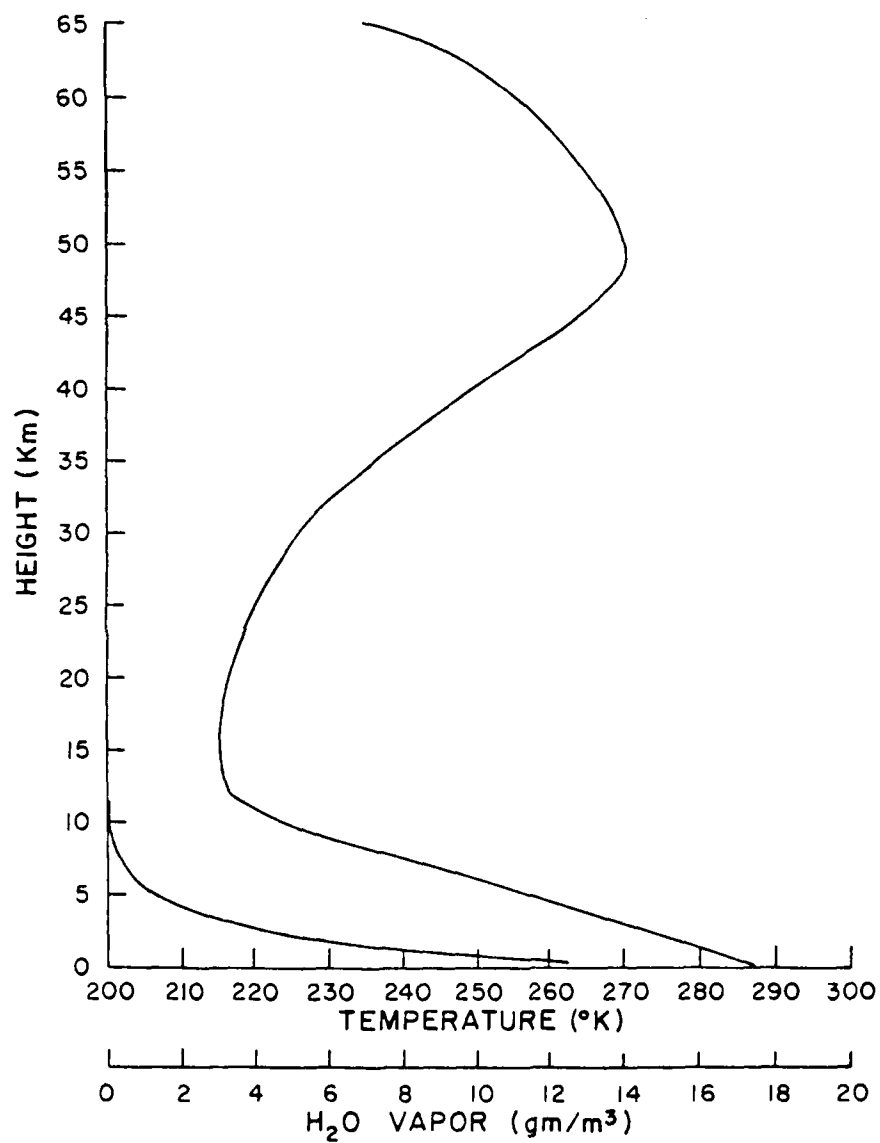
Figure 6. Northern hemisphere mid-latitude Spring/Fall profile.

1) for spherical particles the liquid droplet volume per unit volume of atmosphere is

$$V = \frac{4}{3} \pi \int_0^\infty r^3 N(r) dr .$$

(3-2)

Now we may express the liquid water content per unit volume of atmosphere as

$$W = \frac{4}{3} \pi \rho \int_0^\infty r^3 N(r) dr \quad gm\ cm^{-3}$$

(3-3)

where r is in cm, $N(r)$ is in cm^{-4}, and the density of liquid water is 1 gm cm^{-3}. W may be expressed for the two cloud models as

$$W = 1.16678 \times 10^{-2} \quad gm\ cm^{-2}\ km^{-1}$$

(3-4)

for the Diermendjian L-Model and

$$W = 1.77883 \times 10^{-2} \cdot R^{.84} \quad gm\ cm^{-2}\ km^{-1}$$

(3-5)

for the Marshall-Palmer model. Table 5 presents the total mass of liquid water within a column of 1 cm^2 cross sectional area for the cloud models used in the microwave comparison.

Table 5. Total Liquid Water Content (10^{-2} gm cm^{-2}).

Thickness (km)	1	2	3	4	5
Deirmendjian:	1.16678	2.33356	3.50034	4.66712	5.83390
Marshall-Palmer: R(mm/hr)					
1	0.88941	1.77882	2.66823	3.55764	4.44705
2	1.59209	3.18418	4.77627	6.36835	7.96044
3	2.23812	4.47625	6.71437	8.95249	11.1906
4	2.84992	5.69984	8.54975	11.3997	14.2496
5	3.43745	6.87491	10.3124	13.7498	17.1873
10	6.15321	12.3064	18.4596	24.6129	30.7661
15	8.65005	17.3001	25.9502	34.0020	43.2503
20	11.0146	22.0291	33.0437	44.0583	55.0728
25	13.2853	26.5706	39.8559	53.1412	66.4266
30	15.4840	30.9681	46.5421	61.9361	77.4201

CHAPTER 4

BRIEF REVIEW OF MICROWAVE RADIATIVE TRANSFER

IN A PLANE PARALLEL MEDIUM

4.1 Clear Column Calculations

The plane-parallel model assumes that the atmosphere is made up of many layers of infinite horizontal extent that are homogeneous and in local thermodynamic equilibrium. This atmosphere is necessarily axially symmetric about nadir-zenith. Also, for clear column brightness temperature calculations, there is no source of illumination at the top of the atmosphere.

The basic equation of transfer for an absorbing and emitting medium may be written as

$$\frac{dI_\nu}{k_\nu \rho ds} = -I_\nu + J_\nu, \qquad (4\text{-}1)$$

where I_ν is the intensity at frequency ν, k_ν is the absorption coefficient, ρ is density, J_ν is the source function, and S is the slant path. We change variables from ds to dz such that $ds=dz/\mu$, where z is height, $\mu = \cos\theta$, and θ is the zenith angle. The formal solution of Eq. (4-1) is given by

$$I_\nu(z) = I_\nu(0)e^{-\int_0^z k_\nu \rho dz'} + \int_0^z J_\nu(z')e^{\int_0^z k_\nu \rho dz'} k_\nu \rho dz' . \quad (4\text{-}2)$$

where $I_\nu(0)$ is the radiation source from the earth's surface. For convenience, we define the optical depth and transmittance, respectively,

as follows:

$$\tau(z',z) = \int_{z'}^{z} k_\nu \, \rho \, dz, \qquad (4\text{-}3)$$

$$T_\nu(z',z;\mu) = \exp[-\tau(z',z)/\mu]. \qquad (4\text{-}4)$$

These definitions allow us to rewrite Eq. (4-2) as

$$I_\nu(z) = I_\nu(0) \, T_\nu(0,z;\mu) + \int_{z'=0}^{z} J_\nu(z') \, dT_\nu(z',z;\mu) \qquad (4\text{-}5)$$

We may write Eq. (4-5) to represent the radiance reaching the top of the atmosphere as

$$I_\nu = I_\nu(0) \, T_\nu(0,\infty;\mu) + \int_{z'=0}^{\infty} J_\nu(z) \, dT_\nu(z',\infty) \qquad (4\text{-}6)$$

The source function, J_ν, for an atmosphere in local thermodynamic equilibrium may be represented by Planck's function. In the frequency domain, it is given by

$$B_\nu(T) = 2h\nu^3/[c^2(e^{h\nu/kT}-1)] \qquad (4\text{-}7)$$

where h is Planck's constant, c is the speed of light, and k is Boltzman's constant. In the microwave domain ($h\nu/KT \ll 1$), the Rayleigh-Jeans approximation to Planck's function is customarily used and therefore

$$\exp(h\nu/kT) \cong 1 + h\nu/kT . \qquad (4\text{-}8)$$

Consequently, Eq. (4-7) reduces to

$$B_\nu(T) = (\frac{2\nu^2 k}{c^2})\ T = c_\nu T \ . \qquad\qquad (4\text{-}9)$$

That is, given a frequency, the Planck function is directly proportional to the temperature. Moreover, analogous to Eq. (4-9) the equivalent brightness temperature may also be defined from the upwelling radiance in the form

$$I_\nu = c_\nu T_B(\nu) \ . \qquad\qquad (4\text{-}10)$$

In a clear atmosphere, radiance emitted at a level is isotropic and makes two contributions to the radiant energy reaching the top of the atmosphere. First, energy emitted in an upward direction travels directly to the top of the atmosphere, suffering a Beer's law attenuation due to the absorption by atmospheric gases along its path. Second, energy emitted in the downward direction is attenuated along its path to the surface. There, a percentage is reflected back upward and is again attenuated to the top of the atmosphere. Obviously, then, the contribution from the first description to intensity reaching the top of the atmosphere from height z is

$$T_B^d(\nu, z) = T(z) T_\nu(z, \infty; \mu) \qquad\qquad (4\text{-}11)$$

The latter contribution may be expressed as

$$T_B^r(\nu, z) = T(z)(1 - \varepsilon_\nu) T_\nu(0, \infty; \mu) T_\nu(0, z; \mu) \qquad (4\text{-}12)$$

Note T_B^d is the direct component of brightness temperature, T_B^r, the reflected, $T(z)$, the temperature at height z, and $T_\nu(z, \infty; \mu)$, the transmission from z to ∞ along path μ. ε_ν is the emissivity of the surface. The atmospheric contribution to microwave radiance reaching

the top of the atmosphere may be gotten by integrating Eqs. (4-11) and (4-12) and adding them together as

$$T_B^a(\nu) = \int_{z=0}^{\infty} T(z)\,dT_{\nu}(z,\infty;\mu) + (1-\varepsilon_{\nu})T_{\nu}(0,\infty;\mu)$$

$$\cdot \int_{z=0}^{\infty} T(z)\,dT_{\nu}(0,z;\mu) \quad . \tag{4-13}$$

There is one more contribution we must take into account. The surface of the Earth emits in the microwave region as a grey body, and the expression for this emission, attenuated to the top of the atmosphere is written

$$T_B^e(\nu) = \varepsilon_{\nu}T_s T_{\nu}(0,\infty;\mu), \tag{4-14}$$

where T_s is the surface temperature at $z=0$. The total brightness temperature at the top of the atmosphere may be written then as the sum of Eqs. (4-13) and (4-14) as

$$T_B(\nu) = \int_{z=0}^{\infty} T(z)\,dT_{\nu}(z,\infty;\mu) + (1-\varepsilon_{\nu})T_{\nu}(0,\infty;\mu) \int_{z=0}^{\infty} T(z)\,dT_{\nu}(0,z;\mu)$$

$$+ \varepsilon_{\nu}T_s T_{\nu}(0,\infty;\mu) \quad . \tag{4-15}$$

Eq. (4-15) yields the clear column brightness temperature at the top of the atmosphere. If the transmissivities have been adjusted for antenna gain characteristics, the Eq. (4-15) will give us what are commonly called "antenna temperatures". Note that we have carried along the dependence of the transmission on $\mu = \cos\theta$ (θ = zenith angle) throughout this discussion. However, in clear column discussions, θ is normally assumed to be zero degrees. We have kept the

nominal dependence for convenience in discussing the formulation of the clear atmosphere boundary conditions for the plane-parallel and cylinder cloud models.

4.2 Plane Parallel Model for Cloudy Atmospheres

The basic equation of transfer for a plane parallel cloud layer in local thermodynamic equilibrium can be written in the form:

$$\mu \frac{dI_\nu(\tau,\mu)}{d\tau} = I_\nu(\tau,\mu) - \frac{\tilde{\omega}_\nu}{2} \int_{-1}^{1} P_\nu(\mu,\mu') \, I_\nu(\tau,\mu') d\mu'$$

$$- (1-\tilde{\omega}_\nu) \, B_\nu(T(\tau)) \tag{4-16}$$

where I_ν represents the monochromatic radiance, μ the cosine of the emergent angle with respect to the zenith, τ the monochromatic optical depth, P_ν the normalized axially symmetric scattering phase function and $\tilde{\omega}_\nu$ the single scattering albedo. $B_\nu[T(\tau)]$ is the Planck function as defined by Eq. (4-7). The phase function can be expressed as a truncated series of Legendre polynomials. A Gauss-Legendre quadrature is used to replace the integration in Eq. (4-16). This allows us to derive a set of first order inhomogeneous differential equations. We seek homogeneous and particular solutions of the differential equations as outlined by Chandrasekhar (1950), and the complete solution of the scattered intensity from an isothermal cloud (temperature, T_c) for a given discrete stream, μ_i is expressed as

$$I_\nu(\tau,\mu_i) = \sum_m L_m \phi_m(\mu_i) \exp(-k_m \tau) + B_\nu(T_c) \tag{4-17}$$

where m is the number of discrete streams employed, ϕ_m and k_m represent eigenfunctions and eigenvalues for the differential equations

and the L_m are a set of constants determined from the radiation boundary conditions. Noting that the brightness temperature in the microwave range is simply the radiant intensity divided by a constant, Eq. (4-16) can also be written in terms of brightness temperature. The solution is then given by

$$T_B(\nu,\tau;\mu_i) = \sum_m L'_m \phi_m(\mu_i) \exp(-k_m\tau) + T_c \qquad (4-18)$$

where the constants L'_m, are different from those in Eq. (4-17), having been obtained using brightness temperature boundary conditions. T_c is the cloud layer temperature and is independent of frequency, ν.

At the cloud top, the downward brightness is equal to the brightness contributions from every point in the atmosphere above the cloud top attenuated by Beer's Law down to the cloud top. This can be expressed as

$$T_B(\nu,z_t;-\mu_i) = \int_{z=z_t}^{\infty} T(z)\,dT\,(z,z_t;-\mu_i) \qquad (4-19)$$

where z_t is the height at the cloud top and the negative sign on μ_i simply indicates downward transfer.

Within the cloud layer, where scattering occurs, continuity of brightness values from all directions is required. Thus

$$T_B(\nu,\tau_\ell;\mu_i) = T_B(\nu,\tau_{\ell+1};\mu_i) \quad \ell=1,2,\cdots N-1 \qquad (4-20)$$

where N is the total number of sublayers with the cloud.

At the lower boundary of the cloud, three brightness contributions are immediately apparent:

a) the surface contribution,

b) the direct atmospheric contribution from below the cloud, and

c) the reflected atmospheric contribution from below the cloud.
A fourth, and perhaps less obvious, brightness contribution at the
lower boundary must be considered for the cloud of infinite horizontal
extent (Nipko, 1979). Since the reflection of downward brightness by
the Earth's surface is significant for microwave radiation, the emer-
gent brightness at the cloud bottom will contribute to the lower
boundary condition. That is to say, the solution to the radiative
transfer through the cloud affects the boundary conditions used to
obtain the solution. Nipko (1979) suggested an iterative approach to
correct the lower boundary condition. If we include this additional
term, we may express the lower boundary condition as

$$T_3(\nu,z_b;\mu_i) = \varepsilon_s T_s T_\nu(0,z_b;\mu_i) + \int_{z=0}^{z_b} T(z) dT_\nu(z,z_b;\mu_i)$$

$$+ (1-\varepsilon_\nu) T_\nu(0,z_b;\mu_i) [\int_{z=0}^{z_b} T(z) dT_\nu(0,z;-\mu_i)]$$

$$+ T_3(\nu,z_t;-\mu_i) T_p(\mu_i) T_\nu(0,z_b;\mu_i) \qquad (4\text{-}21)$$

where $T_p(\mu_i)$ is defined to be the top/down throughput of the cloud for
the stream defined by μ_i and z_b is the height of the cloud base.

$$T_p(-_i) = T_3(\nu,z_b;-\mu_i)/T_3(\nu,z_t;-\mu_i) \qquad (4\text{-}22)$$

The solution of the microwave transfer equation given by
Eq. (4-18) is applicable only to isothermal and homogeneous cloud
layers. To apply the transfer solution to thick clouds it is neces-
sary to divide the cloud into sublayers for which the isothermal and

homogeneous assumptions are reasonable. By matching the brightness
temperature continuity equation for brightness temperature in each
sublayer, a set of linear equations with unknown coefficients can be
obtained which can be solved by standard matrix inversion techniques.
Similar procedures have been used by Liou (1975) to evaluate the
transfer of solar radiation in inhomogeneous atmospheres and by
Feddes and Liou (1977) to investigate the transfer of spectral
infrared radiation in cloudy atmospheres.

CHAPTER 5

RADIATIVE TRANSFER IN A CYLINDRICAL MEDIUM -
A SPHERICAL HARMONICS APPROACH

Radiative transfer in cylindrical geometry will be investigated for a one dimensional cylindrically symmetric infinite cylinder and a two dimensional infinite cylinder. The source function was chosen so as to represent terrestrial radiation. Note that the frequency dependence index, ν, is omitted for simplicity.

5.1 Basic Equations and Simplifying Assumptions

Monochromatic radiative transfer can be described by the equation

$$-\frac{dI}{\beta_e ds} = I - J \quad .\tag{5-1}$$

I is the monochromatic intensity (or radiance), J is the source function, β_e is the extinction coefficient, and s is a distance in space (Chandrasekhar, 1950). Since

$$\frac{dI}{ds} = \vec{\Omega} \cdot \nabla I + \frac{1}{c}\frac{I}{t}\tag{5-2}$$

Eq. (5.1) becomes

$$-\frac{1}{\beta_e}(\vec{\Omega}\cdot\nabla)I(\vec{s},\vec{\Omega};t) - \frac{1}{c}\frac{\partial I(\vec{s},\vec{\Omega};t)}{\partial t} = I(\vec{s},\vec{\Omega};t) - J(\vec{s},\vec{\Omega};t)\tag{5-3}$$

where $\vec{\Omega}$ is a unit vector specifying the direction of scattering through a position vector, $\vec{s}$. We further reduce the equation by

assuming a steady state, homogeneous medium and we may now write

$$-\frac{1}{\beta_e}(\vec{\Omega}\cdot\nabla)I(\vec{s},\vec{\Omega}) = I(\vec{s},\vec{\Omega}) - J(\vec{s},\vec{\Omega}). \qquad (5-4)$$

In the infrared and microwave spectral regions, the source function J for a scattering, emitting and absorbing atmosphere may be written as

$$J(\vec{s},\vec{\Omega}) = \frac{\tilde{\omega}_\nu}{4\pi} \int_{4\pi} I(\vec{s},\vec{\Omega})P(\vec{\Omega},\vec{\Omega}')d\Omega' + (1-\tilde{\omega}_\nu)B_\nu(T) \qquad (5-5)$$

where $\tilde{\omega}_\nu$ is the single scattering albedo, $B_\nu(T)$ is the Planck function of temperature, T, at wavenumber ν, and P is the scattering phase function which is normalized such that

$$\frac{1}{4\pi} \int_{4\pi} P(\vec{\Omega},\vec{\Omega}')d\Omega' = 1 \ . \qquad (5-6)$$

The source function terms represent multiple scattering and emission, respectively, from the assumed homogeneous medium, and the parameters P, $\tilde{\omega}_\nu$ and β_e are assumed to be independent of the position vector, $\vec{s}$. We now write Eq. (5-4) in cylindrical coordinates as

$$-\frac{1}{\beta_e}[\Omega_r \frac{\partial}{\partial r} + \Omega_{\phi_r} \frac{\partial}{\partial \phi_r} + \Omega_z \frac{\partial}{\partial z}]I(\vec{s},\vec{\Omega}) = I(\vec{s},\vec{\Omega}) - J(\vec{s},\vec{\Omega}) \ .$$

$$(5.7)$$

The relevant geometry of the cylinder is illustrated in Fig. 7. $\vec{r}$ is a position vector from the center of the cylinder to a point on the cylinder wall. $\vec{\Omega}$ is described by θ, the angle from the z axis, and ϕ, the difference between ϕ_Ω, the projection of $\vec{\Omega}$ onto the plane containing $\vec{r}$, and ϕ_r, the angle of the polar coordinates of $\vec{r}$. As can be seen from Fig. 7, the components of $\vec{\Omega}$ may be written as
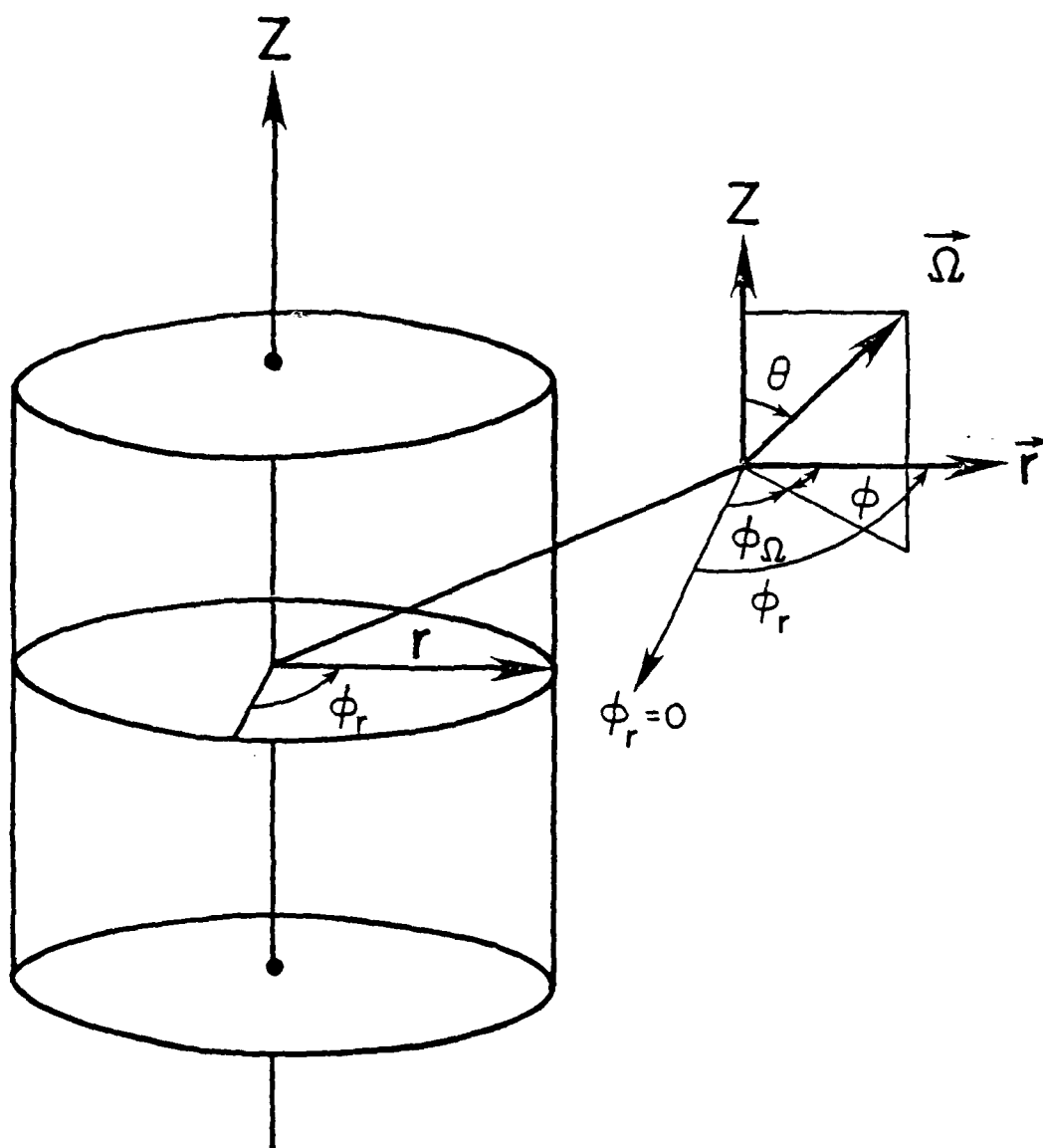
Figure 7. Cylindrical geometry.

$$\Omega_r = \sin\theta \cos\phi$$

$$\Omega_{\phi_r} = -\frac{\sin\theta \sin\phi}{r}$$

$$\Omega_z = \cos\theta \qquad\qquad (5\text{-}8)$$

We now make the further assumption that the z axis of the cylinder is infinite and the problem becomes independent of z. Eq. (5-7) becomes (substituting in Eqs. (5-8))

$$-\frac{1}{\beta_e}\left[\sin\theta\cos\phi\,\frac{\partial}{\partial r} - \frac{\sin\theta\sin\phi}{r}\,\frac{\partial}{\partial\phi_r}\right]I(\vec{r},\vec{\Omega}) = I(\vec{r},\vec{\Omega})$$

$$-\frac{\tilde{\omega}_\nu}{4\pi}\int_{4\pi} I(\vec{r},\vec{\Omega})P(\vec{\Omega},\vec{\Omega}')d\Omega' + (1-\tilde{\omega}_\nu)B_\nu(T) \quad . \qquad (5\text{-}9)$$

We will seek approximate solutions for Eq. (5-9) using the spherical harmonics method. We expand the phase function as

$$P(\vec{\Omega},\vec{\Omega}') = \sum_{\ell=0}^{\infty}\sum_{m=-\ell}^{\ell}\tilde{\omega}_\ell\,Y_\ell^{m\star}(\vec{\Omega}')\,Y_\ell^{m}(\vec{\Omega}) \qquad (5\text{-}10)$$

The assumed form for the solution for the intensity may also be written as

$$I(\vec{r},\vec{\Omega}) = \sum_{\ell=0}^{\infty}\sum_{m=-\ell}^{\ell}I_\ell^{m}(\vec{r})Y_\ell^{m}(\vec{\Omega}) + B_\nu(T). \qquad (5\text{-}11)$$

where * denotes the complex conjugate, $\tilde{\omega}_\ell$ are coefficients of expansion, and the spherical harmonic $Y_\ell^{m}(\vec{\Omega})$ is defined as

$$Y_\ell^{m}(\vec{\Omega}) = (-1)^{\frac{m+|m|}{2}}\sqrt{\frac{(\ell-|m|)!}{(\ell+|m|)!}}\,P_\ell^{m}(\cos\theta)e^{im\phi} \quad . \qquad (5\text{-}12)$$

The $P_\ell^{m}(\cos\theta)$ are the associated Legendre polynomials described by Janke-Emde (1945). These spherical harmonics satisfy the orthonormalization relation such that

$$\int_{\Omega} Y_{\ell}^{m}(\vec{\Omega}) Y_{\alpha}^{\beta\star}(\vec{\Omega}) d\Omega = \frac{4\pi}{2\alpha+1} \delta_{\alpha}^{\ell} \delta_{\beta}^{m} \qquad (5\text{-}13)$$

where δ_{α}^{ℓ} and δ_{β}^{m} are the Kronecker delta functions. Some additional useful relationships are the addition theorum

$$P_{\ell}(\cos\theta) = \sum_{m=-\ell}^{\ell} Y_{\ell}^{m}(\vec{\Omega}) Y_{\ell}^{m\star}(\vec{\Omega}) \qquad (5\text{-}14)$$

and the recursion formula

$$\sin\theta e^{i\phi} Y_{\ell}^{m}(\vec{\Omega}) = \frac{1}{2\ell+1} \{ \sqrt{(\ell-m-1)(\ell-m)} \ Y_{\ell-1}^{m+1}(\vec{\Omega})$$

$$- \sqrt{(\ell+m+1)(\ell+m+2)} \ Y_{\ell+1}^{m+1}(\vec{\Omega})\} \qquad (5\text{-}15)$$

and

$$\sin\theta e^{-i\phi} Y_{\ell}^{m}(\vec{\Omega}) = \frac{1}{2\ell+1} \{ \sqrt{(\ell-m+1)(\ell-m+2)} \ Y_{\ell+1}^{m-1}(\vec{\Omega})$$

$$- \sqrt{(\ell+m-1)(\ell+m)} \ Y_{\ell-1}^{m-1}(\vec{\Omega})\} \qquad . \qquad (5\text{-}16)$$

First, we will investigate Eq.(5-9) for the case of cylindrical symmetry, i.e., the intensity is a function of r, θ and ϕ, and then will return to the more general problem where the intensity is a function of $\vec{r}(r,\rho_r)$, θ and ϕ.

5.2 One-Dimensional Model (Cylindrical Symmetry)

5.2.1 First Order Solution

We rewrite Eq. (5-9) to reflect cylindrical symmetry as (Kofink, 1959)

$$- \frac{1}{\beta_e} [\sin\theta\cos\phi\frac{\partial}{\partial r} - \frac{\sin\theta\sin\phi}{r} \frac{\partial}{\partial\phi_r}] \, I(r,\vec{\Omega}) = I(r,\vec{\Omega})$$

$$- \frac{\tilde{\omega}_\nu}{4\pi} \int_{4\pi} I(r,\vec{\Omega})P(\vec{\Omega},\vec{\Omega}')d\Omega' + (1-\tilde{\omega}_\nu)B_\nu(T) \, . \qquad (5\text{-}17)$$

Substituting in the expansions for I and P in Eqs. (5-10) and (5-11) and recognizing the orthonormalization property denoted in Eq. (5-13), we carry out the operation

$$\int_{4\pi} [\text{Eq. } (5.17)] \cdot Y_\alpha^{\beta *} (\vec{\Omega}) \, d\Omega \qquad (5\text{-}18)$$

and we utilize the recursion formula in Eqs. (5-15) and (5.16). We then obtain the set of partial differential equations as follows:

$$\frac{A_\alpha^\beta}{\beta_e} [\frac{d}{dr} + \frac{(\beta+1)}{r}] \, I_{\alpha+1}^{\beta+1}(r) - \frac{B_\alpha^\beta}{\beta_e} [\frac{d}{dr} - \frac{(\beta-1)}{r}] \, I_{\alpha+1}^{\beta-1}(r)$$

$$- \frac{C_\alpha^\beta}{\beta_e} [\frac{d}{dr} + \frac{(\beta+1)}{r}] \, I_{\alpha-1}^{\beta+1} (r) + \frac{D_\alpha^\beta}{\beta_e} [\frac{d}{dr} - \frac{(\beta-1)}{r}] \, I_{\alpha-1}^{\beta-1} (r)$$

$$= I_\alpha^\beta (r) - \frac{\tilde{\omega}_\nu}{2\alpha+1} \, \tilde{\omega}_\alpha I_\alpha^\beta(r) - (1-\tilde{\omega}_\nu)B_\nu(T) \, . \qquad (5\text{-}19)$$

The parameters A, B, C and D are defined as

$$A_\alpha^\beta = \frac{(\alpha+\beta+1)^{1/2} (\alpha+\beta+2)^{1/2}}{2(2\alpha+3)} \qquad (5\text{-}20a)$$

$$B_\alpha^\beta = \frac{(\alpha-\beta+1)^{1/2} (\alpha-\beta+2)^{1/2}}{2(2\alpha+3)} \qquad (5\text{-}20b)$$

$$C_\alpha^\beta = \frac{(\alpha-\beta-1)^{1/2} (\alpha-\beta)^{1/2}}{2(2\alpha-1)} \qquad (5\text{-}20c)$$

$$D_\alpha^\beta = \frac{(\alpha+\beta-1)^{1/2}\,(\alpha+\beta)^{1/2}}{2(2\alpha-1)} \tag{5-20d}$$

Some details of this procedure may be found in the Appendix. By noting that $\tau = \beta_e r$ we may rewrite Eq. (5-19), for simplicity, as

$$A_\alpha^\beta[\frac{d}{d\tau} + \frac{\beta+1}{\tau}]I_{\alpha+1}^{\beta+1}(\tau) - B_\alpha^\beta[\frac{d}{d\tau} - \frac{\beta-1}{\tau}]I_{\alpha+1}^{\beta-1}(\tau) - C_\alpha^\beta[\frac{d}{d\tau} + \frac{\beta+1}{\tau}]I_{\alpha-1}^{\beta+1}(\tau)$$

$$+ D_\alpha^\beta[\frac{d}{d\tau} - \frac{\beta-1}{\tau}]I_{\alpha-1}^{\beta-1}(\tau) = \gamma_\alpha I_\alpha^\beta(\tau) - (1-\tilde{\omega}_\nu)B_\nu(T) \tag{5-21}$$

where

$$\gamma_\alpha = 1 - \frac{\tilde{\omega}_\nu \tilde{\omega}_\alpha}{2\alpha+1} \quad . \tag{5-22}$$

For a first approximation to the set of partial differential equations, (5-15), we select the zero and first modes and set the $\ell = 2, \ldots\infty$ modes to zero. Allowing these degrees of freedom we obtain the four basic equations:

$$A_0^0[\frac{d}{d\tau} + \frac{1}{\tau}]I_1^1(\tau) - B_0^0[\frac{d}{d\tau} + \frac{1}{\tau}]I_1^{-1}(\tau) = (1-\tilde{\omega}_\nu)I_0^0(\tau) - (1-\tilde{\omega}_\nu)B_\nu(T)$$
$$\tag{5-23}$$

$$C_1^{-1}\frac{d}{d\tau}I_0^0(\tau) = I_1^{-1}(\tau) - \frac{\tilde{\omega}_\nu \tilde{\omega}_1}{3}I_1^{-1}(\tau) \tag{5-24}$$

$$I_1^0(\tau) = 0 \tag{5-25}$$

$$D_1^1\frac{d}{d\tau}I_0^0(\tau) = I_1^1(\tau) - \frac{\tilde{\omega}_\nu \tilde{\omega}_1}{3}I_1^1(\tau) \tag{5-26}$$

Solving for I_1^1 and I_1^{-1} in Eqs. (5-24) and (5-26), respectively, and substituting into Eq. (5-23), and taking the homogeneous portion only, yields

$$\tau^2 \frac{d^2 I_0^0(\tau)}{d\tau^2} + \tau \frac{d I_0^0(\tau)}{d\tau} + \tau^2 n^2 I_0^0(\tau) = 0 \qquad (5\text{-}27)$$

which is Bessel's equation of order zero with a parameter n. Here

$$n^2 \equiv \frac{\tilde{\omega}_\nu - 1}{\xi} \qquad (5\text{-}28a)$$

where

$$\xi = \frac{A_0^0 D_1^1 + B_0^0 C_1^{-1}}{(1 - \frac{\tilde{\omega}_\nu \tilde{\omega}_1}{3})} \qquad (5\text{-}28b)$$

The solution to Bessel's equation may be written in terms of the modified Bessel functions as

$$I_0^0(\tau) = c_1 I_0(\frac{\tau}{\lambda}) + c_2 k_0(\frac{\tau}{\lambda}) \qquad (5\text{-}29)$$

where $\lambda = \frac{1}{n}$, I_0 and k_0 are the zeroth order modified Bessel functions of the first and second kind, respectively, and c_1 and c_2 are constants to be determined.

There are two boundary conditions to be applied for the first order approximation with cylindrical symmetry. First we recognize that the intensity is finite at $\tau = 0$. Since $k_0(\frac{\tau}{\lambda})$ approaches minus infinity at $\tau = 0$, we must have $c_2 = 0$. Therefore

$$I_0^0(\tau) = c_1 I_0(\frac{\tau}{\lambda}) \quad . \qquad (5\text{-}30)$$

The second condition is on the outer boundary and will be discussed in general in the next section.

5.2.2 Extension to Higher Order Approximations

We assume, as proposed by Kofink (1959), that the system of

partial differential equations denoted in Eq. (5-21) is satisfied by a linear combination of modified Bessel functions

$$I_\ell^m(\tau) = c_{1\lambda} P_\ell^m(\cdot) I_m(\tfrac{\tau}{\cdot}) + c_{2\cdot} Q_\ell^m(\cdot) K_m(\tfrac{\tau}{\cdot})$$

where $c_{1\lambda}$, $c_{2\lambda}$ are arbitrary constants and P_ℓ^m and Q_ℓ^m are eigenfunctions of the eigenvalue, λ. Once again, applying the boundary condition at $\tau = 0$, we find $C_{2\lambda} = 0$ and

$$I_\ell^m(\tau) = c_{1\lambda} P_\ell^m(\lambda) I_m(\tfrac{\tau}{\lambda}) \tag{5-32}$$

Through the recursion properties of the modified Bessel functions we find that it is possible to transform Eq. (5.21) into recursion relations for the eigenfunctions $P_\ell^m(\lambda)$. The recursion formula are:

$$I_{-m}(x) = I_m(x) \tag{5.33a}$$

$$\tfrac{1}{2}[I_{m-1}(x) - I_{m+1}(x)] = \tfrac{m}{x} I_m(x) \tag{5.33b}$$

$$\tfrac{1}{2}[I_{m-1}(x) + I_{m+1}(x)] = \frac{dI_m(x)}{dx} \quad . \tag{5.33c}$$

From Eqs. (5.33) we find

$$[\tfrac{d}{d\tau} + \tfrac{m+1}{\tau}]I_{\ell\pm1}^{m+1}(\tau) = \tfrac{1}{\cdot} \{c_{1\lambda} P_{\ell\pm1}^{m+1}(\cdot) I_m(\tfrac{\tau}{\cdot})\} \tag{5.34a}$$

and

$$[\tfrac{d}{d\tau} - \tfrac{m-1}{\tau}]I_{\ell\pm1}^{m-1}(\tau) = \tfrac{1}{\cdot} \{c_1 P_{\ell\pm1}^{m-1}(\cdot) I_m(\tfrac{\tau}{\cdot})\} \quad . \tag{5.34b}$$

Therefore we may write

$$A_\ell^m P_{\ell+1}^{m+1}(\cdot) - B_\ell^m P_{\ell+1}^{m-1}(\cdot) - C_\ell^m P_{\ell-1}^{m+1}(\cdot) + D_\ell^m P_{\ell-1}^{m-1}(\cdot) = \gamma_\ell P_\ell^m(\cdot) \quad .$$

(5-35)

By eliminating the square roots in the coefficients by the formula

$$P_\ell^m(\cdot) = (2\ell+1 \frac{(-1)^{(\ell-m)/2}}{2^\ell} \cdot \frac{\sqrt{(\ell-m)!(\ell+m)!}}{(\frac{\ell-m}{2})!(\frac{\ell+m}{2})!} R_\ell^m(\cdot)), \qquad (5-36)$$

the recursion formula for the $P_\ell^m(\cdot)$ is transformed into a simpler relationship in $R_\ell^m(\cdot)$

$$(\ell+m+1)R_{\ell+1}^{m+1}(\cdot) + (\ell-m+1)R_{\ell+1}^{m-1}(\cdot) + (\ell-m)R_{\ell-1}^{m+1}(\cdot) + (\ell+m)R_{\ell-1}^{m-1}(\cdot)$$

$$= 2(2\ell+1) \gamma_\ell R_\ell^m(\cdot) \quad . \qquad (5-37)$$

The solution for Eq. (5.37) may be written (according to Kofink)

$$R_\ell^m(\cdot) = \beta_\ell^{m(z)} g_\ell^{(z)}(\lambda) \qquad (5-38)$$

where the superscript (z) represents the main solution $(z=0)$ or the zth complementary solution $(z = 1,\infty)$. We will discuss the main solution first.

The main solution satisfies the recursion formula

$$(\ell+1)g_{\ell+1}^{(0)}(\cdot) + \ell g_{\ell-1}^{(0)}(\cdot) = (2\ell+1)\gamma_\ell g_\ell^{(0)}(\cdot) \quad , \qquad (5-39)$$

and $\beta_\ell^{m(0)} \equiv 1$. The set of $g_\ell^{(0)}(\cdot)$ begins with $\ell = 0$ with $g_0^{(0)}(\cdot)$ arbitrarily set to 1. We write out the first few $g_\ell^{(0)}(\cdot)$ in terms of $g_0^{(0)}(\cdot)$ as

$$g_0^{(0)}(\cdot) = 1$$

$$g_1^{(0)}(\cdot) = \gamma_0 \, g_0^{(0)}(\cdot)$$

$$g_2^{(0)}(\cdot) = (\frac{3}{2}\gamma_0\gamma_1\cdot^2 - \frac{1}{2})g_0^{(0)}(\cdot)$$

$$g_3^{(0)}(\cdot) = [\frac{5}{2}\gamma_0\gamma_1\gamma_2\cdot^3 - (\frac{5}{6} + \frac{2}{3}\gamma_0)\cdot]\,g_0^{(0)}(\cdot) \qquad (5\text{-}40)$$

It is convenient to write Eqs. (5-40) in matrix form as

$$
\begin{bmatrix}
-\gamma_0 & 1 & 0 & 0 & 0 & . & . & . \\
1 & -3\gamma_1 & 2 & 0 & 0 & . & . & . \\
0 & 2 & -5\gamma_2 & 3 & 0 & . & . & . \\
0 & 0 & 3 & -7\gamma_3 & 4 & . & . & . \\
. & . & . & . & . & . & . & . \\
. & . & . & . & . & . & . & . \\
. & . & . & . & . & . & . & .
\end{bmatrix}
\begin{bmatrix}
g_0^{(0)} \\
g_1^{(0)} \\
g_2^{(0)} \\
g_3^{(0)} \\
. \\
. \\
.
\end{bmatrix}
= 0.
$$

$$(5\text{-}41)$$

This system of equations for the main solution can be carried out to the order of approximation desired. A nontrivial solution to Eq. (5-41) may be obtained by setting the determinant equal to zero. We then find the roots of the characteristc polynomial, which are the set of . There will be $(n + 1)/2$ pairs of roots for the main solution since n is normally taken to be odd. The roots of the characteristic polynomial may be gotten directly for $n = 1,3$. We find

$$\cdot_1^{(0)} = \pm \sqrt{3\gamma_0\gamma_1} \quad \text{for } n = 1$$

and the four roots

$$\begin{matrix} \pm \eta_1^{(0)} \\ \pm \eta_2^{(0)} \end{matrix} = \pm \sqrt{\frac{(-b \pm \sqrt{b^2 - 4ac})}{2a}} \quad \text{for } n = 3 \quad,$$

where $a = 105 \, \gamma_0 \gamma_1 \gamma_2 \gamma_3$, $b = -(27 \, \gamma_0 \gamma_1 + 35 \, \gamma_2 \gamma_3 + 28 \, \gamma_0 \gamma_3)$ and $c = 9$.

The characteristic polynomial for higher order n was determined by the following scheme. The tridiagonal matrix is of the form

$$\begin{bmatrix} a_1 & b_2 & 0 & & & & & \\ b_3 & a_2 & b_4 & 0 & & & & \\ 0 & b_5 & a_3 & b_6 & 0 & . & . & \\ . & 0 & b_7 & a_4 & b_8 & . & . & \\ . & . & . & b_9 & a_5 & b_{10} & . & \\ . & . & . & & b_{11} & a_6 & . & \\ & & & & & . & . & . \\ & & & & & & . & . & b_{2n-2} \\ & & & & & & & b_{2n-1} & a_n \end{bmatrix}$$

$$(5\text{-}42)$$

and the characteristic function is given by the sequence

$$\begin{aligned} f_0 &= 1 \\ f_1 &= a_1 \\ f_2 &= a_2 f_1 - b_2 b_3 f_0 \\ f_3 &= a_3 f_2 - b_4 b_5 f_1 \\ &\ . \\ &\ . \\ &\ . \\ f_n &= a_n f_{n-1} - b_{2n-1} b_{2n-2} f_{n-2} \end{aligned}$$

For n≥5, we are no longer able to solve directly for the eignevalues, and therefore have employed Newton's iteration scheme to numerically calculate the roots.

Mark (1945) showed that one additional degree of freedom in the solution is created every time n is increased by two. These "complementary" solutions are reflected in Eq. (5-38) and the recursion formula for the complementary solutions corresponding to that for the main solution given by Eq. 5-39 (Kofink, 1959) may be written

$$(\lambda+1-2z)g_{\lambda+1}^{(z)}[\lambda_k^{(z)}] + (\lambda+2z)g_{\lambda-1}^{(z)}[\lambda_k^{(z)}] = (2\lambda+1)\lambda_k^{(z)}\gamma_\lambda g_\lambda^{(z)} \ ,$$

$$\lambda \gtreqless 2n$$

$$n = 1, 2, 3 \tag{5-43}$$

The coefficients, ε_λ^m, of Eq. (5-38) may be determined, then, by the recursion relations

$$(\lambda+m+1)\varepsilon_{\lambda+1}^{m+1}(z) + (\lambda-m+1)\varepsilon_{\lambda+1}^{m-1}(z) = 2(\lambda-2n+1)\varepsilon_\lambda^m(z) \tag{5-44a}$$

and

$$(\lambda-m)\varepsilon_{\lambda-1}^{m+1}(z) + (\lambda+m)_{\lambda-1}^{m-1}(z) = 2(\lambda+2n)\varepsilon_\lambda^m(z) \ . \tag{5.44b}$$

For example, beginning at $(\lambda,m) = (0,0)$ with $g_0^{(0)}$ arbitrarily set to 1, we may add the arbitrary constant $R_2^{0(1)}$ to the main solution at $(\lambda,m) = (2,0)$

$$R_2^0[\lambda_k^{(0)}] = g_2^{(0)}[\lambda_k^{(0)}] + R_2^{0(1)}[\lambda_j^{(1)}] \ . \tag{5.45}$$

$R_2^{0(1)}[\lambda_j^{(1)}]$, the first complementary solution, begins a new series of functions $g^{(1)}[\lambda_j^{(1)}]$ with $\lambda \gtreqless 2$, that obey the recursion formula in

Eqs. (5-43) and (5-44). Starting with $g_2^{(1)}[\lambda_j^{(1)}]$ arbitrarily set to 1, we solve the recursion formula (Eq. (4-43)) straightforwardly until we reach the order of the approximation we desire ($\ell = n$). For an example, we write out the matrices needed for a fifth order solution (n=5).

For the main solution we have

$$
\begin{bmatrix}
-\gamma_0 \lambda_k^{(0)} & 1 & 0 & 0 & 0 & 0 \\
1 & -3\gamma_1 \lambda_k^{(0)} & 2 & 0 & 0 & 0 \\
0 & 2 & -5\gamma_2 \lambda_k^{(0)} & 3 & 0 & 0 \\
0 & 0 & 3 & -7\gamma_3 \lambda_k^{(0)} & 4 & 0 \\
0 & 0 & 0 & 4 & -9\gamma_4 \lambda_k^{(0)} & 5 \\
0 & 0 & 0 & 0 & 5 & -11\gamma_5 \lambda_k^{(0)}
\end{bmatrix}
\begin{bmatrix}
g_0^{(0)} \\
g_1^{(0)} \\
g_2^{(0)} \\
g_3^{(0)} \\
g_4^{(0)} \\
g_5^{(0)}
\end{bmatrix}
= 0 .
$$

(5-46)

For the first complementary solution we have

$$
\begin{bmatrix}
-5\gamma_2 \lambda_j^{(1)} & 1 & 0 & 0 \\
5 & -7\gamma_3 \lambda_j^{(1)} & 2 & 0 \\
0 & 6 & -9\gamma_4 \lambda_j^{(1)} & 3 \\
0 & 0 & 7 & -11\gamma_5 \lambda_j^{(1)}
\end{bmatrix}
\begin{bmatrix}
g_2^{(1)} \\
g_3^{(1)} \\
g_4^{(1)} \\
g_5^{(1)}
\end{bmatrix}
= 0 . \qquad (5-47)
$$

For the second complementary solution we have

$$
\begin{bmatrix}
-9\gamma_4 \lambda_i^{(2)} & 1 \\
9 & -11\gamma_5 \lambda_i^{(2)}
\end{bmatrix}
\begin{bmatrix}
g_4^{(2)} \\
g_5^{(2)}
\end{bmatrix}
= 0. \qquad (5-48)
$$

Once we have determined the $\lambda_k^{(z)}$, we may calculate the functions $P_\ell^m[\lambda_k^{(z)}]$ and the modified Bessel functions $I_m[\tau/\lambda_k^{(z)}]$ (please see Eq. (5-32)). We now turn our attention to the calculation of the unknown coefficients, $c_1[\lambda_k^{(z)}]$ by means of applying the boundary condition at the outer surface.

5.2.3   Boundary Conditions at the Outer Surface

From the preceding discussion, we have seen that there are $(n + 1)/2$ pairs of eigenvalues in the main solution and $(n^2 - 1)/8$ pairs of additional roots occuring in the complementary solutions. We add these to find $(n + 1)(n + 3)/8$ pairs of $\lambda_k^{(z)}$ involved. Therefore, we look for the same number of outer boundary conditions to determine the unknown constants $c_1[\lambda_k^{(z)}]$.

Historically, the rigorous boundary condition first applied to this type of problem was (in the neutron transport literature) the so called "Vacuum" boundary condition, e.g., no energy incident on the boundary or

$$I(\tau,\mu) = 0. \tag{5-49}$$

It is obvious that this condition cannot be met exactly by any finite expansion of the intensity. Mark (1945) suggested that

$$I(\tau,\mu_i) = 0 \tag{5-50}$$

where the intensity was expanded in a truncated series of Legendre polynomials and the μ_i were the $\ell/2$ positive roots of $P_\ell(\mu_i) = 0$. Marshak (1947) suggested setting

$$\int_0^1 I(\tau,\mu)P_{2i+1}(\mu)d\mu = 0 \tag{5-51}$$

where the intensity is expanded in the same truncated Legendre form to approximate the "vacuum" boundary. It is worthy of note that Marshak's proposal seems to be much more widely applied than Mark's for a zero incident intensity distribution (e.g., Pomraning, 1964; Gelbard, 1968; Dave and Canosa, 1974).

In this study we are interested in the situation when there is an intensity distribution incident on the outer boundary

$$I(r,\vec{\Omega}) = f(\vec{\Omega}). \tag{5-52}$$

In this situation, a generalization of Marshak's integral conditions appear to enjoy popular acceptance. These conditions may be written

$$\int_0^1 P_{2n+1}(\mu) \{I(\tau,\mu) - f(\mu)\} \, d\mu = 0. \tag{5-53}$$

Since the incoming intensity distribution incident on the boundary, $f(\mu)$, is presumed known, one may carry out the various angular integrations.

For this study, an analogous method was used to approximate the boundary conditions. Rewriting Eq. (5-10), for convenience, and recalling that we are dealing, at present, with the cylindrically symmetric case, and recognizing the form of $I_\ell^m(\tau)$ (Eq. (5-32)), we have

$$I(\tau,\vec{\Omega}) = B_\nu(T) + \sum_{\ell=0}^\infty \sum_{m=-\ell}^\infty \sum_{\lambda_k(z)} c_1[\lambda_k(z)]P_\ell^m[\lambda_k(z)]I_m[-\frac{\tau}{\lambda(z)}]Y_\ell^m(\vec{\Omega})$$

$$\tag{5-54}$$

where

$$\overline{Y}_{\ell}^{m}(\vec{\Omega}) = \begin{bmatrix} Y_{\ell}^{m}(\vec{\Omega}) + (-1)^{m} \, Y_{\ell}^{-m}(\vec{\Omega}), & m \neq 0 \\ Y_{\ell}^{0}(\vec{\Omega}) & m=0 \end{bmatrix} . \qquad (5\text{-}55)$$

Note that we have combined the spherical harmonics using the relation-ship $P_{\ell}^{m}[\lambda_{k}^{(z)}] = (-1)^{m} \, P_{\ell}^{-m}[\lambda_{k}^{(z)}]$ (Kofink, 1959). Now we choose a weight function (as in Marshak's method), multiply both sides of Eq. (5-54) by it, and integrate over the appropriate domain. The choice of the weight function should be related to the spherical harmonics and is taken to be $\overline{Y}_{\alpha}^{\beta}(\theta,\phi)$ where $(\alpha+\beta)$ = even. The domain of the incident hemisphere is $0 \leq \theta \leq \pi$ and $\frac{\pi}{2} \leq \phi \leq \frac{3\pi}{2}$. Carrying out the indicated operations, we may write

$$\int\limits_{0}^{\pi} \int\limits_{\pi/2}^{3\pi/2} B_{\nu}(T) Y_{0}^{0}(\theta,\phi) \overline{Y}_{\alpha}^{\beta}(\theta,\phi) \sin\theta \, d\theta \, d\phi$$

$$+ \int\limits_{0}^{\pi} \int\limits_{\pi/2}^{3\pi/2} \sum\limits_{\ell=0}^{\infty} \sum\limits_{m=-\ell}^{\ell} \sum\limits_{\lambda_{k}^{(z)}} c_{1}[\lambda_{k}^{(z)}] P_{\ell}^{m}[\lambda_{k}^{(z)}] I_{m}[\frac{\tau}{\lambda_{k}^{(z)}}]$$

$$\cdot \; \overline{Y}_{\ell}^{m}(\theta,\phi) \overline{Y}_{\alpha}^{\beta}(\theta,\phi) \sin\theta \, d\theta \, d\phi$$

$$= \int\limits_{0}^{\pi} \int\limits_{\pi/2}^{3\pi/2} I(\tau,\theta,\phi) Y_{0}^{0}(\theta,\phi) \overline{Y}_{\alpha}^{\beta}(\theta,\phi) \sin\theta \, d\theta \, d\phi \qquad (5\text{-}56)$$

where the right side of the equation is the known incident intensity distribution. The evaluation of the integrals of the produces of the spherical harmonics becomes quite tedious for higher order approxima-tions. For this study, the integrals were accomplished analytically up to and including n=5. A general numerical scheme for these inte-grations has been developed by Ou (1979, private communication).

Continuing with n=5, for example, we look for $(n+1)(n+3)/8$ or 6 outer boundary conditions for our one-dimensional study. These will be obtained by accomplishing the operation described by Eq. (5-56) with the following weight functions

$$\overline{Y}_1^1(\vec{\Omega}) = Y_1^1(\vec{\Omega}) - Y_1^{-1}(\vec{\Omega}) = -\sqrt{2}\, P_1^1(\mu)\, \cos\phi$$

$$\overline{Y}_3^1(\vec{\Omega}) = Y_3^1(\vec{\Omega}) - Y_3^{-1}(\vec{\Omega}) = -\sqrt{\frac{1}{3}}\, P_3^1(\mu)\, \cos\phi$$

$$\overline{Y}_3^3(\vec{\Omega}) = -\sqrt{\frac{1}{180}}\, P_3^3(\vec{\Omega})\, \cos 3\phi$$

$$Y_5^1(\vec{\Omega}) = -\sqrt{\frac{2}{15}}\, P_5^1(\mu)\, \cos\phi$$

$$Y_5^3(\vec{\Omega}) = -\sqrt{\frac{1}{5040}}\, P_5^3(\mu)\, \cos 3\phi$$

$$Y_5^5(\vec{\Omega}) = -\sqrt{\frac{1}{907,200}}\, P_5^5(\mu)\, \cos 5\phi \tag{5-57}$$

5.3 Two Dimensional Model

5.3.1 General Solution

We recall Eqs. (5-9)-(5-15). In the one-dimensional case we simplified $I(\vec{r},\vec{\Omega})$ to $I(r,\vec{\Omega})$. For this instance, we take $I(\vec{r},\vec{\Omega})$ to be $I(r,\phi_r,\vec{\Omega})$, where $\vec{r}$ is the polar coordinates of any "slice" across the assumed infinite cylinder. We follow essentially the same procedure as before by substituting in the expansions for the intensity and the phase function, and utilizing the orthonormalization property. We

then carry out the operation

$$\int_{4\pi} \text{Eq. (5-9)} \cdot Y_{\alpha}^{3*}(\vec{\Omega}) d\Omega \ . \tag{5-58}$$

Once again, using the recursion formula, Eqs. (5-15) and (5-16), we obtain the new set of partial differential equations.

$$A_{\alpha}^{\beta} \{\frac{d}{d\tau} + \frac{(\beta+1)}{\tau} - \frac{1}{i\tau} \frac{d}{d\phi_r}\} I_{\alpha+1}^{\beta+1} (\tau,\phi_r) -$$

$$- B_{\alpha}^{\beta} \{\frac{d}{d\tau} - \frac{(\beta-1)}{\tau} + \frac{1}{i\tau} \frac{d}{d\phi_r}\} I_{\alpha+1}^{\beta-1} (\tau,\phi_r)$$

$$- C_{\alpha}^{\beta} \{\frac{d}{d\tau} + \frac{(\beta+1)}{\tau} - \frac{1}{i\tau} \frac{d}{d\phi_r}\} I_{\alpha-1}^{\beta+1} (\tau,\phi_r)$$

$$+ D_{\alpha}^{\beta} \{\frac{d}{d\tau} - \frac{(\beta-1)}{\tau} + \frac{1}{i\tau} \frac{d}{d\phi_r}\} I_{\alpha-1}^{\beta-1} (\tau,\phi_r)$$

$$= \gamma_{\alpha} I_{\alpha}^{\beta} (\tau,\phi_r) - (1-\tilde{\omega}_{\nu}) B_{\nu}(T). \tag{5-59}$$

Details of this integration may be found in Appendix A.

5.3.2 First Order Approximation

Selecting the zero and first order modes we may write from Eq. (5-59) (homogeneous portion only):

$$A_0^0 \{\frac{d}{d\tau} + \frac{1}{\tau} - \frac{1}{i\tau} \frac{d}{d\phi_r}\} I_1^1(\tau,\phi_r) - B_0^0 \{\frac{d}{d\tau} + \frac{1}{\tau} + \frac{d}{d\phi_r}\} I_1^{-1}(\tau,\phi_r) =$$

$$= I_0^0 (1-\tilde{\omega}_{\nu}) \tag{5-60}$$

$$-C_1^{-1} \{\frac{d}{d\phi_r} - \frac{1}{i\tau} \frac{d}{d\phi_r}\} I_0^0 (\tau,\phi_r) = I_1^{-1}(\tau,\phi_r)[1 - \frac{\tilde{\omega}_\nu \omega_1}{3}] \quad (5\text{-}61)$$

$$I_1^0 = 0 \qquad\qquad\qquad (5\text{-}62)$$

$$D_1^1 \{\frac{d}{d\phi_r} + \frac{1}{i\tau} \frac{d}{d\phi_r}\} I_0^0(\tau,\phi_r) = I_1^1(\tau,\phi_r)(1 - \frac{\tilde{\omega}_\nu \omega_1}{3}) \qquad (5\text{-}63)$$

We solve Eqs. (5-61) and (5-63) for I_1^{-1} and I_1^1, respectively, and substitute into Eq. (5-60). After some algebraic manipulation, and noting that

$$A_0^0 D_1^1 = B_0^0 C_1^{-1} = \frac{1}{6} \, ,$$

we may write our new expression as

$$\frac{1}{3\gamma_1} \left[\frac{d^2}{d\tau^2} + \frac{1}{\tau} \frac{d}{d\tau} + \frac{1}{\tau^2} \frac{d^2}{d\phi_r^2}\right] I_0^0(\tau,\phi_r) = \gamma_0 I_0^0(\tau,\phi_r) \, . \qquad (5\text{-}64)$$

We now see that Eq. (5-64) is equivalent to

$$K_1 \nabla^2 I_0^0(\tau,\phi_r) - K_2 I_0^0 = 0 \, ,$$

This is a time-independent diffusion equation expressed in cylindrical coordinates, where

$$K_1 = \frac{1}{3\gamma_1}$$

and

$$K_2 = \gamma_0 \, .$$

Separation of variables is used to solve Eq. (5-64). We let

$$I_0^0(\tau,\phi_r) = R(\tau) \Phi (\phi_r) \qquad\qquad (5\text{-}65)$$

and substituting Eq. (5-65) into Eq. (5-64) and separating variables, we find

$$\frac{\tau^2}{R} \frac{d^2R}{d\tau^2} + \frac{\tau}{R} \frac{dR}{d\tau} - \tau^2 \frac{K_2}{K_1} = n^2 \qquad (5-66)$$

and

$$- \frac{1}{\phi} \frac{d^2\phi}{d\phi_r^2} = n^2 \qquad (5-67)$$

Eq. (5-67) may be written as

$$\frac{d^2\phi}{d\phi_r^2} + n^2 \phi = 0$$

and the solution is

$$\phi = A_n \cos(n\phi_r) + B_n \sin(n\phi_r) . \qquad (5-68)$$

Eq. (5-66) may be expressed as

$$\tau^2 \frac{d^2R}{d\tau^2} + \tau \frac{dR}{d\tau} - (\tau^2 \frac{K_2}{K_1} + n^2) R = 0 .$$

This is the modified Bessel equation with a parameter $\lambda = \sqrt{\frac{K_2}{K_1}}$. As before, we let $\lambda = \frac{1}{\lambda}$, and the solution to Eq. (5-66) is

$$R = C_{1,n} I_n(\frac{\tau}{\lambda}) + C_{2,n} K_n(\frac{\tau}{\lambda}), \text{ n unrestricted. } (5.69)$$

From Eq. (5-65) the complete solution is

$$I_0^0(\tau, \phi_r) = \sum_{n=0}^{\infty} [C_{1,n} I_n(\frac{\tau}{\lambda}) + C_{2,n} K_n(\frac{\tau}{\lambda})][A_n \cos(n\phi_r) + B_n \sin(n\phi_r)]$$
$$(5-70)$$

Two boundary conditions are applied at this time for simplicity. As

before, we must have $C_{2,n}=0$ since $K_n \to -\infty$ as $\tau \to 0$. Next, since $\phi(0) = \phi(2\tau)$ on any "slice" of the cylinder, we must have n be an integer. We may now rewrite Eq. (5-70) (combining and renaming the constants) as

$$I_0^0(\tau, \phi_r) = \sum_{n=0}^{\infty} I_n(\frac{\tau}{\lambda})[A_n \cos(n\phi_r) + B_n \sin(n\phi_r)] . \qquad (5-71)$$

Eqs. (5-61) and (5-63) may now be solved for $I_1^{-1}(\tau, \phi_r)$ and $I_1^1(\tau, \phi_r)$, respectively. We recall the first order approximation expansion for the intensity (homogeneous portion of Eq. (5-10)) may be expressed as

$$I(\vec{\tau}, \vec{\phi}) = I_0^0(\tau, \phi_r)Y_0^0(\theta, \phi) + I_1^1(\tau, \phi_r)Y_1^1(\theta, \phi) + I_1^{-1}(\tau, \phi_r)Y_1^{-1}(\theta, \phi) .$$
$$(5-72)$$

We may write $I_1^{-1}(\tau, \phi_r)$ and $I_1^1(\tau, \phi_r)$ as

$$I_1^1(\tau, \phi_r) = \frac{1}{\sqrt{2} \, \gamma_1} \sum_n \{\frac{1}{2\lambda} [I_{n-1}(\frac{\tau}{\lambda}) + I_{n+1}(\frac{\tau}{\lambda})][A_n \cos(n\phi_r)$$

$$+ B_n \sin(n\phi_r)] + I_n(\frac{\tau}{\lambda}) \frac{n}{\tau} [-A_n \sin(n\phi_r) + B_n \cos(n\phi_r)]\}$$
$$(5-73)$$

and

$$I_1^{-1}(\tau, \phi_r) = \frac{1}{\sqrt{2} \, \gamma_1} \sum_n \{\frac{1}{2\lambda} [I_{n-1}(\frac{\tau}{\lambda}) + I_{n+1}(\frac{\tau}{\lambda})][A_n \cos(n\phi_r)$$

$$+ B_n \sin(n\phi_r)] - I_n(\frac{\tau}{\lambda}) \frac{n}{\tau} [-A_n \sin(n\phi_r)$$

$$+ B_n \cos(n\phi_r)] . \qquad (5-74)$$

We substitute Eqs. (5-71), (5-73) and (5-74) into Eq. (5-72 and may write

$$I(\tau,\phi_r,\theta,\phi) = \sum_n I_n(\tfrac{\tau}{\lambda})[A_n \cos(n\phi_r) + B_n \sin(n\phi_r)]$$

$$+ \frac{1}{\sqrt{2}\,\gamma_1} \sum_n \{\frac{1}{2\lambda}[I_{n-1}(\tfrac{\tau}{\lambda}) + I_{n+1}(\tfrac{\tau}{\lambda})][A_n \cos(n\phi_r) + B_n \sin(n\phi_r)]$$

$$+ \frac{I_n(\tfrac{\tau}{\lambda})}{i\tau} n[-A_n \sin(n\phi_r) + B_n \cos(n\phi_r)]\} \; Y_1^1(\vec{\Omega})$$

$$- \frac{1}{\sqrt{2}\,\gamma_1} \sum_n \{\frac{1}{2\lambda}[I_{n-1}(\tfrac{\tau}{\lambda}) + I_{n+1}(\tfrac{\tau}{\lambda})][A_n \cos(n\phi_r) + B_n \sin(n\phi_r)]$$

$$- \frac{I_n(\tfrac{\tau}{\lambda})}{i\tau} n\,[-A_n \sin(n\phi_r) + B_n \cos(n\phi_r)]\} \; Y_1^{-1}(\vec{\Omega}) \; . \qquad (5\text{-}75)$$

To combine terms we add and subtract $Y_1^1(\vec{\Omega})$ and $Y_1^{-1}(\vec{\Omega})$ as

$$Y_1^1(\vec{\Omega}) - Y_1^{-1}(\vec{\Omega}) = -\sqrt{2}\, P_1^1(u)\, \cos\phi \qquad (5\text{-}76a)$$

and

$$Y_1^1(\vec{\Omega}) + Y_1^{-1}(\vec{\Omega}) = -\sqrt{2}\, i\, P_1^1(u)\, \sin\phi \qquad (5\text{-}76b)$$

where $P_\lambda^m(u)$ are the associated Legendre functions. Rewriting Eq. (5-75) to reflect these combinations, we have

$$I(\tau,\phi_r,\theta,\phi) = \sum_n I_n(\tfrac{\tau}{\lambda})[A_n \cos(n\phi_r) + B_n \sin(n\phi_r)]$$

$$+ \frac{1}{\sqrt{2}\,\gamma_1} \sum_n \{\frac{1}{2\lambda}[I_{n-1}(\tfrac{\tau}{\lambda}) + I_{n+1}(\tfrac{\tau}{\lambda})][A_n \cos(n\phi_r) + B_n \sin(n\phi_r)]$$

$$\cdot [Y_1^1(\vec{\Omega}) - Y_1^{-1}(\vec{\Omega})]:$$

$$+ \frac{1}{\sqrt{2}\,\gamma_1} \sum_n \{ \frac{I_n(\frac{\tau}{\lambda})}{i\tau} n[-A_n \sin(n\phi_r) + B_n \cos(n\phi_r)]$$

$$\cdot [Y_1^1(\vec{\Omega}) + Y_1^{-1}(\vec{\Omega})]\} . \tag{5-77}$$

Upon substituting Eqs. (5-76) into Eq. (5-77), we arrive at

$$I(\tau,\phi_r,\theta,\phi) = \sum_n I_n(\frac{\tau}{\lambda})[A_n \cos(n\phi_r) + B_n \sin(n\phi_r)]$$

$$- \frac{P_1^1(\mu)\cos\phi}{2\lambda\gamma_1} \sum_n [I_{n-1}(\frac{\tau}{\lambda}) + I_{n+1}(\frac{\tau}{\lambda})][A_n \cos(n\phi_r) + B_n \sin(n\phi_r)]$$

$$- \frac{P_1^1(\mu)\sin\phi}{2\lambda\gamma_1} \sum_n [I_{n-1}(\frac{\tau}{\lambda}) - I_{n+1}(\frac{\tau}{\lambda})][B_n \cos(n\phi_r) - A_n \sin(n\phi_r)]. \tag{5-78}$$

Note that we have made use of the recursion properties of the modified Bessel functions (Eq. (5-33b)) in the last term of Eq. (5-78). At this point, the unknown constants, A_n and B_n, may be determined by applying the outer boundary conditions. The discussion of these boundary conditions will be held in abeyance until we have presented the extension of the two-dimensional model to higher orders.

5.3.3 Extension to Higher Order Approximations

To generate higher order approximations for the two dimensional problem, we look for a general solution for the $I_\ell^m(\tau,\phi_r)$. From the form of the first order parameters, $I_0^0(\tau,\phi_r)$, $I_1^1(\tau,\phi_r)$ and $I_1^{-1}(\tau,\phi_r)$, and by comparison with the one dimensional problem, we are led to assume the form

$$I_{\ell}^{m}(\tau,\phi_r) = \sum_{\lambda_k^{(z)}} P_{\ell}^{m}[\lambda_k^{(z)}] \sum_n \left[\frac{I_{n+m}[\frac{\tau}{\lambda_k^{(z)}}] + I_{n-m}[\frac{\tau}{\lambda_k^{(z)}}]}{2} \right]$$

$$\cdot [A_{n,\lambda} \cos(n\phi_r) + B_{n,\lambda} \sin(n\phi_r)] + i\left[\frac{I_{n+m}[\frac{\tau}{\lambda_k^{(z)}}] + I_{n-m}[\frac{\tau}{\lambda_k^{(z)}}]}{2} \right]$$

$$\cdot [B_{n,\lambda} \cos(n\phi_r) - A_{n,\lambda} \sin(n\phi_r)] \} . \qquad (5\text{-}79)$$

Substituting this solution into the homogeneous form of Eq. (5-59) and, again, noting the recursion properties of the modified Bessel functions, we may transform Eq. (5-59) into a recursion relation for the eigenfunctions $P_{\ell}^{m}[\lambda_k^{(z)}]$, as before (see Appendix). We find that we can form the same recursion formula for the $P_{\ell}^{m}[\lambda_k^{(z)}]$ as in the one dimensional case - that is, the $P_{\ell}^{m}[\lambda_k^{(z)}]$ are invariant for the one dimensional and two dimensional problems. We may, therefore, determine the eigenvalues $\lambda_k^{(z)}$ and the eigenfunctions $P_{\ell}^{m}[\lambda_k^{(z)}]$ by the same methods presented previously.

5.3.4 Boundary Conditions at the Outer Surface

As was written previously, the form of the approximation to the intensity is

$$I(\vec{\tau},\vec{\Omega}) = \sum_{\ell=0}^{\infty} \sum_{m=-\ell}^{\ell} I_{\ell}^{m}(\vec{\tau}) Y_{\ell}^{m}(\vec{\Omega}) + B_{\nu}(T)$$

Substituting in the expression for $I_{\ell}^{m}(\vec{\tau})$, Eq. (5-79), we have

$$I(\vec{\tau},\vec{\Omega}) = \sum_{\ell=0}^{\infty} \sum_{m=-\ell}^{\ell} \sum_{\lambda_k(z)} P_\ell^m[\lambda_k^{(z)}] \sum_n \left\{\left[\frac{I_{n+m}[\frac{\tau}{\lambda_k(z)}] + I_{n-m}[-\frac{\tau}{\lambda_k(z)}]}{2}\right]\right.$$

$$\cdot [A_n[\lambda_k^{(z)}]\cos(n\phi_r) + B_n[\lambda_k^{(z)}]\sin(n\phi_r)]$$

$$+ i \left[\frac{I_{n+m}[\frac{\tau}{\lambda_k(z)}] - I_{n-m}[\frac{\tau}{\lambda_k(z)}]}{2}\right][B_n[\lambda_k^{(z)}]\cos(n\phi_r)$$

$$\left. - A_n[\lambda_k^{(z)}]\sin(n\phi_r)]\right\} Y_\ell^m(\vec{\Omega}) + B_\nu(T) \; . \tag{5-80}$$

For example, the expansion for the third order approximation is straightforward but tedious and is written

$$I(\vec{\tau},\vec{\Omega}) = B_\nu(T)$$

$$+ \sum_{\lambda_k(z)} \sum_n I_n[\frac{\tau}{\lambda_k(z)}][A_n[\lambda_k^{(z)}]\cos(n\phi_r) + B_n[\lambda_k^{(z)}]\sin(n\phi_r)$$

$$\cdot P_0^0[\lambda_k^{(z)}]Y_0^0(\vec{\Omega}) + P_1^1[\lambda_k^{(z)}]\left[\frac{I_{n+1}[\frac{\tau}{\lambda_k(z)}] + I_{n-1}[\frac{\tau}{\lambda_k(z)}]}{2}\right]$$

$$\cdot [A_n[\lambda_k^{(z)}]\cos(n\phi_r) + B_n[\lambda_k^{(z)}]\sin(n\phi_r)][Y_1^1(\vec{\Omega}) - Y_1^{-1}(\vec{\Omega})]$$

$$+ P_1^1[\lambda_k^{(z)}]\left[\frac{I_{n+1}[\frac{\tau}{\lambda_k(z)}] - I_{n-1}[\frac{\tau}{\lambda_k(z)}]}{2}\right][B_n[\lambda_k^{(z)}]\cos(n\phi_r)$$

$$- A_n[\lambda_k^{(z)}]\sin(n\phi_r)][iY_1^1(\vec{\Omega}) + Y_1^{-1}(\vec{\Omega})] + P_2^0[\lambda_k^{(z)}] I_n[\frac{\tau}{\lambda_k(z)}]$$

$$\cdot \left[A_n[\lambda_k^{(z)}]\cos(n\phi_r) + B_n[\lambda_k^{(z)}]\sin(n\phi_r)\right]\left[Y_2^0(\vec{\Omega})\right]$$

$$+ P_2^2[\lambda_k^{(z)}]\left[\frac{I_{n+2}[\frac{\overline{\tau}}{\lambda_k^{(z)}}] + I_{n-2}[\frac{\overline{\tau}}{\lambda_k^{(z)}}]}{2}\right][A_n[\lambda_k^{(z)}]\cos(n\phi_r)$$

$$+ B_n[\lambda_k^{(z)}]\sin(n\phi_r)]\left[Y_2^2(\vec{\Omega}) + Y_2^{-2}(\vec{\Omega})\right] + P_2^2[\lambda_k^{(z)}]$$

$$\cdot\left[\frac{I_{n+2}[\frac{\overline{\tau}}{\lambda_k^{(z)}}] - I_{n-2}[\frac{\overline{\tau}}{\lambda_k^{(z)}}]}{2}\right][B_n[\lambda_k^{(z)}]\cos(n\phi_r) - A_n[\lambda_k^{(z)}]\sin(n\phi_r)]$$

$$\cdot\left[i(Y_2^2(\vec{\Omega}) - Y_2^{-2}(\vec{\Omega}))\right] + P_3^1[\lambda_k^{(z)}]\left[\frac{I_{n+1}[\frac{\overline{\tau}}{\lambda_k^{(z)}}] + I_{n-1}[\frac{\overline{\tau}}{\lambda_k^{(z)}}]}{2}\right]$$

$$\cdot\left(A_n[\lambda_k^{(z)}]\cos(n\phi_r) + B_n[\lambda_k^{(z)}]\sin(n\phi_r)\right)\left[Y_3^1(\vec{\Omega}) - Y_3^{-1}(\vec{\Omega})\right]$$

$$+ P_3^1[\lambda_k^{(z)}]\left[\frac{I_{n+1}[\frac{\overline{\tau}}{\lambda_k^{(z)}}] - I_{n-1}[\frac{\overline{\tau}}{\lambda_k^{(z)}}]}{2}\right][B_n[\lambda_k^{(z)}]\cos(n\phi_r)$$

$$- A_n[\lambda_k^{(z)}]\sin(n\phi_r)]\left[i(Y_3^1(\vec{\Omega}) + Y_3^{-1}(\vec{\Omega}))\right] + P_3^3[\lambda_k^{(z)}]$$

$$\cdot\left[\frac{I_{n+3}[\frac{\overline{\tau}}{\lambda_k^{(z)}}] + I_{n-3}[\frac{\overline{\tau}}{\lambda_k^{(z)}}]}{2}\right][A_n[\lambda_k^{(z)}]\cos(n\phi_r) + B_n[\lambda_k^{(z)}]\sin(n\phi_r)]$$

$$\cdot \; [Y_3^3(\vec{\Omega}) - Y_3^{-3}(\vec{\Omega})] + P_3^3[\lambda_k^{(z)}][\frac{I_{n+3}[\frac{\tau}{\lambda_k^{(z)}}] - I_{n-3}[\frac{\tau}{\lambda_k^{(z)}}]}{2}]$$

$$\cdot \; [B_n[\lambda_k^{(z)}] \cos(n\phi_r) - A_n[\lambda_k^{(z)}] \sin(n\phi_r)][i(Y_3^3(\vec{\Omega}) + Y_3^{-3}(\vec{\Omega}))] \quad .$$

$$(5-81)$$

Note that we have used the relationship

$$P_\ell^m[\lambda_k^{(z)}] = (-1)^m \; P_\ell^{-m}[\lambda_k^{(z)}]$$

to simplify the expansion.

Eq. (5-81) may be further simplified by collecting common factors to

$$B_\nu(T) \; +$$

$$+ \; \frac{\bar{\lambda}_{(z)}}{\lambda_k^{(z)}} \; \sum_n [A_n[\lambda_k^{(z)}] \cos(n\phi_r) + B_n[\lambda_k^{(z)}] \sin(n\phi_r)]$$

$$\cdot \; \{ I_n[\frac{\tau}{\lambda_k^{(z)}}] \; P_0^0[\lambda_k^{(z)}] \; Y_0^0(\vec{\Omega}) + P_1^1[\lambda_k^{(z)}][\frac{I_{n+1}[\frac{\tau}{\lambda_k^{(z)}}] + I_{n-1}[\frac{\tau}{\lambda_k^{(z)}}]}{2}]$$

$$\cdot \; [Y_1^1(\vec{\Omega}) - Y_1^{-1}(\vec{\Omega})] + P_2^0[\lambda_k^{(z)}][I_n[\frac{\tau}{\lambda_k^{(z)}}] \; Y_2^0(\vec{\Omega}) + P_2^2[\lambda_k^{(z)}]$$

$$\cdot \; [\frac{I_{n+2}[\frac{\tau}{\lambda_k^{(z)}}] + I_{n-2}[\frac{\tau}{\lambda_k^{(z)}}]}{2}][Y_2^2(\vec{\Omega}) - Y_2^{-2}(\vec{\Omega})] + P_3^1[\lambda_k^{(z)}]$$

$$\cdot \; [\frac{I_{n+1}[\frac{\tau}{\lambda_k(z)}] + I_{n-1}[\frac{\tau}{\lambda_k(z)}]}{2}][Y_3^1(\vec{\Omega}) - Y_3^{-1}(\vec{\Omega})] + P_3^3[\lambda_k(z)]$$

$$\cdot \; [\frac{I_{n+3}[\frac{\tau}{\lambda_k(z)}] + I_{n-3}[\frac{\tau}{\lambda_k(z)}]}{2}][Y_3^3(\vec{\Omega}) - Y_3^{-3}(\vec{\Omega})] \; \}$$

$$+ \sum_{\lambda_k(z)} \sum_n [B_n[\lambda_k(z)] \cos(n\phi_r) - A_n[\lambda_k(z)] \sin(n\phi_r)]$$

$$\cdot \; \{ \; P_1^1[\lambda_k(z)][\frac{I_{n+1}[\frac{\tau}{\lambda_k(z)}] - I_{n-1}[\frac{\tau}{\lambda_k(z)}]}{2}][i(Y_1^1(\vec{\Omega}) + Y_1^{-1}(\vec{\Omega}))]$$

$$+ P_2^2[\lambda_k(z)][\frac{I_{n+2}[\frac{\tau}{\lambda_k(z)}] - I_{n-2}[\frac{\tau}{\lambda_k(z)}]}{2}][i(Y_2^2(\vec{\Omega}) - Y_2^{-2}(\vec{\Omega}))]$$

$$+ P_3^1[\lambda_k(z)][\frac{I_{n+1}[\frac{\tau}{\lambda_k(z)}] - I_{n-1}[\frac{\tau}{\lambda_k(z)}]}{2}][i(Y_3^1(\vec{\Omega}) + Y_3^{-1}(\vec{\Omega}))]$$

$$+ P_3^3[\lambda_k(z)][\frac{I_{n+3}[\frac{\tau}{\lambda_k(z)}] - I_{n-3}[\frac{\tau}{\lambda_k(z)}]}{2}][i(Y_3^3(\vec{\Omega}) + Y_3^{-3}(\vec{\Omega}))]$$

$$= I(\tau,\vec{\Omega}) \quad . \tag{5-82}$$

As in the one dimensional model, the outer boundary condition on this problem is that the "moments of flux" across the boundary are continuous. We, therefore, are led to multiply Eq. (5-82) by the

same weight functions as before and integrate over the domain of the

incident hemisphere. The right hand side of Eq. (5-82) will be the

assumed known incident intensity distribution. This intensity distri-

bution may be calculated by assuming that the infinite cylinder is

embedded in a non-scattering (clear atmosphere) plane parallel medium.

See Chapter 4 for details of clear column intensity calculations.

A double Gauss quadrature, utilizing 16 streams of intensity in each

angle (θ and ϕ mapped onto the interval (-1, 1)), was used to inte-

grate the right hand side of the equation after it was multipled by

the appropriate weight function. Note that multiplying the right hand

side by the weight function $\overline{Y}_1^1(\theta,\phi)$ and integrating over the domain

results in what we normally call the flux - but we will term it the

"first moment" of flux. $\overline{Y}_3^1(\theta,\phi)$ is the "second moment" of flux, and

so on, to avoid confusion. Calculations of the moments of flux were

performed at 18 equally spaced intervals on the cylinder wall between

0 and π. Recognizing that the incident moments of flux are periodic

in θ_r, and noting the form of the left hand side of Eq. (5-82), we

are lead to express the right hand side moments in a Fourier series.

In fact, the right hand side moments are even functions on (0, π) and

may be reduced to a set of cosine series. The right hand side moments,

therefore, may be written as

$$
\begin{array}{c}
\text{Right} \\
\text{Hand} \\
\text{Side}
\end{array}
= \left(d_0 + \sum_{n=1}^{\infty} d_n \cos(n\phi_r) \right) \overline{Y}_1^1(\theta,\phi); \; \overline{Y}_3^1(\theta,\phi); \; \text{etc.} \; . \; .
$$

The coefficients, d_0 and d_n, of the cosine series of each set of 18

moments were determined numerically (Powers, 1972) by the algorithms

$$d_0 = \frac{1}{s}(\frac{1}{2}f(x_0)+f(x_1)+\cdots+f(x_{s-1})+\frac{1}{2}f(x_s))$$

and

$$d_n = \frac{2}{s}(\frac{1}{2}f(x_0)+f(x_1)\cos\frac{n\pi}{a}x_1 +\cdots+ \frac{1}{2}f(x_s)(\cos\frac{n\pi}{a}x_s),$$

$$n=1,\cdots,s-1,$$

where the interval $(0,\pi)$ is divided into s equal subintervals with
endpoints $0=X_0$, X_1, $\cdots$, $X_s = \pi$. Returning our attention to the
left hand side of Eq. (5-82), we note that when we multiply by the
weight function and integrate over the incoming hemisphere (φ from
$\pi/2$, $3\pi/2$ and $\ominus$ from $0,\pi$), about half of the terms involve integra-
tions of the form

$$\int_{\pi/2}^{3\pi/2} \sin\phi \cos\varphi d\varphi \equiv 0.$$

In fact, these are the terms with the coefficient

$$\{ B_n[\lambda_k^{(z)}] \cos(n\phi_r) - A_n[\lambda_k^{(z)}] \sin(n\phi_r)\} .$$

For an example, we may now express the first moment of flux as

$$\int_{\pi/2}^{3\pi/2} \int_0^{\pi} Eq. (5-82). \overline{Y}_1^1(\ominus,\phi) \sin d\ominus d\phi = B_\nu(T) \overline{\overline{Y}_1^1 Y_0^0}$$

$$+ \sum_n \sum_{\lambda_k^{(z)}} [A_n[\lambda_k^{(z)}] \cos(n\phi_r) + B_n[\lambda_k^{(z)}] \sin(n\phi_r)]$$

$$\cdot P_0^0[\lambda_k^{(z)}] I_n[\frac{\tau}{\lambda_k^{(z)}}] \overline{\overline{Y}_1^1 Y_0^0} + P_1^1[\lambda_k^{(z)}][\frac{I_{n+1}[\frac{\tau}{\lambda_k^{(z)}}] + I_{n-1}[\frac{\tau}{\lambda_k^{(z)}}]}{2}]$$

$$\cdot \; \overline{Y_1^1 Y_1^1} + \cdots \cdots + P_5^5 [\lambda_k^{(z)}] [\frac{I_{n+5}[\frac{\tau}{\lambda_k(z)}] + I_{n-5}[\frac{-\tau}{\lambda_k(z)}]}{2}]$$

$$\cdot \; \overline{Y_5^5 Y_1^1} = [d_0 + \sum_{n=1}^{\infty} d_n \cos(n\phi_r)] \; \overline{Y_1^1}$$

where

$$\overline{Y_\ell^m Y_\alpha^\beta} = \int_{\pi/2}^{3\pi/2} \int_0^\pi [Y_\ell^m(\vec{\Omega}) + (-1)^m Y_\ell^{-m}(\vec{\Omega})][Y_\alpha^\beta(\vec{\Omega}) + (-1)^m Y_\alpha^{-\beta}(\vec{\Omega})] \sin\theta \, d\theta \, d\phi$$

Thus we see that Eq. (5-82) is a set of $\lambda_k^{(z)}$ simultaneous equations for any given n. We may determine the unknown constants by use of the orthogonality of the Fourier series. That is

$$A_0[\lambda_k^{(z)}] \;=\; \frac{1}{2\pi} \int_{-\pi}^{\pi} \text{Eq. (5-83)} \; d\phi_r$$

and

$$B_n[\lambda_k^{(z)}] \;=\; \frac{1}{\pi} \int_{-\pi}^{\pi} \text{Eq. (5-83)} \; \sin(n\phi_r) \; d\phi_r$$

and

$$A_n[\lambda_k^{(z)}] \;=\; \frac{1}{\pi} \int_{-\pi}^{\pi} \text{Eq. (5-83)} \; \cos(n\phi_r) d\phi_r \; . \qquad\qquad (5\text{-}83)$$

CHAPTER 6

COMPUTATIONAL RESULTS

6.1 Comparison with Cubic and Plane-Parallel Cloud Models in the Infrared

Calculations were performed using the two-dimensional infinite cylinder model. Mie theory was used to generate the single-scattering parameters for a typical water cloud at the chosen wavelength of 10 μm. Values employed were a single-scattering albedo, $\tilde{\omega}_\nu$, of .63 and coefficients, ω_ℓ, of the expansion of the phase function. The ω_ℓ are approximately 2.3, 3.4, 3.6, 3.4 and 2.7 for $\ell=1,5$. Note that absorption due to water vapor was not included in the infrared calculations.

Comparisons were made with two different models. Liou (1973) gave results for a plane-parallel cloud using the 16 stream discrete ordinate method. Liou and Ou (1979) presented calculations for radiative transfer in Cartesian coordinates for cubic and rectangular clouds. A spherical harmonics expansion of the scattering phase function and intensity was used for the finite clouds and the expansion was truncated at the first mode (e.g., $\ell=0,1$) and may be called a first-order solution.

Physically, both cloud models were assumed to be isothermal with temperature T_c and were situated above a horizontally infinite diffusely emitting plane whose temperature is T_s. Note that no atmosphere was present. The cylinder cloud, for comparison purposes, was configured in the same manner. Boundary conditions for the cylinder cloud were

calculated at a series of equally spaced points on a cylinder cross section as described in Chapter 5. Because the assumed black surface is the only source of radiation outside of the cloud, we see that the downward flux density will be zero at the cloud top point $(\phi_r=\pi)$, the upward flux density will be $\pi B_\nu(T_s)$ at the cloud bottom point $(\phi_r=0)$, and the flux density arriving on the circular side of the cloud will be a smooth function with values between 0 and $\pi B_\nu(T_s)$. Note that the cylinder cloud is situated in the atmosphere so that the polar angle, ϕ_r, equals zero at the nadir direction and π at the zenith direction.

Emergent intensity from the cloud models is a quantity of some theoretical interest. Liou and Ou (1979) presented average intensity values emerging from the top and bottom faces of cubic and rectangular clouds. These values were compared to emergent values from the plane-parallel cloud (Liou, 1973). The cloud top point and cloud bottom point are the only points on the cylinder cross section that lie in the same plane as the top and bottom "faces" of the other two models. Hence, the emergent values at those points were chosen for comaprison purposes. Figure 3 details the intensity (per units of $\pi B_\nu(T_s)$) from the cloud top and bottom as a function of emergent angle for vertical cloud optical depths of 1 and 10. Note that the fifth order intensity values are presented here. In each case the finite cloud models produced straight up values and straight down values that were larger and smaller, respectively, than the plane-parallel model. For upward emergent angles near 90°, each model predicted a smaller value than the plane-parallel cloud.

Remote sensing applications demand an average intensity value weighted over an area that is "seen" by an observer or satellite from
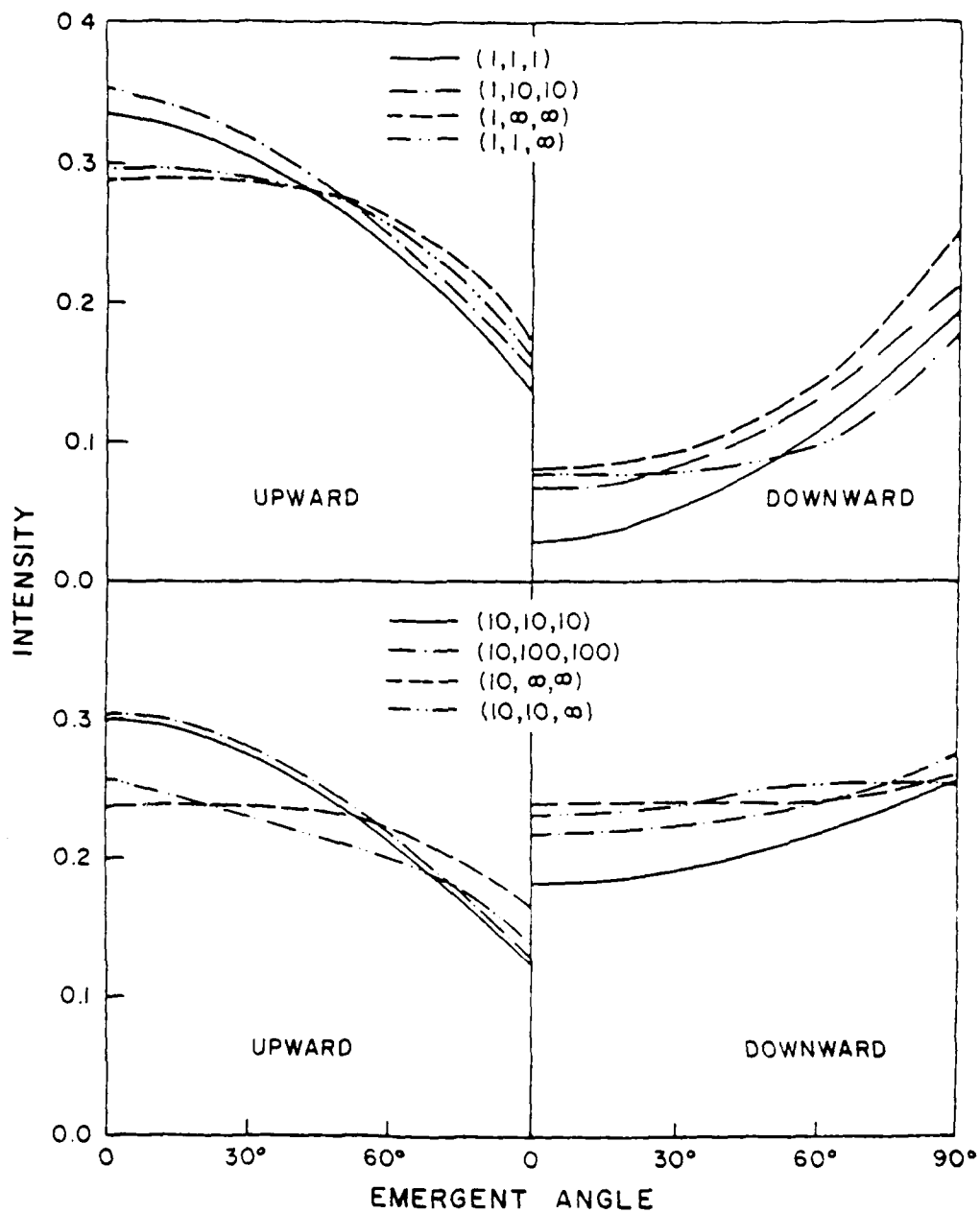
Figure 8. Incident intensity versus emergent angle per $^-B_\nu(T_s)$ in the upward and downward direction at 10 μm.

a far distance. Physically, then, a weighted average intensity would be the observed value. Because of the scanning method of infrared and microwave instruments, clouds may be viewed at several angles of observation. For example, a cloud viewed at 45° obviously will present a different surface than a cloud viewed at nadir. For this purpose we may define a weighted average

$$\bar{I}_w(\tau,\phi_r) = \sum_{i=1}^{N} I_i(\tau,\phi_r;\phi_i) \cdot w_i(\phi_i)$$

where $\bar{I}_w$ is the weighted average intensity, I_i are the N emergent intensity values in direction ϕ_r, the angle of observation, and ϕ_i are the equally spaced angles at which the emergent intensity values are chosen. Liou and Ou (1979) also define an area-weighted upwelling intensity emergent from the surface of a cubic cloud. Comparison of results of weighted average intensity calculations for different angles of observation are presented in Figure 9. Again, note that fifth order intensity solutions for the cylinder cloud are graphed for comparisons. The figures for optical depths 1 and 10 show that the weighted average intensity viewed at nadir for the cylinder cloud is much closer to the plane-parallel result than to the cubic cloud. The large value portrayed at nadir for the cubic cloud may be partially explained by recalling that the cubic cloud solution is only a first order approximation. A first order truncation of the cylinder weighted average intensity also produces a large value at nadir - equal to .375. Note also that a third order turncation produces a nadir value of .265 for the cylinder cloud, smaller than the fifth order solution. From this we may observe the expected oscillatory behavior of the spherical harmonics
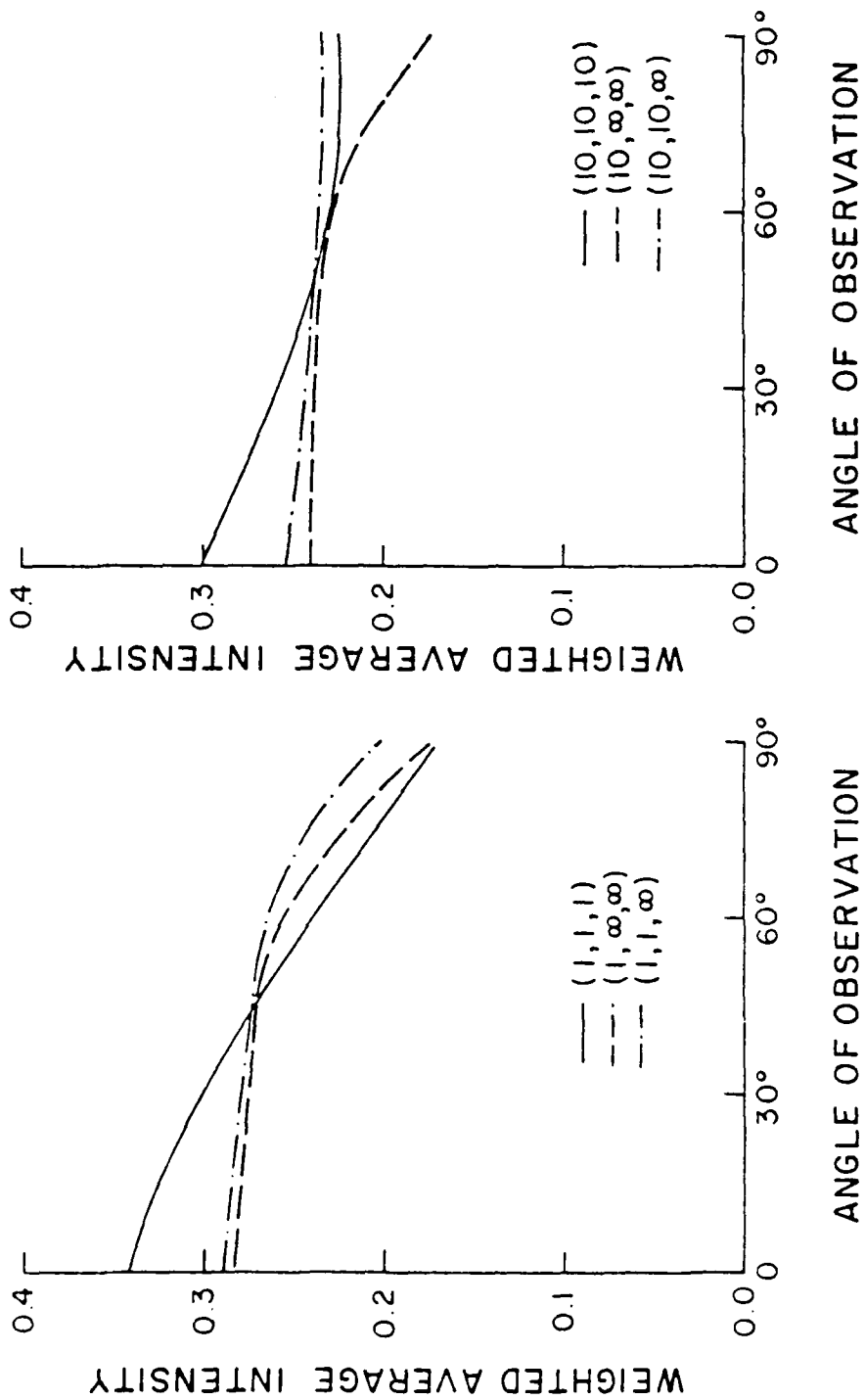
Figure 9. Weighted average intensity versus angle of observation at 10 μm.

solution. When the angle of observation approaches 45° we see that all of the models predict nearly the same value. Near 90° both the cylinder and cubic clouds exhibit similar behavior. As the optical depth of the cloud is increased, the multiple scattering and emission effects within the cloud manifest themselves in increased energy emerging from the sides of the cloud. Obviously these results must be tempered by the fact that we have not considered an intervening atmosphere between the cloud and the sensor. It does appear, however, that the relative observation angle and the cloud position within a sensor scan may be important in the remote sensing of cloud composition from satellite.

Another parameter of interest in infrared radiative transfer is cloud emissivity. Cloud emissivity may be investigated by removing the surface emission from the transfer equation. Effectively this means that the intensity incident on the boundaries of the cloud models is zero. Figure 10 shows the average emissivity, defined as the ratio of the average upward flux density to $\pi B_\nu(T_c)$, as a function of vertical optical thickness. Emissivity values were calculated for the first, third, and fifth order approximations to the cylinder cloud model. As we saw in the weighted average intensity calculations, the emissivity curves for the cylinder cloud manifest the expected oscillatory behavior due to the order of the spherical harmonic approximation. Since we would expect the fifth order emissivity to be slightly higher than the true value, and because the value of the fifth order emissivity approaches a number slightly less than 1, the cylinder model results tend to support the conjecture by Liou and Ou (1979) that clouds of finite extent should not be considered as black bodies even when their optical depths are large. Therefore, the cloud top temperatures inferred from
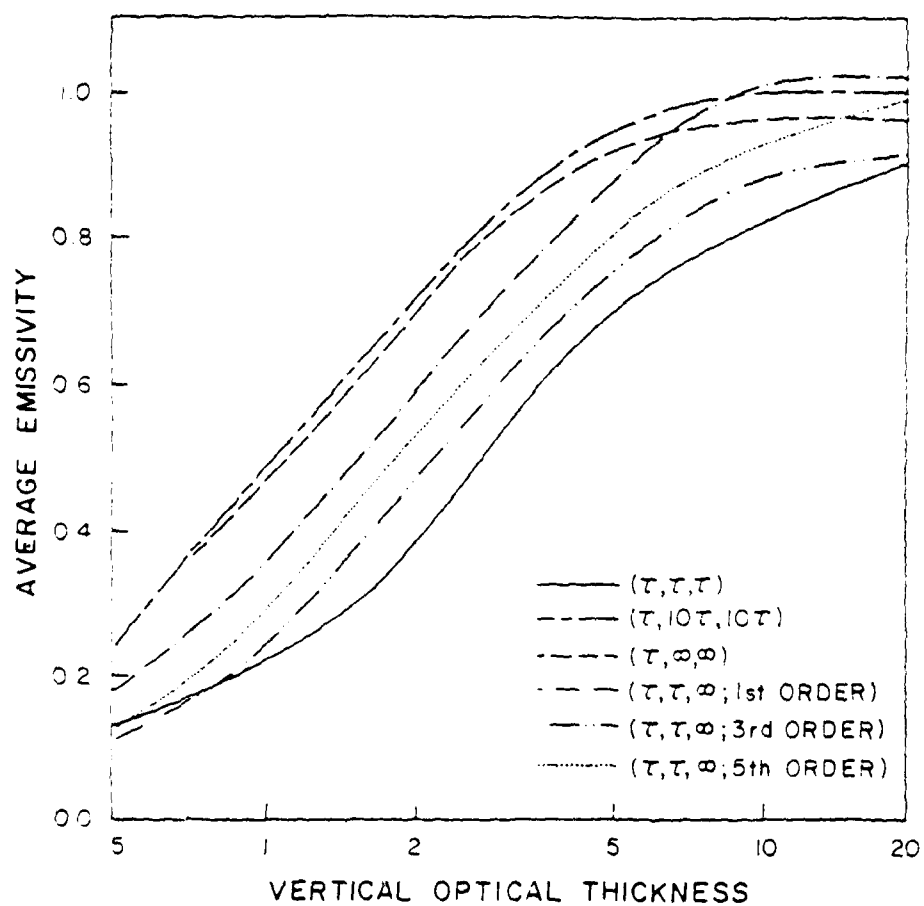
Figure 10. Average emissivity versus vertical optical thickness at 10 μm.

optically thick clouds, utilizing the 10 μm window, will be too high if the cloud emissivity is not accounted for.

6.2 Cylindrical Cloud Model Configuration in Realistic Atmospheres

The scattering, absorbing, and emitting cylinder is placed horizontally in an absorbing and emitting plane-parallel atmosphere. The surface of the Earth is assumed to be a horizontal plane of infinte extent that emits diffusely. Since we have assumed an infinite cylinder, each cross section of the cylinder is like any other and we may look at one such cross section. Calculations for the boundary conditions were performed at 18 points for $0 \leq t_r \leq \pi$, where $t_r = 0$ is the nadir direction with respect to the cloud and $t_r = \pi$ is the zenith direction. In general one could place a tangent plane on the cylinder, find streams of intensity at various Gauss latitudes in ϕ and θ and integrate using Gauss Quadrature to find the inward moments of flux. The problem is simplified somewhat by the infinite cylinder and plane parallel atmosphere assumptions. As a result, by taking into account the position angle, t_r, we may project onto the cross section plane and find the stream angle through the plane-parallel atmosphere that we need. We may now proceed to calculate the intensities in those stream angles.

The intensities in each stream are now calculated in much the same manner as in the boundary conditions for the plane parallel model with some minor difference due to the position of each tangent to the cylinder cross section. Figure 11 illustrates the geometry and it is seen that only the very top point will have no streams that contain surface effects, and that only the very bottom point will have no streams due to the atmosphere only. The incoming streams of intensity for the very

TOP OF ATMOSPHERE

$$\phi_r = \frac{\pi}{2}$$

EARTH'S SURFACE
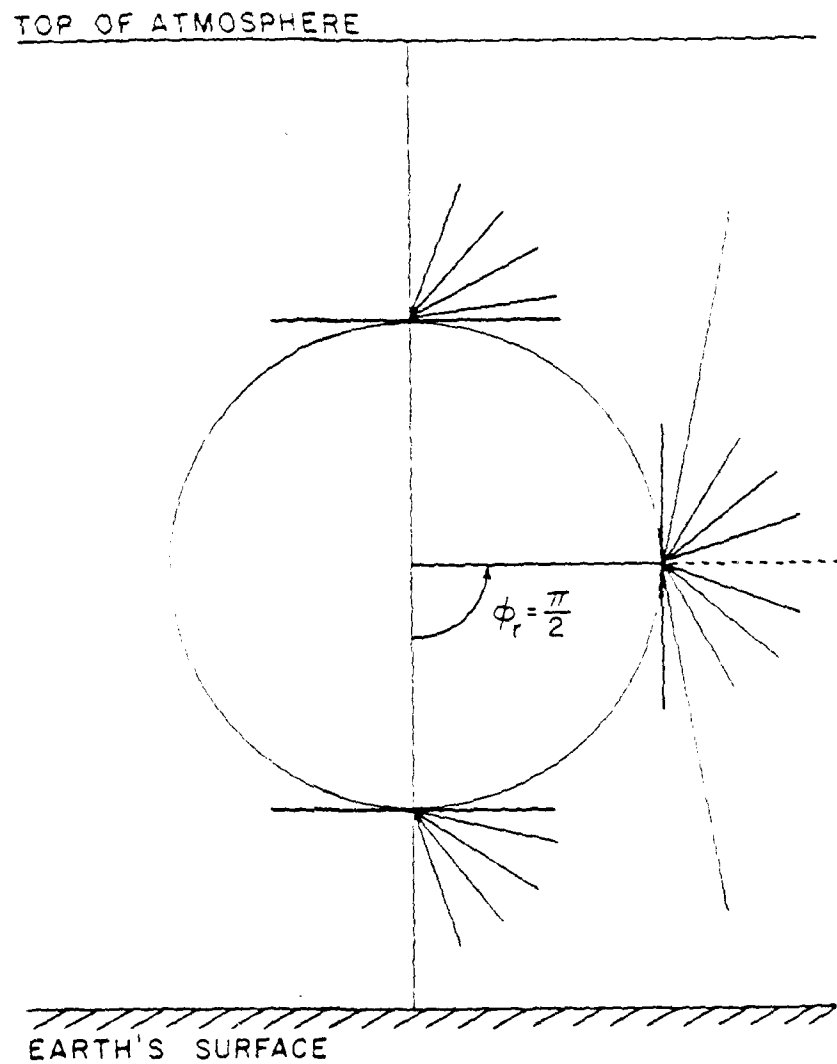
Figure 11. Representation of incoming intensity streams on a
cylinder cross-section.

bottom and very top points, then will be exactly the same as those in the plane parallel cloud model. The brightness temperature arriving at a point of height Z in a stream of angle greater than $\theta_p = \pi/2$ may be written

$$T_B(\nu,z_p;-\mu_i) = \int_{z=z_p}^{\infty} T(z)dT_\nu(z,z_p;-\mu_i)$$

where z_p is the height of the point in question and the negative sign on μ_i simply indicates downward transfer through the atmosphere. Once again, note that

$$T_\nu(z_p,z;-\mu_i) = T_\nu(z,z_p;-\mu_i) = \exp[-(\tau_p-\tau)/\mu_i]$$

and

$$T_\nu(z_1,z_2;-\mu_i) = T_\nu(z_1,\infty;-\mu_i)/T_\nu(z_2,\infty;-\mu_i)$$

where $z_2 > z_1$.

The brightness temperature arriving in a stream of angle less than $\theta_p = \pi/2$ may be written as

$$T_B(\nu,z_p;-\mu_i) = \epsilon_\nu T_s T_\nu(0,z_p;-\mu_i) + \int_{z=0}^{z_p} T(z)dT_\nu(z;z_p;-\mu_i)$$

$$+ (1-\epsilon_\nu)T_\nu(0,z_p;-\mu_i)\int_{z=\infty}^{0} T(z)dT_\nu(z,0;-\mu_i) \;,$$

which include terms for surface emission, atmospheric emission, and surface reflection.

As we may imagine in a real atmosphere, there is a substantial gradient in the values of intensity near $\theta_p = \pi/2$, the transition from

an intensity stream with three components to a stream with only one
component. To adequately represent this gradient, 16 Gauss nodes were
chosen in both θ and φ angles resulting in 128 different streams in φ
for each point. These intensity values were then related to each θ, φ
pair and after multiplying by the appropriate weight function (as de-
scribed before), we integrate utilizing a double Gauss quadrature to
get the moments of flux.

6.3 Comparison with Plane-Parallel Model
for the DMSP Microwave Frequencies

Sensitivity studies were performed for microwave frequencies.
Cloud thickness of 1, 2, 3, 4 and 5 km were used in simulating rainfall
rates of 2, 3, 4, 5, 10, 15, 20, 25 and 30 mm/hr by use of the Marshall-
Palmer drop size distribution as described in Chapter 3. The cloud
base height was fixed at a height of 1 km.

The weighted average intensity for the cylinder model, as de-
scribed in the infrared study, was used to compare with plane-parallel
results with one modification. Since each equally spaced point in a
realistic atmosphere on the cylinder cross section is at a different
optical depth, the streams were attenuated to the top of the atmosphere
prior to applying the weighted average.

Figures 12, 13 and 14 display the variation of brightness tem-
peratures at nadir at the top of the atmosphere over land (ϵ=0.97) and
ocean (ϵ=-.51) surfaces for frequencies of 50.50, 53.20 and 54.35 GHz
(Channels 1-3), respectively. The cloud temperature is assumed to be
283.16°K in all cases. Note that brightness temperature at the top of
the atmosphere for a frequency of 54.90 GHz is affected almost negligi-
bly by the thickest cloud considered in this study. Also the weighting
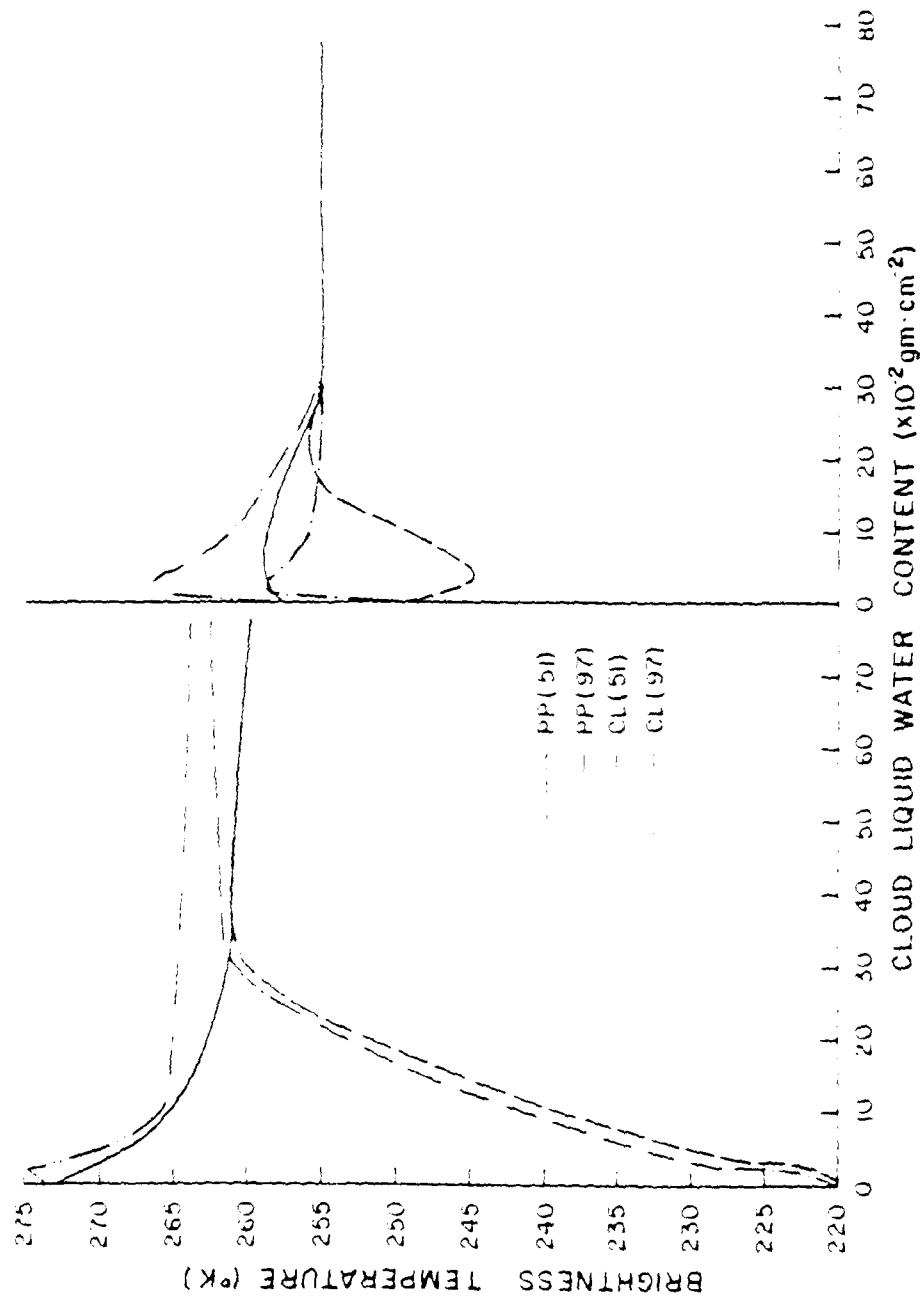
Figure 12. 50.50 GHz brightness temperature (nadir) for the plane-parallel (PP) and cylinder (CL) models over ocean ($\tau = .97$) ($T_{cloud} = 283.16°$ K)

Figure 13. 53.20 GHz brightness temperature (nadir) for the plane-parallel (PP) and cylinder (CL) models over ocean ($\tau = .51$) and land ($\tau = .97$). ($T_{cloud} = 283.16°$ K)

CLOUD LIQUID WATER CONTENT (×10⁻² gm·cm⁻²)

BRIGHTNESS TEMPERATURE (°K)

PP(51)
PP(97)
CL(51)
CL(97)
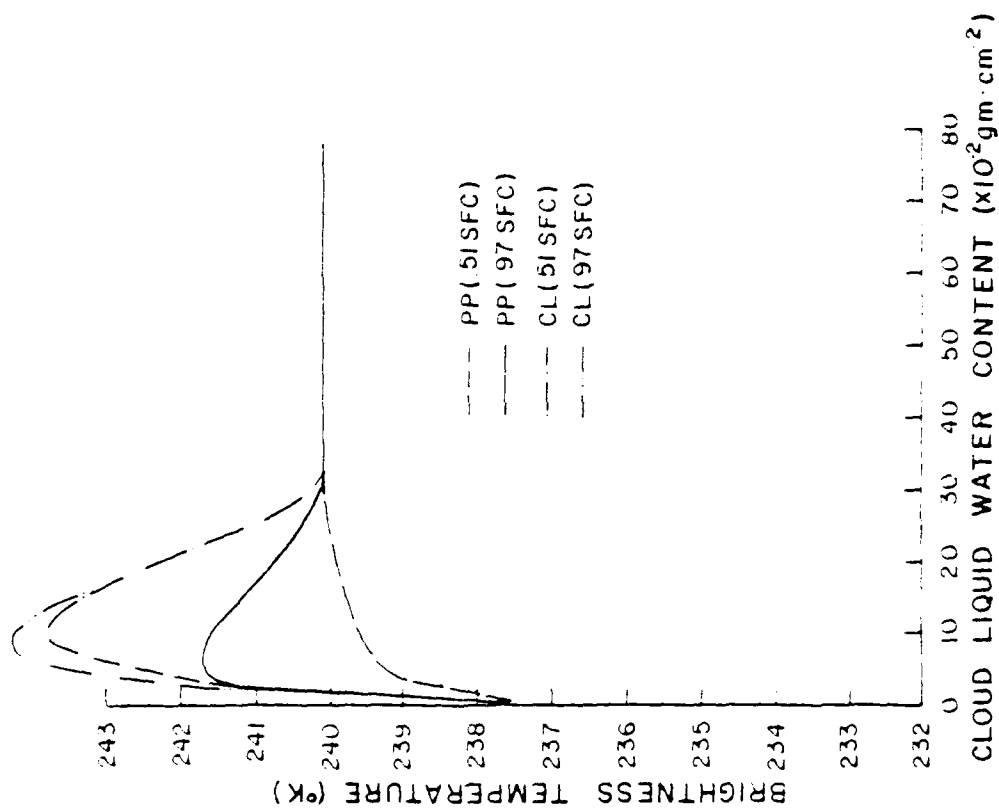
Figure 14. 54.35 GHz brightness temperature (nadir) for the plane-parallel (PP) and cylinder (CL) models over ocean ($\epsilon = .51$) and land ($\epsilon = .97$). ($T_{cloud} = 283.16°$ K).

functions of frequencies 58.40, 58.82, and 59.40 GHz peak sufficiently high in the atmosphere that their brightness temperatures are not affected by cloud models. Therefore, we have chosen not to include these frequencies in the sensitivity studies. For convenience, the abbreviations PP and CL will be used when referencing the plane-parallel and cylinder models, respectively.

At 50.50 GHz over land (Figure 12), the CL model displays an initial rise in brightness temperature (T_B) for very small liquid water contents, followed by a sharp drop, and then levels off to a slightly decreasing trend. The T_B finally reaches a value of 263.8 at a liquid water content of .7742 gm cm^{-2}. This liquid water content corresponds to the most optically thick cloud modeled - a 5 km cloud with a rainfall rate of 30 mm/hr. The PP model responds similarly to the CL model over a land surface. There is no initial rise in the T_B values, however, and the final T_B value reached is near 259.85, a difference of approximately 4.

Over ocean, the 50.50 GHz frequency values (Figure 12) for both models experience a strong rise from the clear column. The CL model, as in the land case, has a higher value throughout the spectrum of liquid water contents. The difference in the two models appears to be largest at .7742 gm cm^{-2} - a T_B difference of approximately 3.

At 53.20 GHz (Figure 13), the T_B differences between the two models for large liquid water contents is practically negligible. There are some differences in response, however, for liquid water contents of less than .30 gm cm^{-2}. Over land, both models show an initial rise in T_B from the clear column value but the CL model's rise is much larger (about T_B=8). Over water, the PP model drops sharply and then

rises to become larger in value than the CL model (about $T_B=$') near a liquid water content of .15 gm cm^{-2} before reaching nearly the same value at .30 gm cm^{-2}. The T_B value for the CL model over water rises initially to a peak value of near 259. and then drops slowly to the values of the other curves.

At 54.35 GHz (Figure 14), the response of the T_B to varying cloud thicknesses and rainfall rates is much less than for the 50.50 and 53.20 GHz frequencies. Note that the scale for the T_B has been considerably reduced. The behavior of this frequency is similar to 53.20 GHz in that the responses to the various forcing functions reaches a near equilibrium value at a liquid water content of .30 gm cm^{-2}. Below .30 gm cm^{-2}, however, we do see some differences. The CL model over both surfaces experiences an initial rise from the clear column value of T_B of approximately 7. The PP model over land also shows this initial rise in T_B but on the order of 4. The T_B of the PP model over ocean gradually rises to the equilibrium value near .30 gm cm^{-2} liquid water content.

Note that the only change in the transfer model between the ocean and land cases studies is a change in the surface emissivity - assumed for the comparison to be .97 for a land surface and .51 for an ocean surface. This change of surface emissivity essentially affects two of the boundary conditions: 1) the surface emission and 2) the atmospheric contribution reflected from the Earth's surface, which is approximately 16 times greater over ocean than land. Note also that the 50.50 GHz frequency over ocean results for both models are generally higher than the clear column value and under score the usefulness of this frequency in "flagging" cloudy conditions that may cause a deterioration

in the accuracy of temperature retrievals based on microwave sounder data.

6.4 Interpretation of Results from Cylindrical Cloud Model

This section will address several different topics. First the cloud top brightness will be split into its various components in an attempt to discern why the CL model responds as it does. Next the average intensity at the top of the atmosphere will be treated from the remote sensing point of view. The third topic focuses on the importance of multiple scattering in the DMSP microwave frequencies. Finally the spherical harmonic solutions of different orders are analyzed with zero boundary conditions.

Figure 15 snows in a general way what mechanisms are at work to cause energy gain and loss within a cylindrical cloud. Energy gains are realized from multiple scattering, droplet and gaseous emission. Energy is lost from the discrete streams emerging from the cloud from droplet and gaseous absorption and single scattering. The interplay of these mechanisms determines the solutions emerging from the cylinder. The forcing functions on the problem are the temperature of the cloud, through the Planck function, and the boundary radiation streams that illuminate the cylinder.

To detail how the cloud interacts with the clear column atmosphere, we examine the three contributors to cloud brightness temperature: 1) emission by the Earth's surface, 2) atmospheric emission, and 3) emission from within the cloud. We may examine the effect of each of these terms independently by "turning off" two of the three contributions simultaneously. This may be accomplished by 1) eliminating the surface
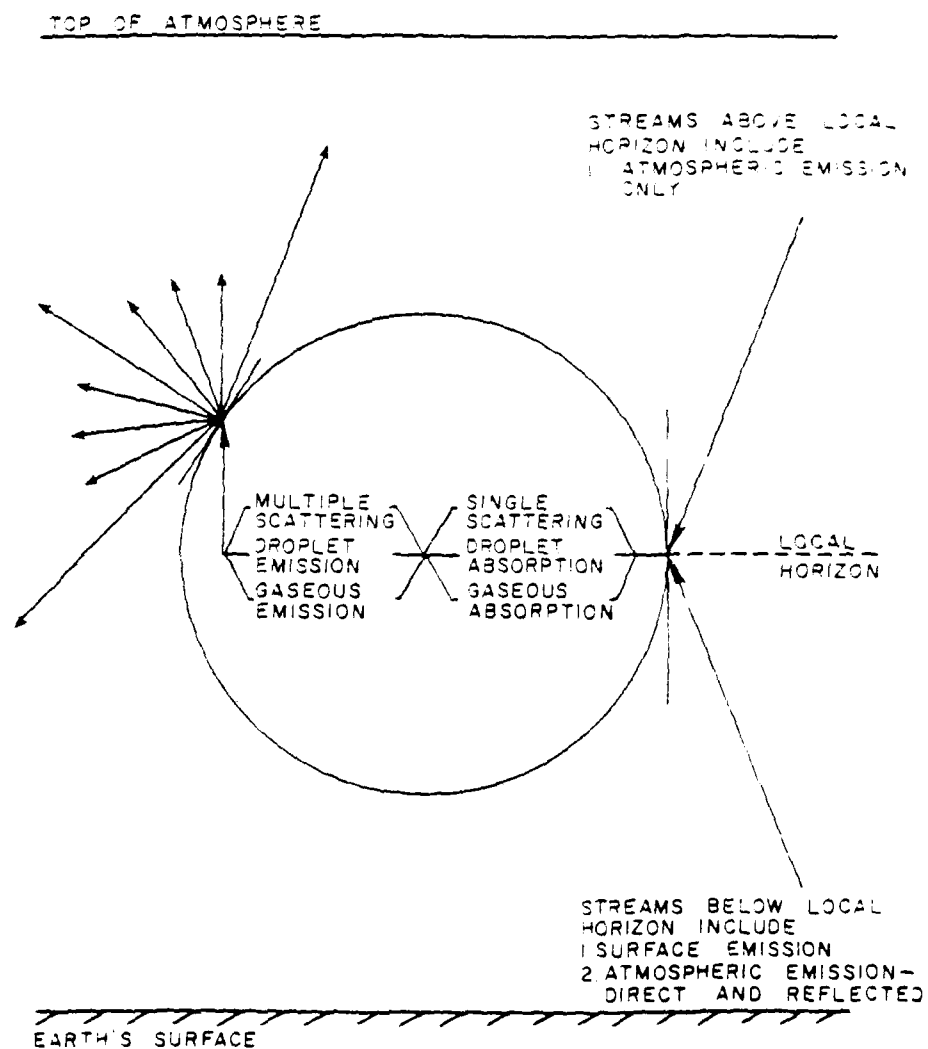
Figure 15. Representation of radiative transfer in a cylindrical cloud.

emission contribution from the below-the-horizon streams of intensity
in the boundary conditions, 2) setting the atmospheric contribution to
zero, and 3) setting the temperature of the cloud to $0^\circ K$.

Figures 16 and 17 present the component contributions to cloud top
brightness for 50.50 GHz for the CL and PP models, respectively. Note
that all values are fifth order solutions. Results are presented for
a 5 km thick cloud with a temperature fixed at $283.16^\circ K$. Land ($\varepsilon=.37$)
and water ($\varepsilon=-.51$) surface calculations are graphed. Note that the
trends for all of the various components to cloud top brightness are
roughly the same for the CL and PP models. Minor differences in the
trends, however, may be used to explain the responses of the CL and PP
models seen previously in Figure 12. At liquid water contents greater
than .40 gm cm^{-2}, the cloud top brightness and the T_B decrease very
slowly. The solution due to the cloud alone is nearly constant in
both models. The difference is seen in the contributions from the sur-
face and atmospheric effects. The surface effect in the PP model is
effectively zero at cloud liquid water contents greater than .4 gm cm^{-2}.
The CL model, however, continues to show an effect due to the surface
throughout the spectrum of cloud liquid water contents. Similarly, the
atmospheric effect for the CL model at large liquid water contents is
slightly larger than the PP model. These contributions, plus the fact
that the CL cloud solution is approximately $3^\circ K$ higher than the PP
model explain the difference seen in this region in Figure 12. Below
.3 gm cm^{-2} cloud liquid water content, the atmospheric and surface
effects continue to have larger values for the CL model. These larger
values are partially offset since the PP model cloud solution rises
more quickly than the CL solution. The net effect, though, is for the
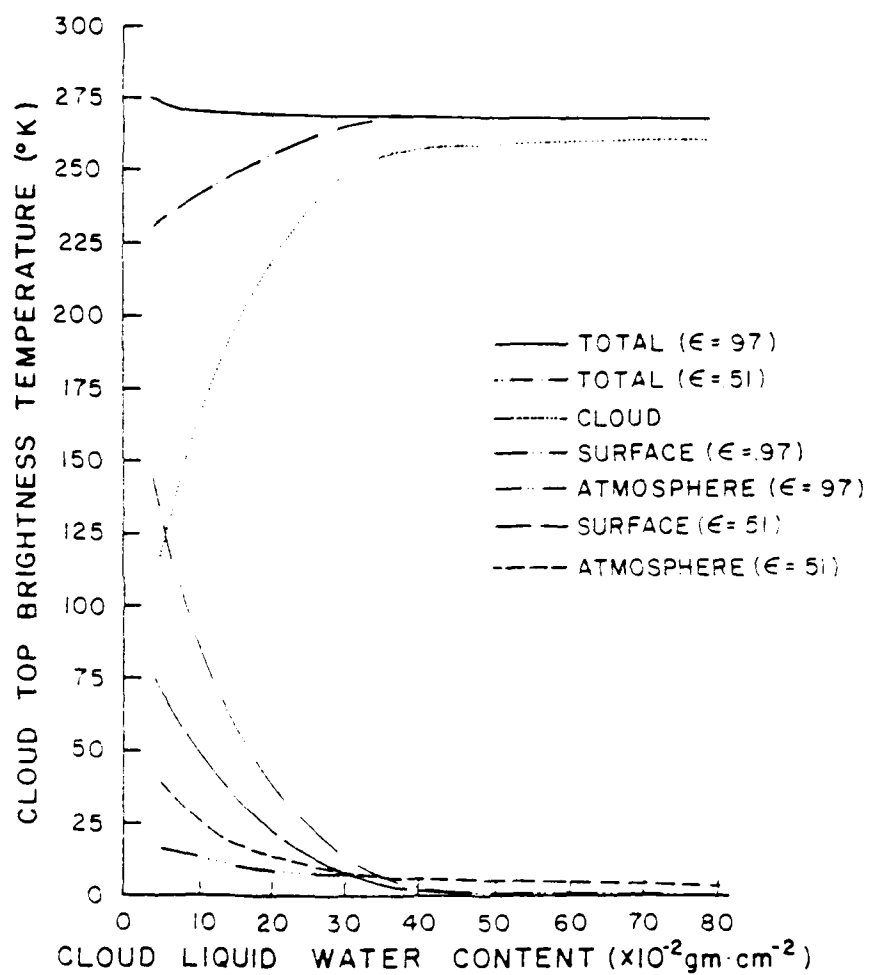
Figure 16. 50.50 GHz component contributions to cloud top brightness for a 5 km thick cylinder cloud. $T_{cloud}=283.16°$ K.

CLOUD TOP BRIGHTNESS TEMPERATURE (°K)

300 —
275 —
250 —
225 —
200 —
175 —
150 —
125 —
100 —
75 —
50 —
25 —
0 —

——— TOTAL (ε = 97)
·— — TOTAL (ε = 5)
········ CLOUD
— · — SURFACE (ε = 97)
— · — ATMOSPHERE (ε = 97)
——— SURFACE (ε = 5)
- - - - ATMOSPHERE (ε = 5)

0   10   20   30   40   50   60   70   80

CLOUD LIQUID WATER CONTENT (×10⁻²gm·cm⁻²)
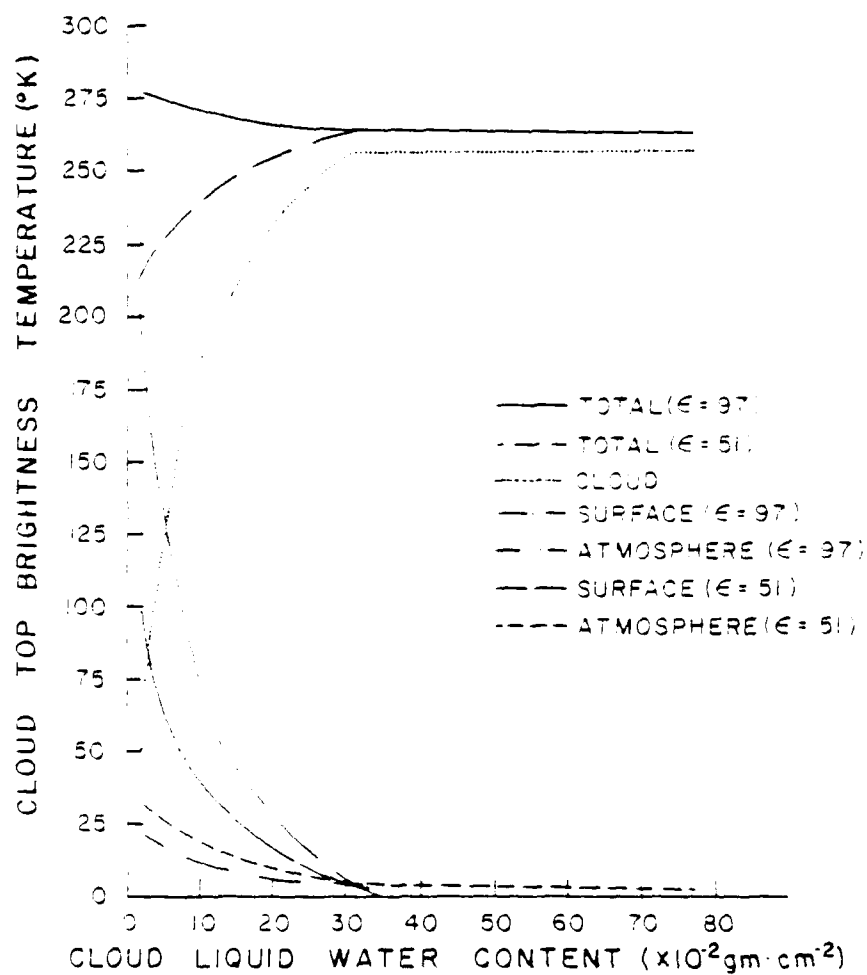
Figure 17. 50.50 GHz component contributions to cloud top brightness for a 5 km thick plane-parallel cloud. T_{cloud}=283.16° K.

CL total to be slightly larger than the PP total. At very small liquid water contents, the atmosphere and surface contributions for the CL model over a land surface do not drop fast enough to compensate for the rapid rise in the cloud solution. Therefore, we observe the initial rise in T_B to a value larger than clear column in this region.

Figures 18 and 19 present the component contributions to cloud top brightness for 53.20 GHz for the CL and PP models, respectively. As seen previously in Fig. 6, the solutions for cloud liquid water contents greater than .35 gm cm^{-2} are nearly identical for both models over both surfaces. For values less than .30 gm cm^{-2} there are graphic differences in the responses of the models. In Fig. 18 the CL model shows an initial rise from the clear column values over both surfaces, and then a drop toward the equilibrium position. These rises are seemingly caused by the observation that the slope of the CL atmospheric and surface solutions tends to be slightly more horizontal as the cloud liquid water content is reduced, while the cloud solution is rising most rapidly. As cloud liquid water is increased the slope of the atmospheric and surface graphs increase and cause the net solution to decrease slowly.

As discussed and defined previously in the infrared sensitivity study, an important parameter from a remote sensing point of view is the weighted average intensity, the intensity that an observer or satellite would see from a far distance. Figure 20 presents the weighted average brightness temperature at the top of the atmosphere as a function of the angle of observation for 6 km clouds of optical depth 3.6 and 12. over a land surface (fifth order solutions). Also presented in Fig. 20 are solutions for a plane-parallel cloud with the
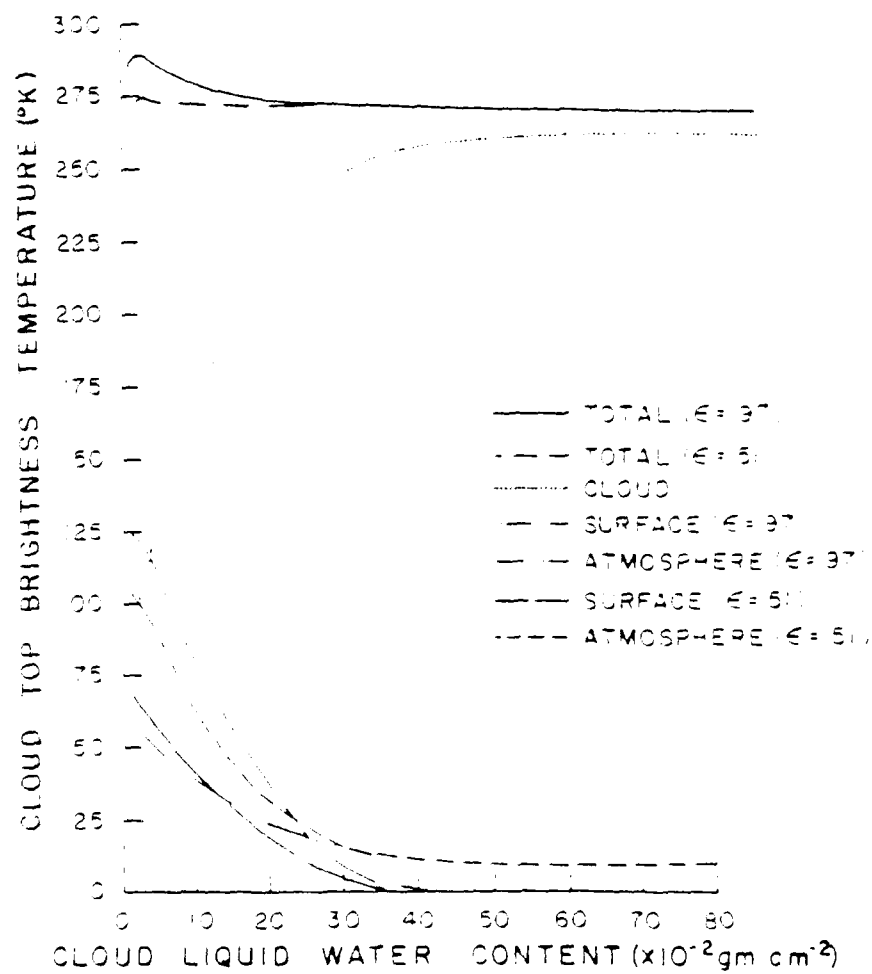
Figure 18. 53.80 GHz component contributions to cloud top brightness for a 5 km thick cylinder cloud. $T_{cloud}=293.16°$ K.
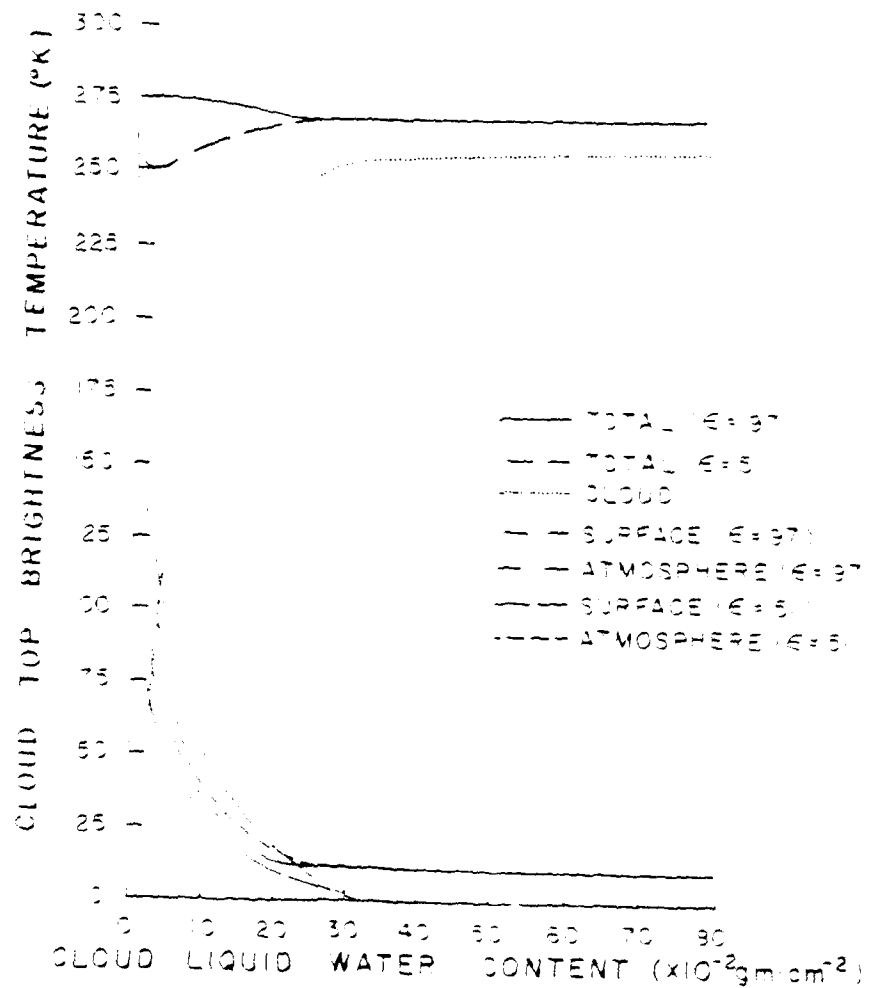
Figure 13. 53.20 GHz component contributions to cloud top brightness for a 5 km thick plane-parallel cloud. The cloud top
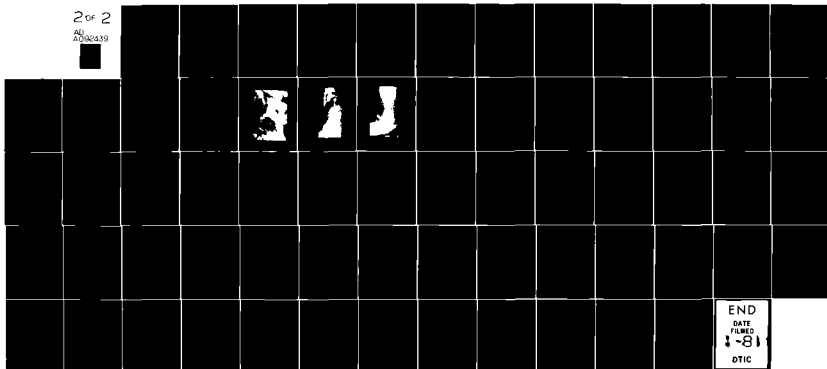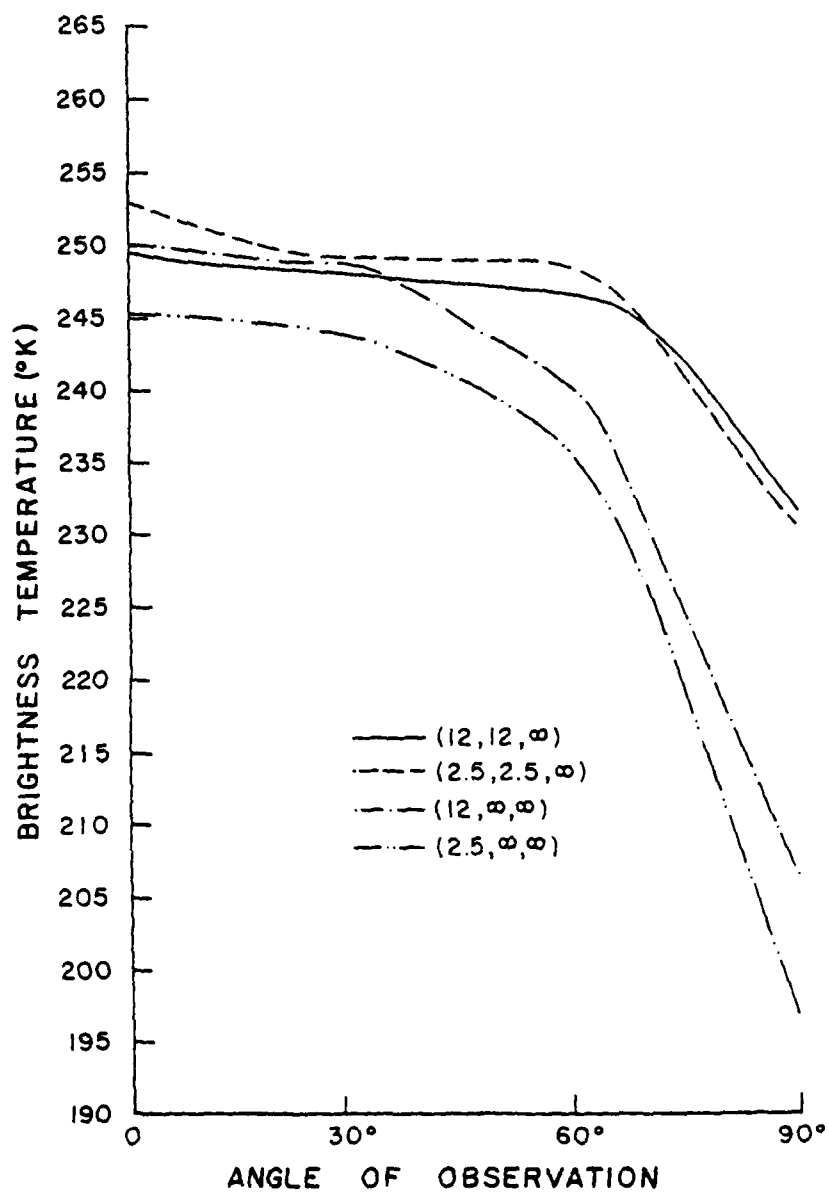
Figure 20. 50.50 GHz weighted average brightness temperature versus angle of observation at the top of the atmosphere. $\varepsilon=.97$. $T_{cloud}=265.41°$ K.

same configuration. The cloud temperature was assumed to be 265.41°K.
The CL solutions for both cloud optical thicknesses gradually decline
as the angle of observation increases to near 60° from nadir. From
60° to 90°, the CL values drop more rapidly, and the solution from the
optically thinner cloud, although higher in value from 0° to 60°, drops
below the solution of the optically thicker cloud. The PP cloud solu-
tions decline slowly to near 30° and then more quickly from 30° to
90°. At nadir-zenith we might expect, as discussed earlier in the IR
study, that the fifth order solution of average intensity for the CL
model might be slightly higher than the true value because of the
oscillation inherent in a spherical harmonics solution. The PP solu-
tion is 16th order and should be reasonably accurate for an infinite
slab. Between 60° and 90° the solution for the optically thick CL
cloud declines less rapidly than that of the optically thin cloud. The
net result is that at 90° the thick CL cloud has a higher solution.
The explanation may be found in Fig. 21. The CL values presented here
are intensities at the view angle, averaged as in the IR case. That
is, the intensity values are averaged without attenuation to the top
of the atmosphere and therefore represent an average intensity leaving
the cloud. It is apparent that the optically thick CL cloud has an
average intensity leaving the cloud that increases as the angle of
observation approaches 90°. The optically thin CL cloud solution de-
clines as the view angle approaches 90°. Apparently, as the CL cloud
optical depth is increased, the multiple scattering and emission
effects within the cloud begin to manifest themselves in increasing
amounts of energy emerging from the sides of the CL cloud. This effect
cannot be seen in the PP model because of its geometrical limitation.
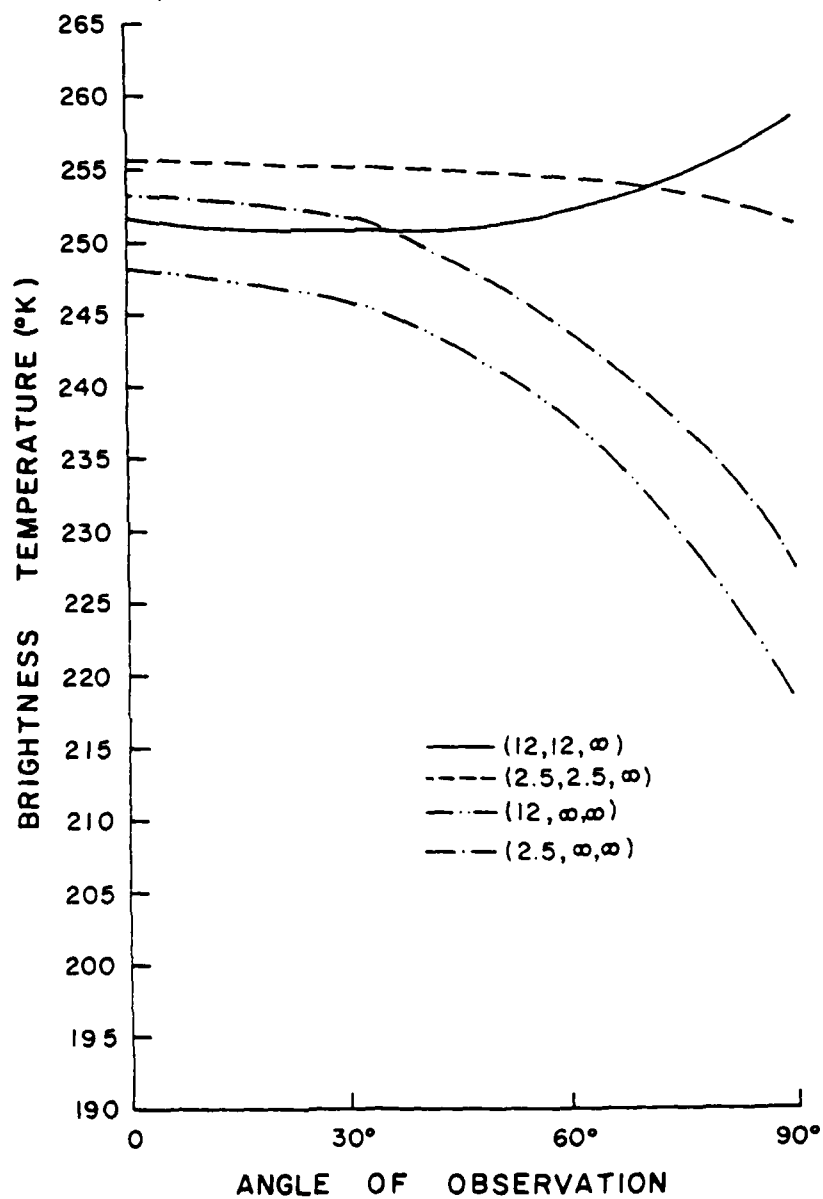
Figure 21. 50.50 GHz cloud average brightness temperature versus angle of observation. $\epsilon=.97$. $T_{cloud}=265.41°$ K.

Even though the fifth order solution from the optically thick CL cloud is rising near 90°, the corresponding brightness temperature at the top of the atmosphere is decreasing. The reason may be that the CL cloud is immersed in a clear plane-parallel atmosphere. Therefore, as the angle of observation approaches 90°, the amount of atmosphere slant path between the observer and the cloud approaches infinity. Therefore, the amount of energy reaching the observer from the cloud should approach zero. This effect is shown in Fig. 22 for a 5 km CL cloud of optical depth 12. Obviously for frequencies that fall at or near the absorption band center, the atmospheric optical depth between the cloud and the sensor is already so large that little or no energy from the cloud reaches the sensor. In "wing" and "window" frequencies, however, relative observation angle and cloud position within the sensor scan may be of importance in the remote sensing of cloud composition from satellite.

Discussion of the importance of multiple scattering in the DMSP microwave frequency region is of paramount importance because if there is little or no multiple scattering occurring, the solution of the PP model is greatly simplified. The equation of transfer in a plane-parallel atmospheric layer with no scattering may be written

$$I(\tau;\mu) = I(\tau_1;\mu)e^{-(\tau_1-\tau)/\mu} + \int_\tau^{\tau_1} B_\nu(T(\tau'))e^{-(\tau'-\tau)/\mu} \frac{d\tau}{\mu} .$$

The cloud is assumed isothermal and the source function, $B_\nu(T)$, may be removed from the integral and the solution to Eq.   may be written

$$I(\tau;\mu) = I(\tau_1;\mu)e^{-(\tau_1-\tau)/\mu} + B_\nu(T)[1-e^{-(\tau_1-\tau)/\mu}] .$$
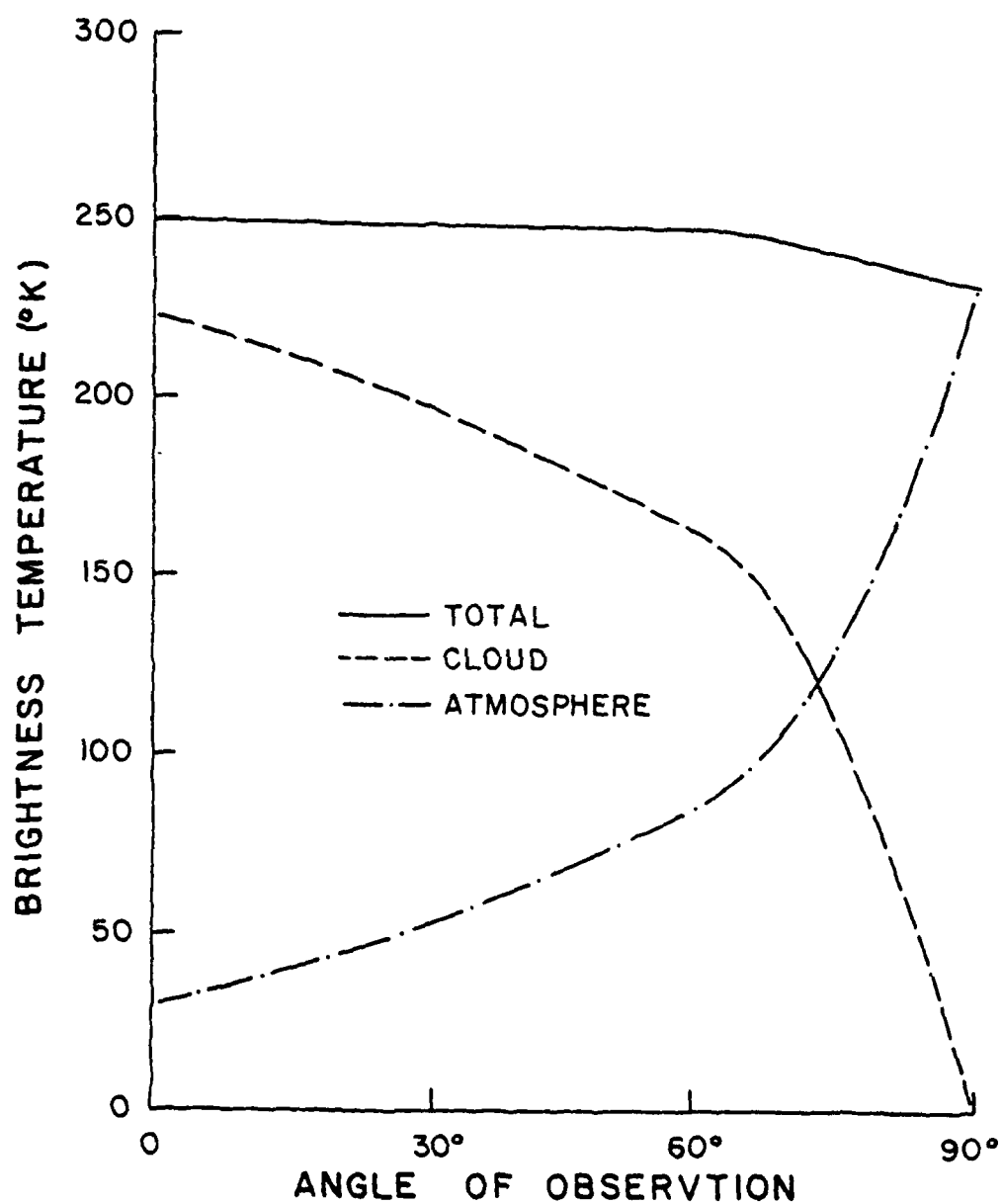
Figure 22. 50.50 GHz atmospheric and cloud contributions to brightness temperature versus angle of observation. $\tau=12$, $\varepsilon=.97$, and $T_{cloud}=265.41°$ K.

Note that at 90°, the solution becomes

$$I(\tau;\mu=0) = B_\nu(T).$$

Some additional physical insight may be gained from this solution. If the cloud optical depth is zero then the second term in the solution goes to zero and

$$I(\tau;\mu) = I(\tau_1;\mu).$$

When the cloud is optically thick the exponential factor approaches zero and the non-scattering solution again approaches the Planck function. Multiple scattering may be deleted from the CL model, also, but the problem's complexity is not appreciably reduced. The equation may be written

$$-\frac{1}{3_e} [\sin\theta\cos\phi\frac{\alpha}{\alpha r} - \frac{\sin\theta\sin\phi}{r} \frac{\alpha}{\alpha\phi_r}] I(\vec{r},\vec{\Omega}) = I(\vec{r},\vec{\Omega}) + B_\nu(T) .$$

Assuming the same expansion as before for the intensity we arrive at a recursion formula similar to Eq. (5-59). Using the method of selecting the zero and first order modes, we may continue with the same method to find a solution for $I_0^0(\rho,\phi_r)$. It appears that the major difference in the solution is in the eigenvalues, λ. With scattering, the first order approximation had

$$\lambda = \sqrt{\frac{1}{3(1-\tilde{\omega}_\nu)(1 - \frac{\tilde{\omega}_\nu\omega_1}{3})}} .$$

Without scattering the eigenvalue for the first order approximation becomes

$$\lambda = \sqrt{\frac{1}{3}} \quad ,$$

a constant.

The numerical program was modified to remove the multiple scattering term and Fig. 23 shows graphically the reduction in the fifth order solution of weighted average intensity from the cloud alone at a frequency of 50.50 GHz (zero outer boundary conditions) when multiple scattering is removed. It appears that the effect of multiple scattering is to increase the total brightness to near an optical depth of 10. At values of optical depth larger than 10 the curves nearly parallel each other with multiple scattering contributing a near constant additional 37% to the cloud brightness.

We discuss the results of the cloud alone, e.g., the boundary conditions are assumed zero and the cloud is given a temperature. Upon examining the character of the solution at several different points around the cylinder cross section, it was found that the emergent angular intensity distributions were identical. This demonstrates, as we might expect, that the cloud with zero outer boundary conditions emits isotropically.

Non-zero variably boundary conditions, then, will act as a forcing function on top of a constant solution. The amount of radiation emitted by the cloud is, of course, a function of the cloud composition.

Figures 24 and 25 present the variation of brightness temperature with emergent angle for the PP and CL models for two representative optical depths in the microwave region. Recall that in the PP (discrete ordinate) method, the solution is gotten explicitly at discrete emergent angles (Gauss nodes) and then a curve is fit through those
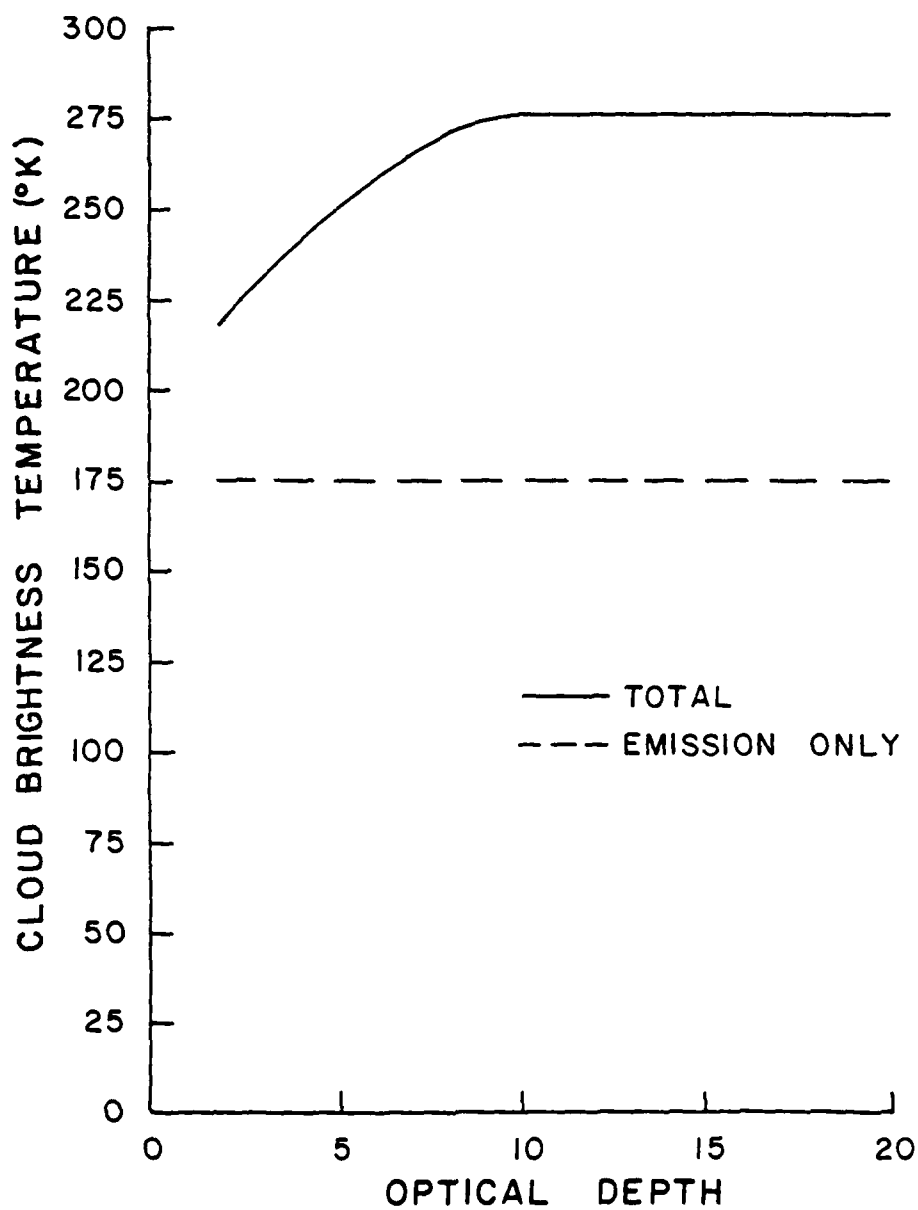
Figure 23. 50.50 GHz effect of removing multiple scattering from source function versus optical depth. Cloud only at $T_{cloud}=301°$ K.
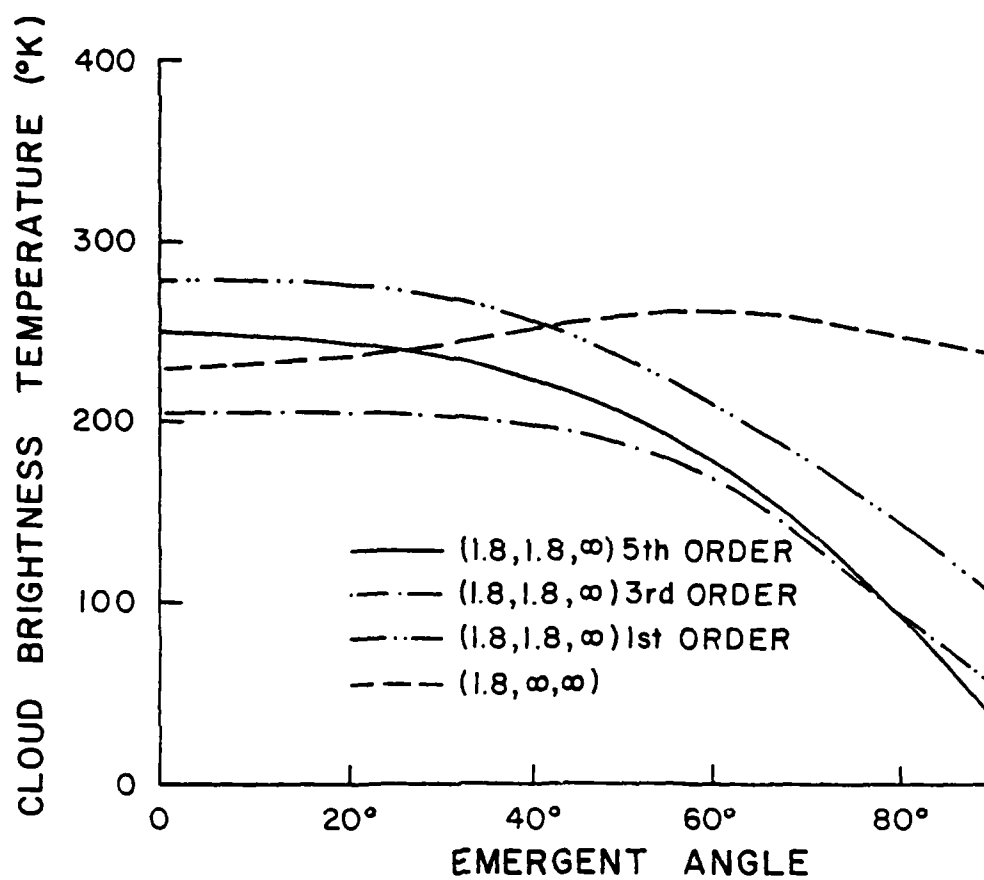
Figure 24. 50.50 GHz cloud brightness temperature versus emergent angle: zero outer boundary conditions. $T_{cloud}=301°$ K.
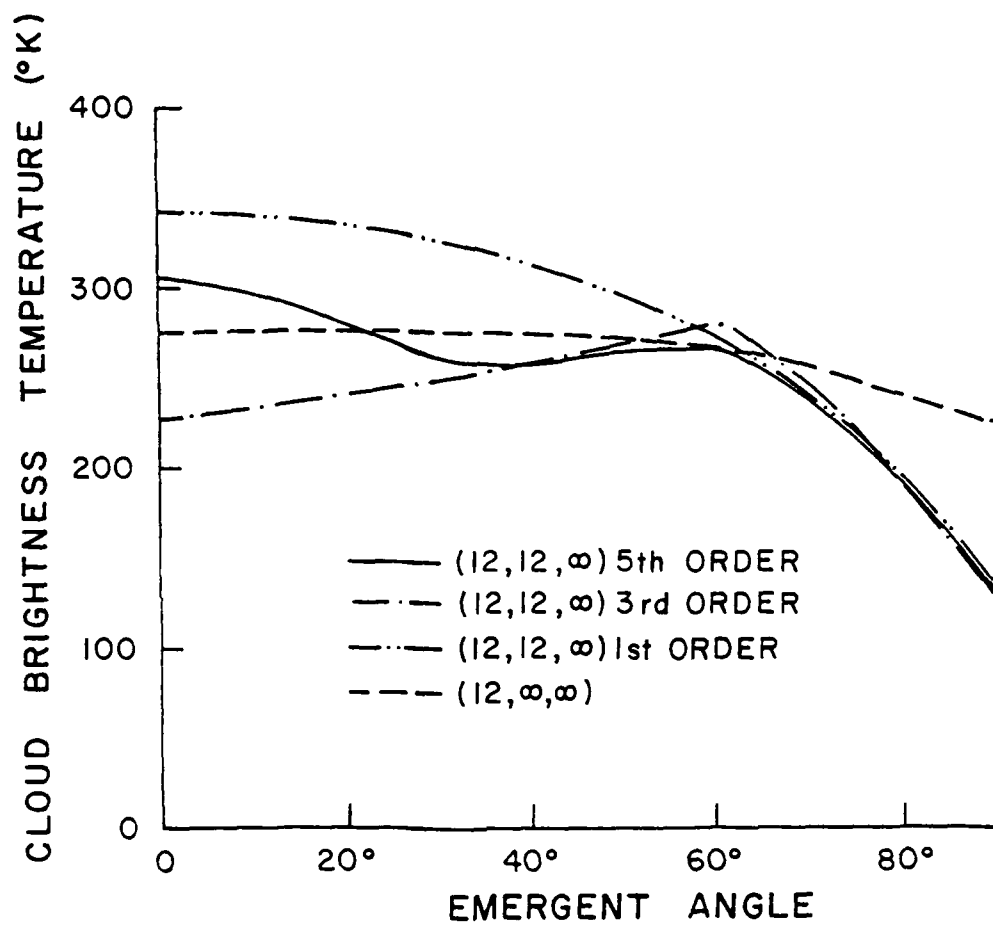
Figure 25. 50.50 GHz cloud brightness temperature versus emergent angle: zero outer boundary conditions. $T_{cloud}=301°$ K.

to extrapolate the 0° and 90° solutions. This method tends to present a smooth curve. The solution as described for the cylinder, at one point, is a series of spherical harmonic functions and will tend to have some oscillation, depending on the order of approximation used. Dave and Canosa (1974) presented results for a spherical harmonics approximation to plane-parallel atmospheric models. Their figures show a pronounced oscillation for a fifth order (so-called P_5) approximation for optical depths up to 1. The various orders of solutions for $\tau=1.8$ for the CL model have no oscillation and we begin to see some oscillation for the $\tau=12.$ curves. This slow onset of oscillatory behavior may be attributed to the form of the two dimensional solution. For example, please refer to Eq. 5-82, the 3rd order approximation written out explicitly. The solution is expressed in terms of various combinations of spherical harmonics (Eq. 5-57), all of which did not vanish when the emergent angle is equal to 90°. Therefore, the approximation renders a value at 90° which is other than zero. Also, the combination of the functions tends to damp the oscillation experienced by Dave and Canosa for low orders of approximation for plane parallel media.

Cloud emissivity for 50.50 GHz is presented in Fig. 25. The average emissivity values, defined as the ratio of the average outward flux denisty to $\pi B_\nu(T_c)$, are presented as a function of cloud optical thickness for first, third and fifth order approximations to the cylinder cloud model. The emissivity curves have essentially the same trends as presented in the infrared case study (Fig.10). Note, however, that the values are lower in the microwave region than in the infrared area for both models at very large optical thicknesses. Also the fifth
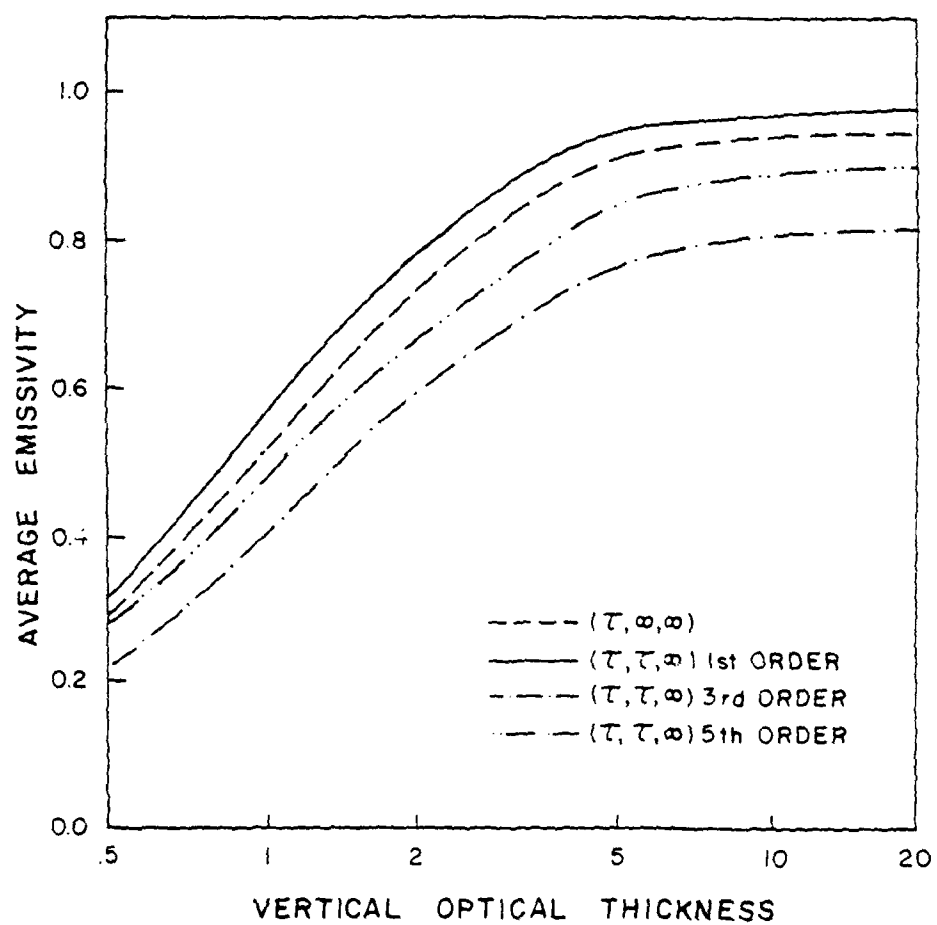
Figure 26. Average emissivity versus vertical optical thickness at 50.50 GHz.

order CL solution is less than the plane-parallel solution, lending more credence to the conjecture that the more finite a cloud model is, the lower its emissivity will be.

CHAPTER 7

ANALYSIS OF DMSP SSM/T DATA

7.1 Cases Selected for Study

We have selected two days, 30 October, 1979 and 23 November, 1979 during which significant cloud and precipitation events are present and during which complete data sets were available over the continental United States. The data included synoptic reports and charts, radar summaries, radiosonde observations, DMSP infrared satellite pictures and SSM/T microwave sounder data. The SSM/T instrument is on board a sun-synchronous polar orbiting satellite.

The cases selected are presented in Table 6 and the satellite pass times presented in Table 6 are the actual observation times of the SSM/T instrument. Note, that, with one exception, the scan times are between 0000 Zulu and 0600 Zulu on the respective dates. Therefore the 0000 Zulu radiosonde observations were deemed most representative and thus were used in the following studies. The DMSP infrared satellite pictures for 30 October 79 are from the same spacecraft as the SSM/T data and therefore are sensed at the same time. The infrared pictures for the 23 November 79 case study have descending node crossing times of 0043 Zulu for the eastern picture and 0224 Zulu for the western picture. Figures 27 , 28 and 29 present the satellite pictures used in the case studies. A major

Table 6. Selected Cases

Station Name	Satellite Pass Time	Latitude (°N)	Longitude (°W)	Case Type
Jackson Mississippi (MS)	0346 Z 30 Oct 79	32.19	90.05	Clear
Centerville Alabama (AL)	0346 Z 30 Oct 79	32.54	87.15	Clear
Little Rock Arkansas (AR)	0346 Z 30 Oct 79	34.44	92.14	Clear
Monett Missouri (MO)	0347 Z 30 Oct 79	36.53	93.54	Clear
Salem Illinois (IL)	0347 Z 30 Oct 79	38.39	38.58	Clear
Peoria Illinois (IL)	0348 Z 30 Oct 79	40.40	89.41	Clear
Boise Idaho (ID)	0530 Z 30 Oct 79	43.34	116.13	Clear
Desert Rock Nevada (NV)	0529 Z 30 Oct 79	36.6	116.1	Clear
Greensboro North Carolina (NC)	0251 Z 23 Nov 79	36.03	79.57	Clear
Chihuahua Mexico (MEX)	0430 Z 23 Nov 79	28.42	106.04	Clear
Del Rio Texas (TX)	0430 Z 23 Nov 79	29.22	100.55	Clear
Dodge City Kansas (KS)	0432 Z 23 Nov 79	37.46	99.58	Clear
Great Falls Montana (MT)	0435 Z 23 Nov 79	47.29	111.22	Clear
Glasgow Montana (MT)	0435 Z 23 Nov 79	48.13	106.37	Clear
Bismark North Dakota (ND)	0350 Z 30 Oct 79	46.46	100.45	Cloudy
Salem Oregon (OR)	0531 Z 30 Oct 79	44.55	123.01	Cloudy
Medford Oregon (OR)	0531 Z 30 Oct 79	42.22	122.52	Cloudy
Huntington W. Virginia (WV)	0252 Z 23 Nov 79	38.22	82.33	Cloudy

Table 6. Selected Cases (Continued)

Station Name	Satellite Pass Time	Latitude (°N)	Longitude (°W)	Case Type
Green Bay Wisconsin (WI)	0253 Z 23 Nov 79	44.29	88.08	Cloudy
Monterrey Mexico (MEX)	0429 Z 23 Nov 79	25.52	100.12	Cloudy
Victoria Texas (TX)	0429 Z 23 Nov 79	28.51	96.55	Cloudy
Rapid City S. Dakota (SD)	0434 Z 23 Nov 79	44.03	103.04	Cloudy
Medford Oregon (OR)	0614 Z 23 Nov 79	42.44	122.52	Cloudy
Dodge City Kansas (KS)	0348 Z 30 Oct 79	37.46	99.58	Precipitating
Omaha Nebraska (NE)	0349 Z 30 Oct 79	41.22	96.01	Precipitating
Huron S. Dakota (SD)	0350 Z 30 Oct 79	44.23	98.13	Precipitating
Dayton Ohio (OH)	0252 Z 23 Nov 79	39.52	84.07	Precipitating
Pittsburgh Pennsylvania (PA)	0252 Z 23 Nov 79	40.32	80.14	Precipitating
Buffalo New York (NY)	0252 Z 23 Nov 79	42.56	78.44	Precipitating
Spokane Washington	0435 Z 23 Nov 79	47.38	117.32	Precipitating
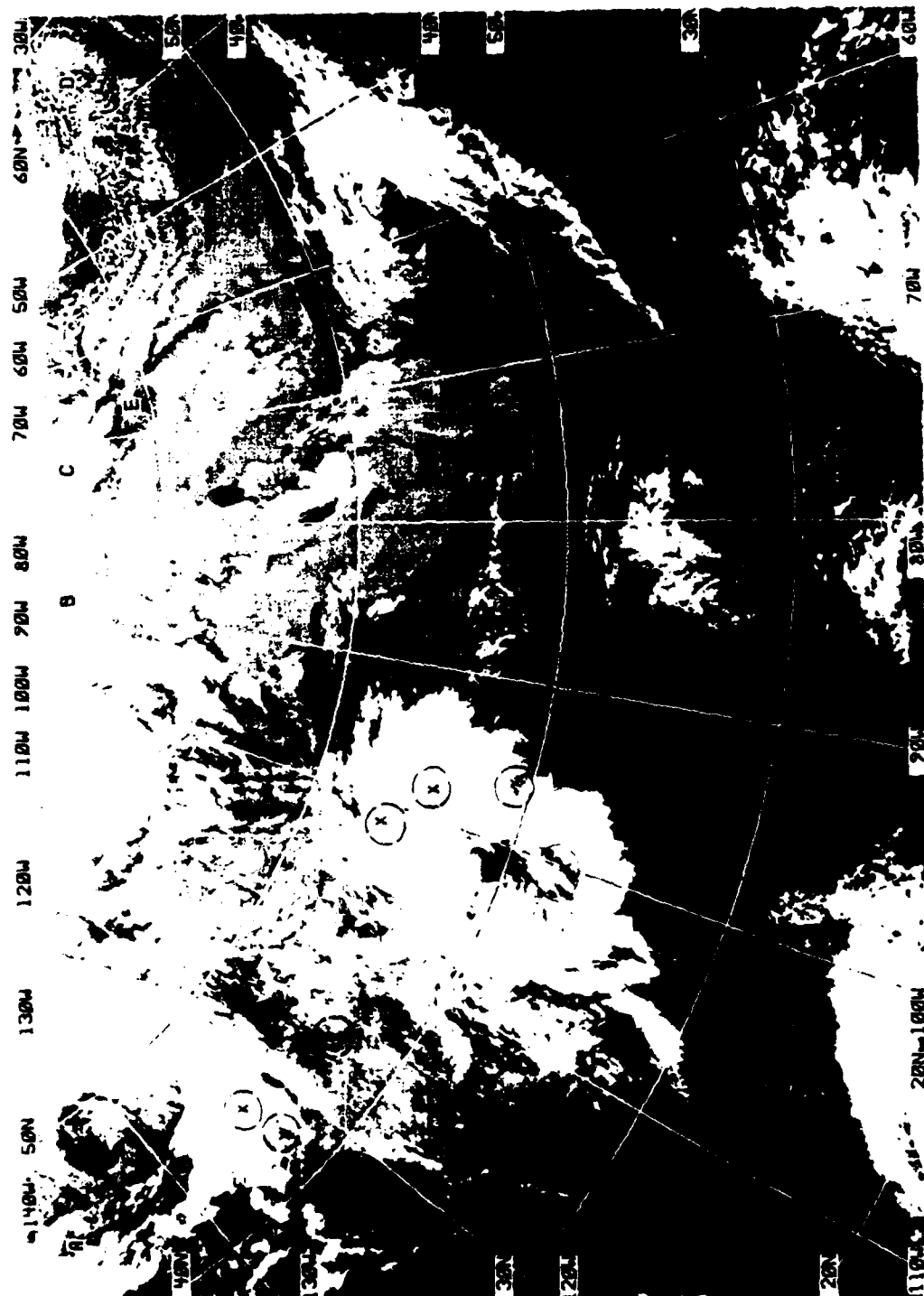
Figure 27.   30 Oct 79 DMSP satellite picture mosaic
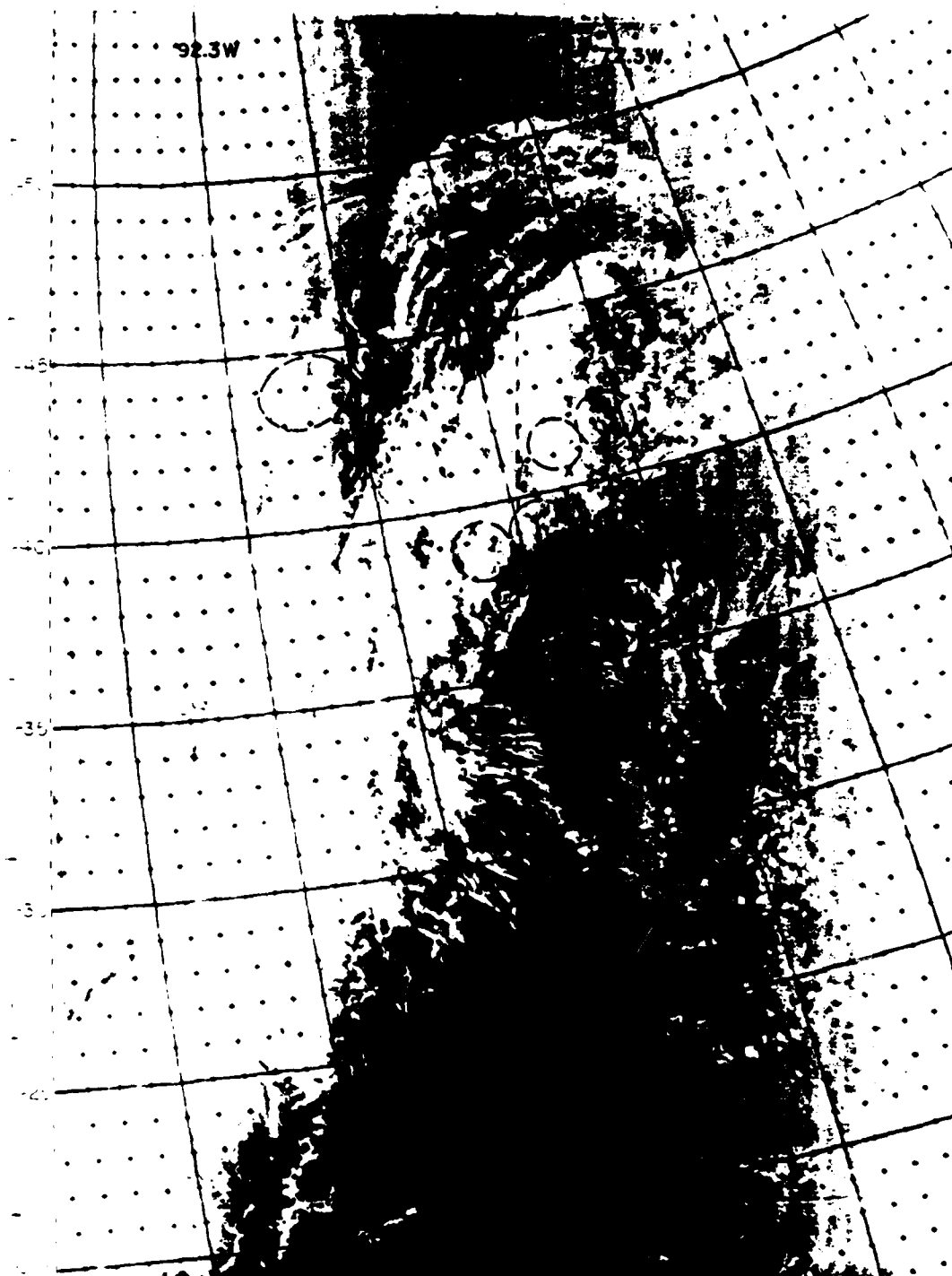
Figure 28. 23 Nov 79 DMSP satellite - eastern scan.
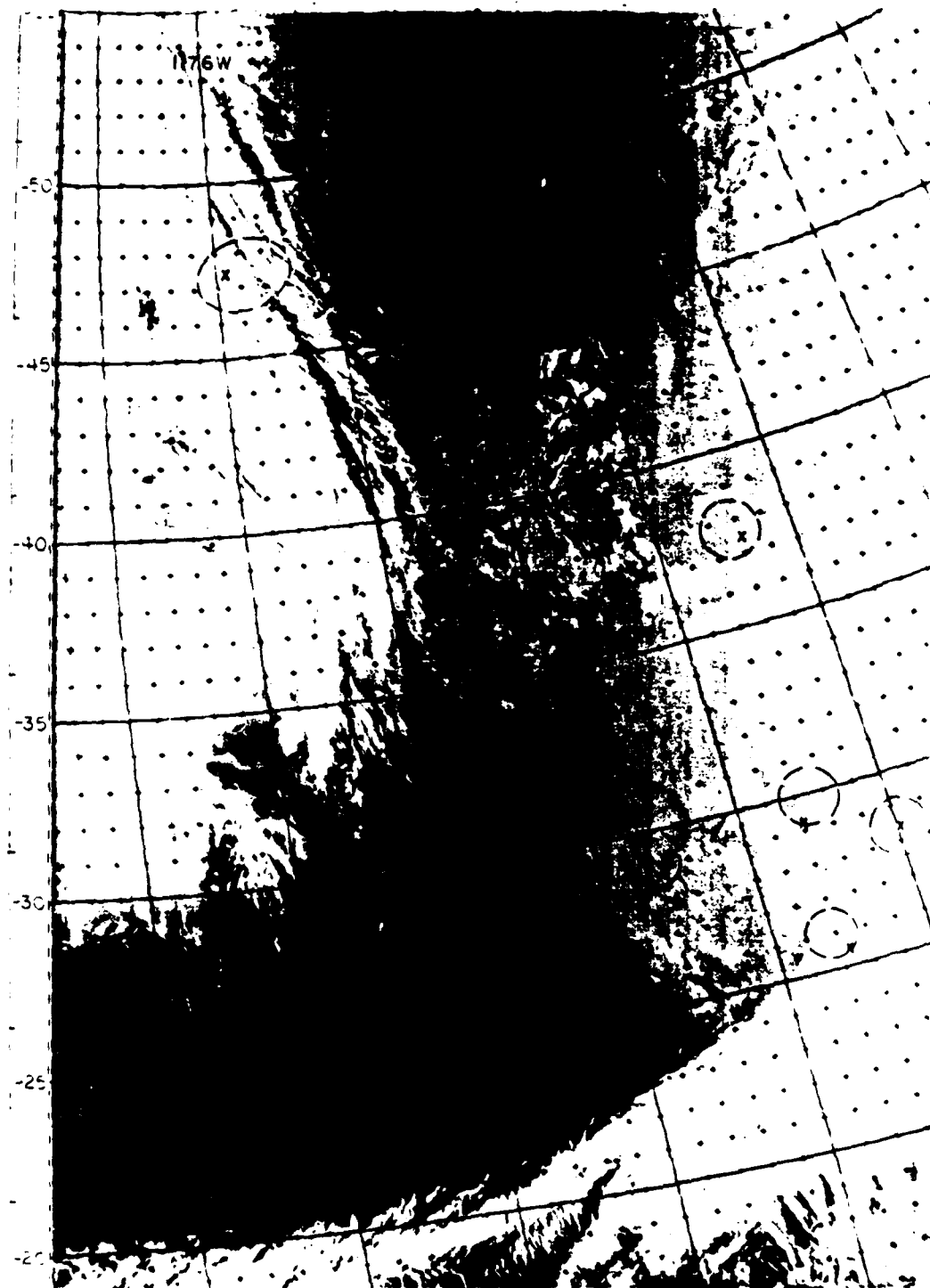
Figure 29.   23 Nov 79 DMSP satellite picture - western scan.

criterion for case selection was to have a radiosonde station within the microwave sounder field of view. The satellite pictures have been superimposed with the SSM/T sounder "footprints" and the relative location of the radiosonde stations within them.

7.1.1 Brief Synoptic Discussion - 30 October, 1979

A surface low pressure center (Fig. 30) lies off the east coast of the United States near 44°N. 62°W. A cold front extends southward and then west to southern North Carolina, becoming a warm front in northern Georgia to southern Arkansas and into Oklahoma. A dissipating low aloft is portrayed on the 30/0000 Zulu 500 mb chart (Fig. 31) as a weakness through the Ohio valley.

The dominant feature on the 500 mb map is a storm system that is deepening and moving into northeast Arizona. A surface low pressure center is drawn in southeast New Mexico. Extending northward from this surface low is an inverted trough extending north-northeast to central Minnesota. The 500 mb chart also shows this trough which extends to a low center near 64°N, 107°W. Cloud patterns associated with the southern storm are extensive (Fig. 27) and case studies were chosen in and around this system. Note that the satellite footprints and selected station locations are presented on the satellite picture (Fig. 27). The details of each individual case will be presented in Section 7.2. A trough at 500 mb just off the west coast of the U.S. supports a surface low drawn near 49°N, 136°W. An occlusion extends south-southeast to a triple point near 43°N, 134°W. This system is moving rapidly and precipitation begins at stations on the Washington
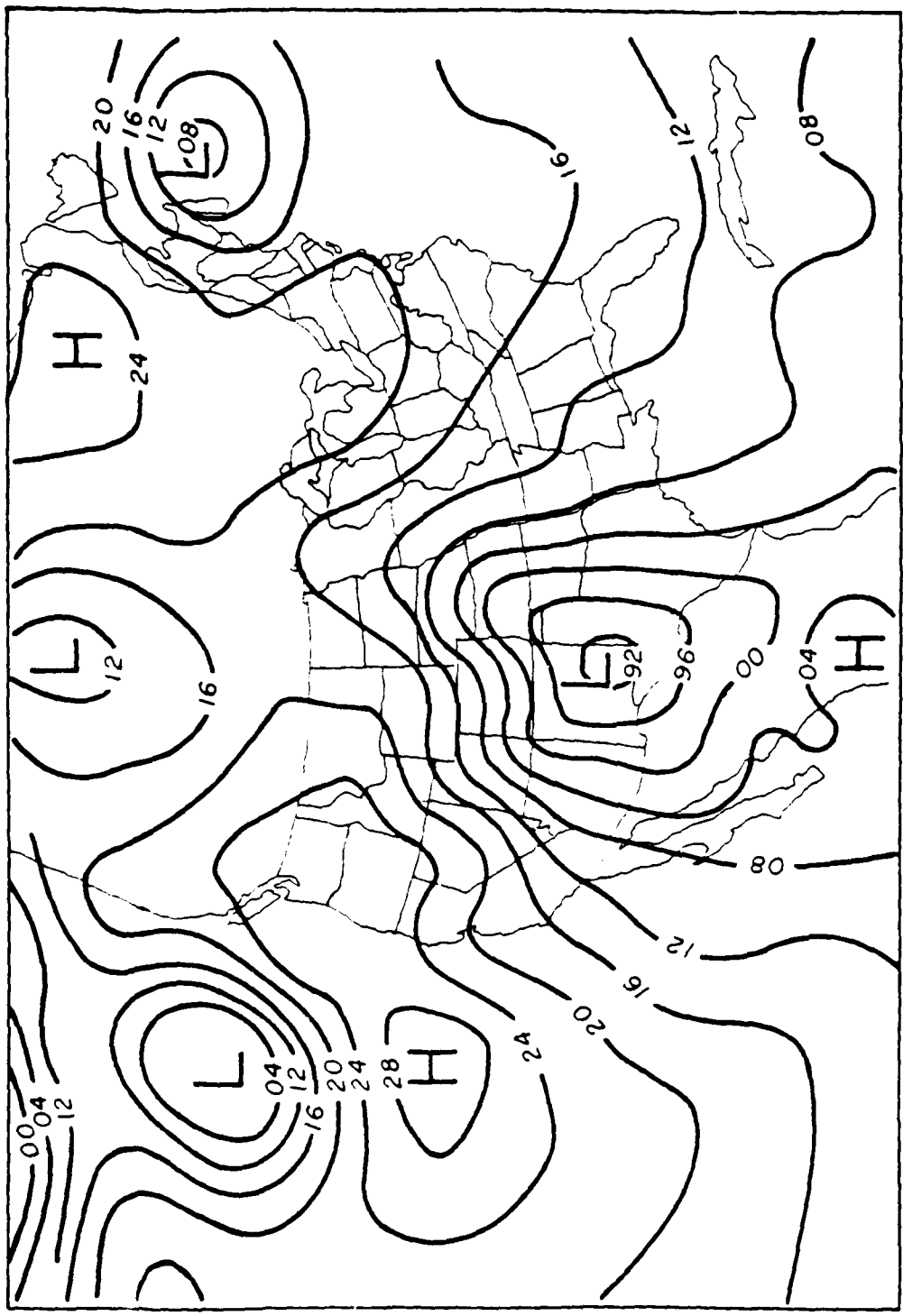
Figure 30. 30 Oct 79, 0000Z, surface analysis.
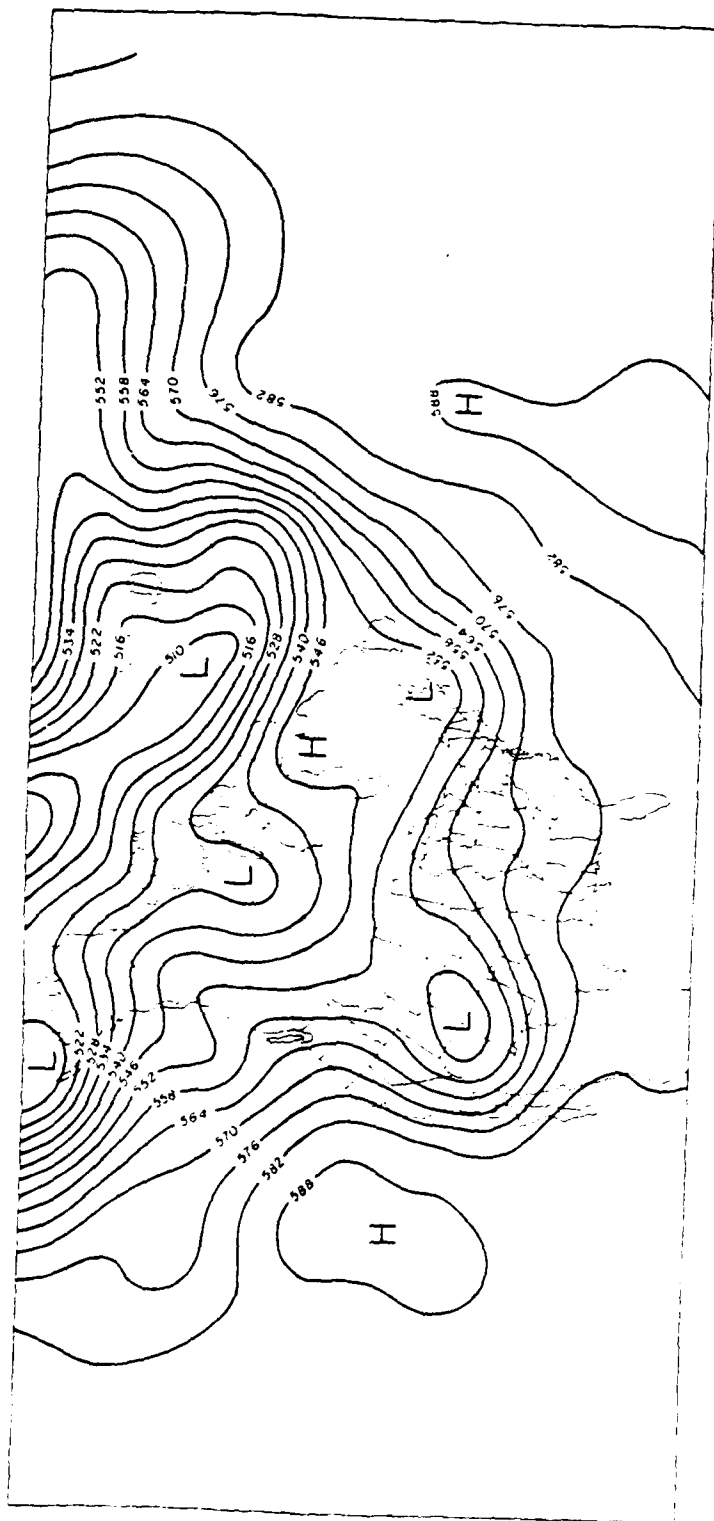
Figure 31, 30 Oct 79, 0000Z, 500 mb analysis.

and Oregon coasts ny 0600 Zulu. The cloud pattern associated with
this system appears to be well organized with the cirrus shield
already on shore at the satellite pass time (Fig. 27).

7.1.2 Brief Synoptic Discussion - 23 November, 1979

A dominant 500 mb low pressure center (Fig. 32) is located in
central Minnesota at 23/0000 Zulu. A deep 500 mb trough extends south-
southwest to the Texas panhandle and continues southwest into northwest
Mexico. On the surface (Fig. 33) there is a double low system with
one low center in south central Minnesota with an occluded front to a
second low drawn on the triple point in central lower Michigan. A
warm front continues eastward to extreme southern Maine. A cold front
extends south through Indiana and into the Gulf of Mexico near New
Orleans, Louisiana. Considerable cloudiness accompanies this storm
system (Fig. 28), extending from the Canadian border across Mexico and
into the eastern Pacific. Another system is just off the west coast
of the U.S. at 500 mb (Fig. 32). The surface map (Fig. 33) shows a
cold front just on the west coast from northern California through
western Oregon and Washington. Extensive cloudiness also accompanies
this storm (Fig. 29) with cloud bands extending along the west coast of
the U.S.

7.2 Comparison of Computed and Observed
    Brightness Temperature

The case studies were divided into two groups - clear and cloudy/
precipitating. The clear atmosphere upwelling brightness temperatures
were computed by the plane-parallel method. The cloudy/precipitating
cases were analyzed using the plane-parallel and cylindrical models.
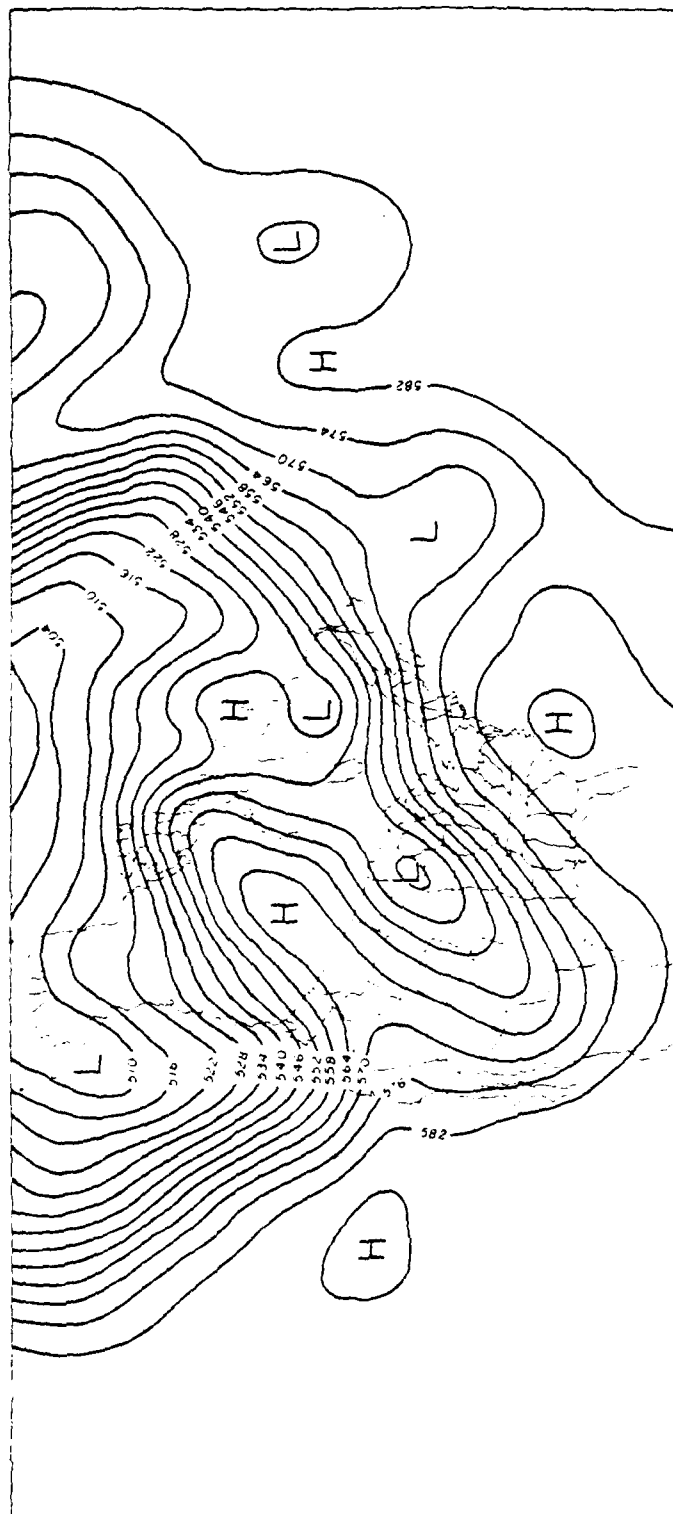
Figure 32. Nov 79, 0000Z, 500 mb analysis.
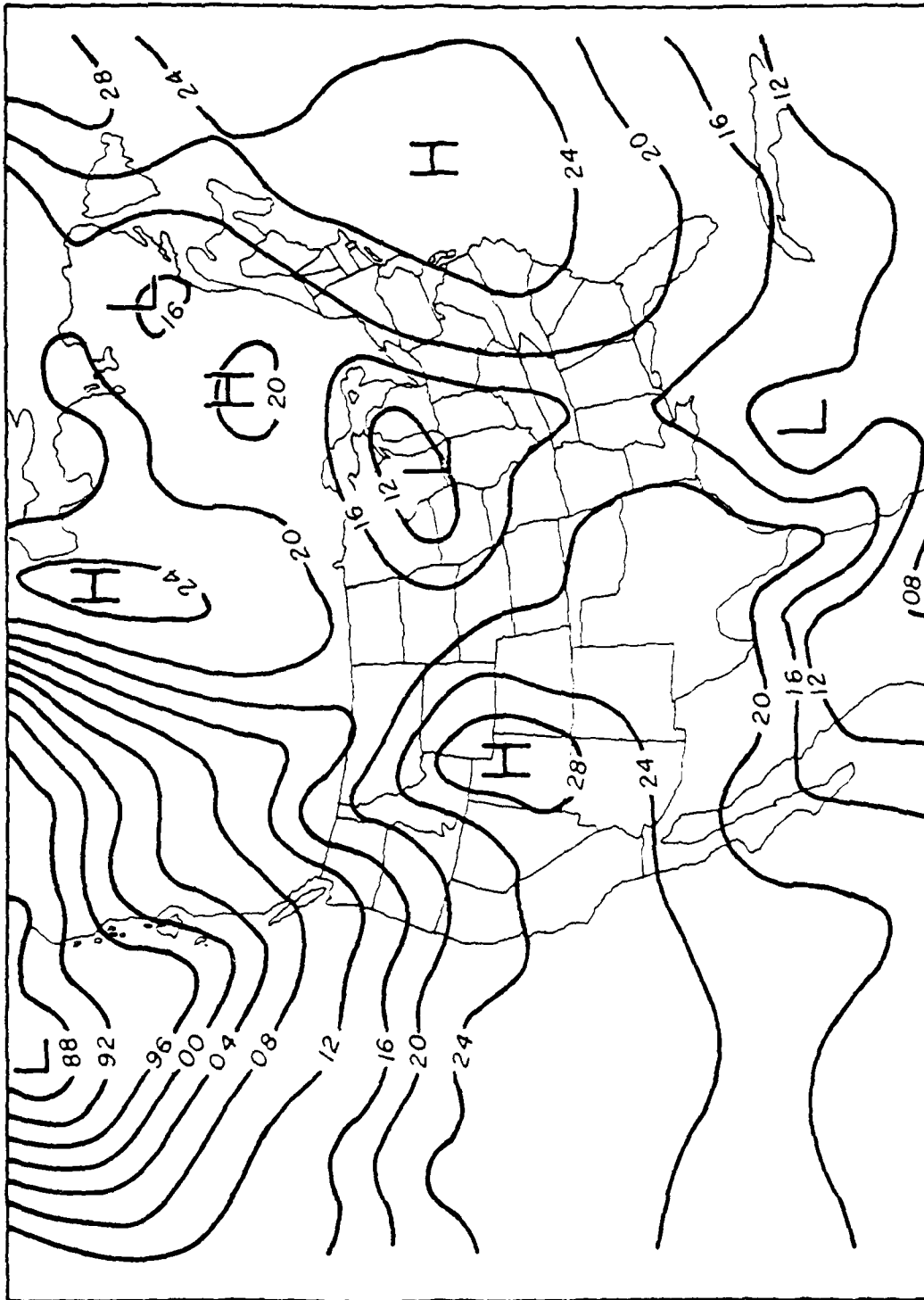
Figure 33.   23 Nov 79, 0000Z, surface analysis.

All results attributed to the cylinder model in the following sections are fifth order solutions.

7.2.1 Clear Atmosphere Cases

A major problem in microwave remote sensing over land is determining the surface emissivity. Gloersen, et. al. (1972) have presented microwave emissivity values ranging from approximately .80 over wet bare soil to .98 over a uniformly vegetated surface. This background variability coupled with atmospheric uncertainties (e.g., clouds and precipitation) considerably complicate the remote sensing effort. In the clear (non-scattering) atmosphere the radiative transfer problem is somewhat simplified and the surface emissivity may be estimated by an objective scheme. Two such schemes were investigated for use in the clear atmosphere.

The first method involoves solving the radiative transfer equation for the surface emissivity using the window frequency of 50.50 GHz. This frequency's weighting function peaks at or near the surface and we may construe that the bulk of the energy received by an observer at the top of the atmosphere at this frequency had its origin at the surface. This basic equation may be written as

$$T_B(\nu_1) = \varepsilon_{\nu_1} T_s T_{\nu_1}(0,\infty) + \int_{z=0}^{\infty} T(z) \, dT_{\nu_1}(z,\infty)$$

$$+ (1-\varepsilon_{\nu_1}) T_{\nu_1}(0,\infty) \int_{z=\infty}^{0} T(z) \, dT_{\nu_1}(0,z), \tag{7.1}$$

where T_B is the brightness temperature at $\nu_1(50.50 \text{ GHz})$, ε is the emissivity, T_s is the surface temperature, T_{ν_1} is the 50.50 GHz

transmission function, and $T(z)$ os the temperature at height z. For simplicity we may define the following terms:

$$A_1 = T\nu_1(0,\infty)$$

$$B_1 = \int_{z=0}^{\infty} T(z) \, dT_{\nu_1}(z,\infty)$$

$$C_1 = \int_{z=\infty}^{0} T(z) \, dT_{\nu_1}(0,z) \tag{7.2}$$

Substituting Eq. (7.2) into Eq. (7.1) and solving for ε, the equation may be written

$$\varepsilon_{\nu_1} = \frac{T_B(\nu_1) - B_1 - A_1 C_1}{T_s A_1 - A_1 C_1} \tag{7.3}$$

For the clear column case studies, the atmosphere radiosonde profiles may be used to generate the transmission function, the surface temperature averaged over the satellite "footprint" may be estimated from the synoptic reports, and the observed values of brightness temperature may be used for $T_B(\nu_1)$. Note Eq. (7.3) may be solved for the 50.50 GHz surface emissivity. It has been generally found that the emissivity does not change in value between 50.50 and 59.40 GHz (Gloersen, et. al., 1972). Thus, the 50.50 GHz value may be employed in upwelling brightness temperature calculations for the remaining channels. Since Eq. (7.1) is applicable to all frequencies, we may replace ν (50.50 GHz) in Eq. (7.1) by ν_2(53.20 GHz), the wing channel whose weighting function peak was nearest the surface. The equation for 50.50 GHz was then divided by that of 53.20 GHz to give

$$\frac{\varepsilon_1 T_s A_1 = T_{B_1} - B_1 - A_1 C_1 + \varepsilon_1 A_1 C_1}{\varepsilon_2 T_s A_2 = T_{B_2} - B_2 - A_2 C_2 + \varepsilon_2 A_2 C_2} , \qquad (7.4)$$

where the subscript 1 refers to 50.50 GHz and 2 refers to 53.20 GHz. Once again the surface emissivity is assumed invariant for the frequency range considered and Eq. (7.4) may be solved for the surface emissivity independent of the surface temperature as

$$\varepsilon = \frac{T_{B_1} - B_1 - A_1 C_1 - (\frac{A_1}{A_2})(T_{B_2} - B_2 - A_2 C_2)}{A_1 C_2 - C_1} . \qquad (7.5)$$

This emissivity value may now be used to solve Eq. (7.1) for the surface temperature. Surface temperature and emissivity values generated by methods one and two are presented in Table 7. The emissivities calculated by method 1 seem to be more in accordance with published values (Gloersen, et. al., 1972) for the different types of ground surfaces than those of method 2. Therefore, the emissivities of method 1 were used for the clear column calculations of the remaining SSM/T frequencies. These calculations are presented in Fig. 34. Note that a 50.50 GHz diagram is not presented since the calculated and observed values will match exactly for this frequency when using method 1. At 53.20 GHz there is generally good agreement between the calculated and observed brightness temperatures, with most of the calculations slightly underestimating the observed values. 53.45 GHz and 54.90 GHz channels overestimate the observations - 54.90 GHz by a larger amount in the average than 54.35 GHz. Referring to Fig. 3,

Table 7. Generated Emissivities and Surface Temperatures

Station	Method 1		Method 2	
	ϵ	$T_s(°K)$	ϵ	$T_s(°K)$
Jackson, MS	.954	289.8	.890	303.4
Centreville, AL	.949	289.8	.895	301.1
Little Rock, AK	.958	287.1	.901	299.4
Monett, MO	.971	287.1	.902	301.9
Salem, IL	.969	282.1	.873	302.5
Peoria, IL	.940	285.9	.894	295.9
Dodge City, KS	.933	273.2	.896	281.3
Del Rio, TX	.924	284.6	.905	288.9
Great Falls, MT	.908	275.9	.933	270.6
Glasgow, MT	.902	281.4	.927	275.7
Greensboro, NC	.935	290.9	.873	305.2
Chihuahua, MEX	.912	280.6	.948	272.4
Desert Rock, NV	.900	281.5	.814	307.5
Boise, ID	.906	273.2	.921	270.2
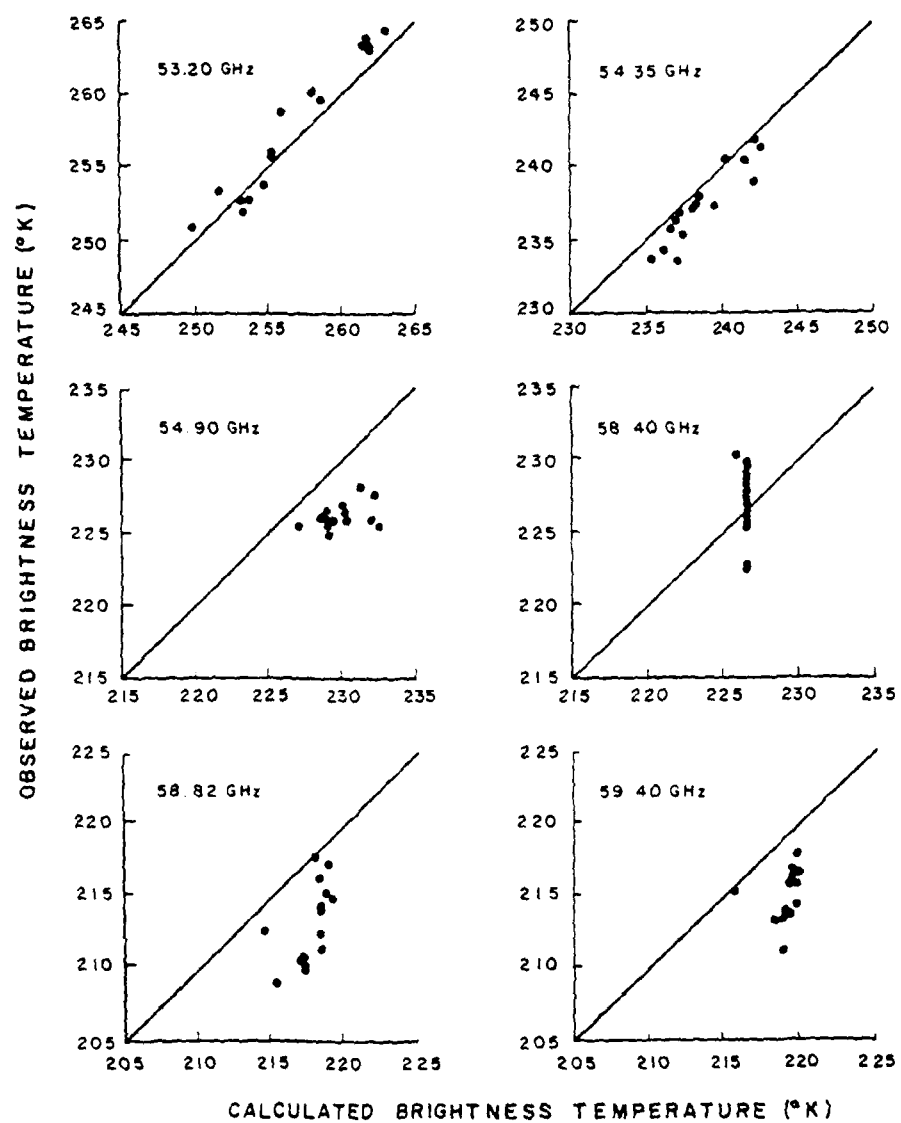
Figure 34. Calculated versus observed clear column brightness temperatures.

the weighting function diagram, it is seen that all three of these frequencies' weighting functions peak well below 16 km. The temperature profile is known to be at least 16 km in all of the clear cases. In theory, then, the calculated values should match the observations to within the accuracy of the radiosonde observation.

The brightness temperature at 53.20 GHz frequency is significantly affected by the surface. Since the height of the standard meteorological instrument shelter is 6 feet, tnis should cause the actual surface temperature to be underestimated. This fact may provide a possible answer for 53.20 GHz calculation generally being lower than the observed values.

The brightness temperatures at 54.35 GHz and 54.90 GHz are not appreciably affected by the surface, since the transmission from the Earth's surface to the top of the atmosphere is approximately .023 and .003 respectively. Since the temperature profile is known to a reasonable accuracy at these heights, it would appear, based on the studies, that there may be some systematic error involved in calculating the brightness temperature. This systematic overestimation in remote sensing channels has been noted by Liou and Yeh (personal communication) in the infrared region. Since the transmission functions are calculated in a different manner for the infrared region than in the microwave region, and the error is still apparent, it seems that the possibility of faulty transmission functions is reduced. A more likely reason may be that the source function for the clear column radiation calculations is somehow being systematically

overestimated. This conjecture was first mentioned by McClatchey
et. al. (1976).

Radiosonde observations were not available above 16 km for the
clear column case studies with the exception of Chihuahua, Mexico on
23 November 1979, where the observation was 24 km. Where the ob-
servation was not available, the Spring/Fall climatological profile
was substituted. Referring to Fig. 3, it is seen that the weighting
functions of frequencies of 58.82 GHz, 59.40 GHz and 58.40 GHz peak
above 16 km. The 58.82 GHz weighting function peaks highest in the
atmosphere with only negligible energy emerging from the top of the
atmosphere originating below 18 km. As a result, the calculated values
were nearly the same for all of the cases since they were all based on
the same climatological sounding. 58.82 GHz and 59.40 GHz weighting
functions peak lower in the atmosphere, at 17 and 20 km, respectively,
and should be influenced somewhat by the available soundings. It is
evident that the plots are approaching the results portrayed for
58.40 GHz as the peak of the weighting function rises higher in the
atmosphere (e.g., the calculated values are more and more representa-
tive of the climatological sounding). The exception to this is the
value presented for Chihuahua, Mexico, whose sounding was available to
25 km. The results for this sounding are underlined (Fig. 34) on the
plot for 58.82 GHz and 59.40 GHz and also demonstrates that the calcu-
lated value is larger than the observed brightness temperature, repeat-
ing the trend established by the comparisons at 54.35 and 54.90 GHz.

7.2.2 Cloudy/Precipitating Cases

As stated in Chapter 3, the Marshall-Palmer drop size distribution was used to simulate precipitating clouds. Non-precipitating clouds were modeled using a drop size distribution established by experimentation and presented by Mason (1971), as measured by Diem (1948) for cumuliform clouds.

Figure 35 presents how the cylinder model may be applied to the atmosphere within the satellite field of view. This sort of configuration suggests a cold frontal band or squall line in the real atmosphere. The SSM/T instrument chosen for case study investigations has a footprint on the Earth's surface that ranges from a near circle of radius of 87 km at nadir to an ellipse with a semi-major axis of 152 km at maximum scan angle (see Fig. 2).

In order to realistically evaluate the upwelling brightness temperature in cloudy atmospheres within the SSM/T field of view, modification of the cylinder model is required so that cloud and/or precipitation could be placed below the tropopause. The cylinder was placed so that a portion of it was below the surface. The portion remaining above the surface was dictated by the height of the cloud top and the areal extent of the cloud formation. For outer boundary conditions, incoming intensity streams on the portion of the cylinder beneath the surface were chosen to be εT_s. Since the size of the cylinder will be increased, the amount of scattering material in the cylinder will also be increased. This, in effect, would cause an unrealistically large optical depth, due to scattering, in the portion of the cylinder that represented the cloud. For this reason, adjust-
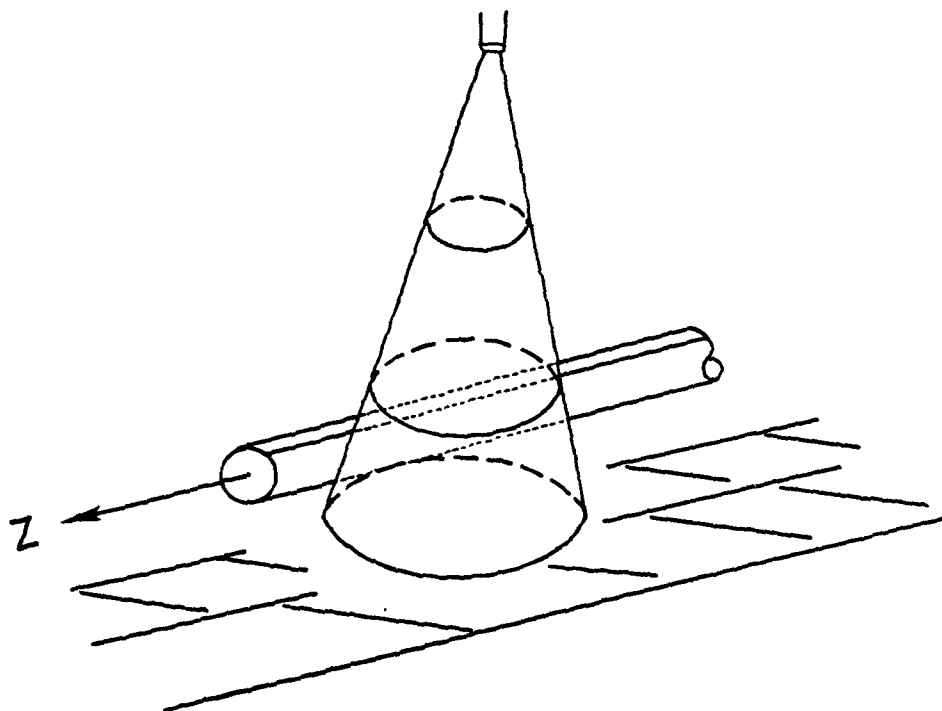
Figure 35. Hypothetical cylinder model placement in the satellite field of view.

ment was made such that the optical depth due to scattering was re-
duced by the ratio of the area of the cylinder cross section repre-
senting the cloud to the total cross sectional area. In practice,
this ratio was multiplied by the scattering coefficient. The cloud
temperature was chosen as the midpoint value along the radius vector
at nadir-zenith. Finally, since only a portion of the field of view
may be covered by the cloud, the cylinder cloud solution is averaged
with a clear column solution based on the temperature profile at the
radiosonde station in the field of view. The solutions are weighted
according to the precentages of the field of view covered by cloud.

Precipitating and cloudy cases are presented individually. Be-
cause the methods used for deriving surface emissivity in the clear
atmosphere could not be applied in these cases, the was fixed at
.97, a compromise value based on published literature (Gloersen, et.
al., 1972). Note that the precipitating cases are in areas that are
heavily vegetated, and as a result, the surface emissivity should not
degrade significantly during precipitation. Estimations of the thick-
ness and cloud amount within the field of view were made using the
available radiosonde data and DMSP infrared satellite photographs.
The plane parallel cloud used for comparison with the cylinder cloud
was composed of three isothermal layers. Because of the plane parallel
model's geometry, the plane parallel cloud filled the entire field of
view.

The information gathered for input to the cloudy cases is pre-
sented as follows:

1. Bismark, N.D. - 30 Oct 79. The satellite picture indicates a

cirrus shield over low cloudiness. Radar charts show no precipitation
in the field of view. Station reports and the National Weather Service
nephanalysis show low cloudiness within the field of view covering an
estimated 60% of the scan area with cloud bases at .9 Km and tops at
2.75 Km. All bases and tops given are above ground level values. The
scan angle is 24°.

2. Medford, OR. - 30 Oct 79. Satellite picture indicates cloudi-
ness in the northwest portion of the scan spot. Synoptic data indicate
this is a band of alto-cumulus with bases at 4.5 Km and top at 6.0 Km.
Cloud coverage is estimated 30% and the scan angle is 12°.

3. Salem, OR. - 30 Oct 79. Satellite picture shows overcast cirrus.
Synoptic reports and nephanalysis indicate a layer of alto-stratus below
the cirrus between 3.5 and 4.5 Km. The alto-stratus is estimated to
fill 40% of the field of view. The scan angle is 12°.

4. Rapid City, S.D. - 23 Nov 79. Satellite picture shows an area
pf alto-cumulus with little or no organization. Synoptic reports tend
to confirm this. Bases were estimated at 2 Km and tops at 3 Km. Cloud
coverage was assumed to be 50%. The scan angle is 12°.

5. Huntington, W.V. - 23 Nov 79. Sa ellite picture indicates
cirrus over some low cloudiness. Synoptic reports show the lower cloud-
iness to be cumulus and cumulus congestus. Cloud bases are assumed to
be 1.25 Km amd tops at 4.0 Km with areal coverage set at 30%. The scan
angle is 12°.

6. Green Bay, WI. - 23 Nov 79. A thin cirrus band lies over a
low stratus deck on the backside of the filling surface low center.
Synoptic reports indicate the cloud bases at .1 Km and tops at 1.6 Km.

Coverage is estimated at 90% and the scan angle is 36°.

7. Monterrey, MX - 23 Nov. 79. Satellite picture shows a large cloud band over the station which fills most of the scan spot. Synoptic reports indicate this band is a layer of alto-cumulus with cirrus above. Cloud bases were assumed to be 2 km with tops at 3 km. The scan is at 0° and the area is 80% cloud covered.

8. Victoria, TX - 23 Nov. 79. This is the same cloud band that is over Monterrey, Mexico, but synoptic reports indicate the layer of alto-cumulus is thicker, with bases at 2 km and tops at 4.5 km. The scan angle is 24°. Eighty percent cloud coverage was found.

Scatter diagrams are presented for the cloudy cases in Figures 36 and 37. Note that both models give brightness temperature values that are in the same range. Also, calculations from both models consistently give values larger than the observations, repeating the trend denoted in the clear column study.

The precipitating cases are presented as follows:

1. Dodge City, KS - 30 Oct. 79. Satellite picture indicates a good squall line in the field of view. Since the scan angle is 36°, the sensor may have picked up some signature from the leading cloud band on the eastern edge of the satellite footprint. The radiosonde station appears to be in the clear at the scan time and was definitely in the clear at radiosonde time. The cloud band thickness was estimated to be from the surface to 12 km and covered 30% of the scan area. Rainfall rate was estimated at 5 mm/hr.

2. Omaha, NE - 30 Oct. 79. The satellite picture indicates cloudiness to the northwest and southwest of Omaha. This situation
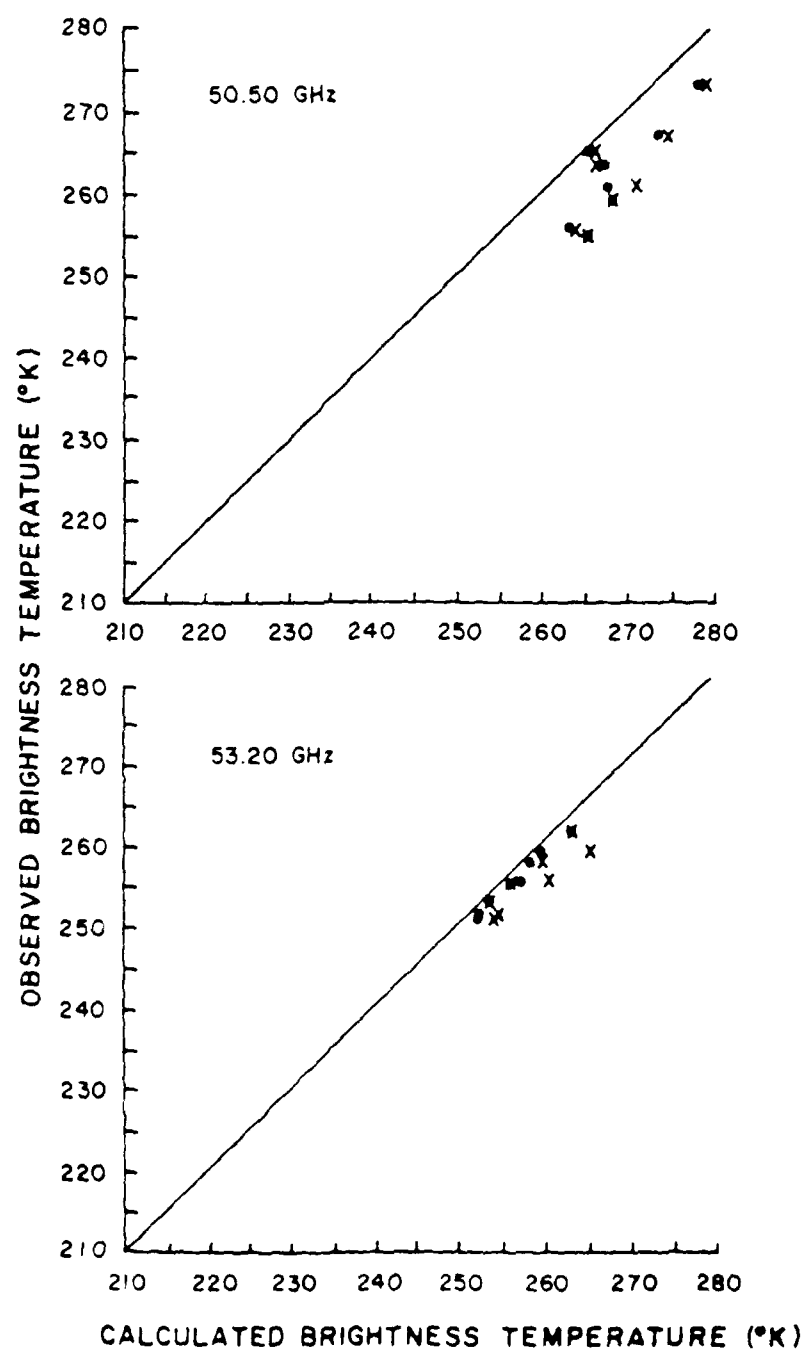
Figure 36. 50. 50 and 53.20 GHz calculated versus observed cloudy brightness temperatures.
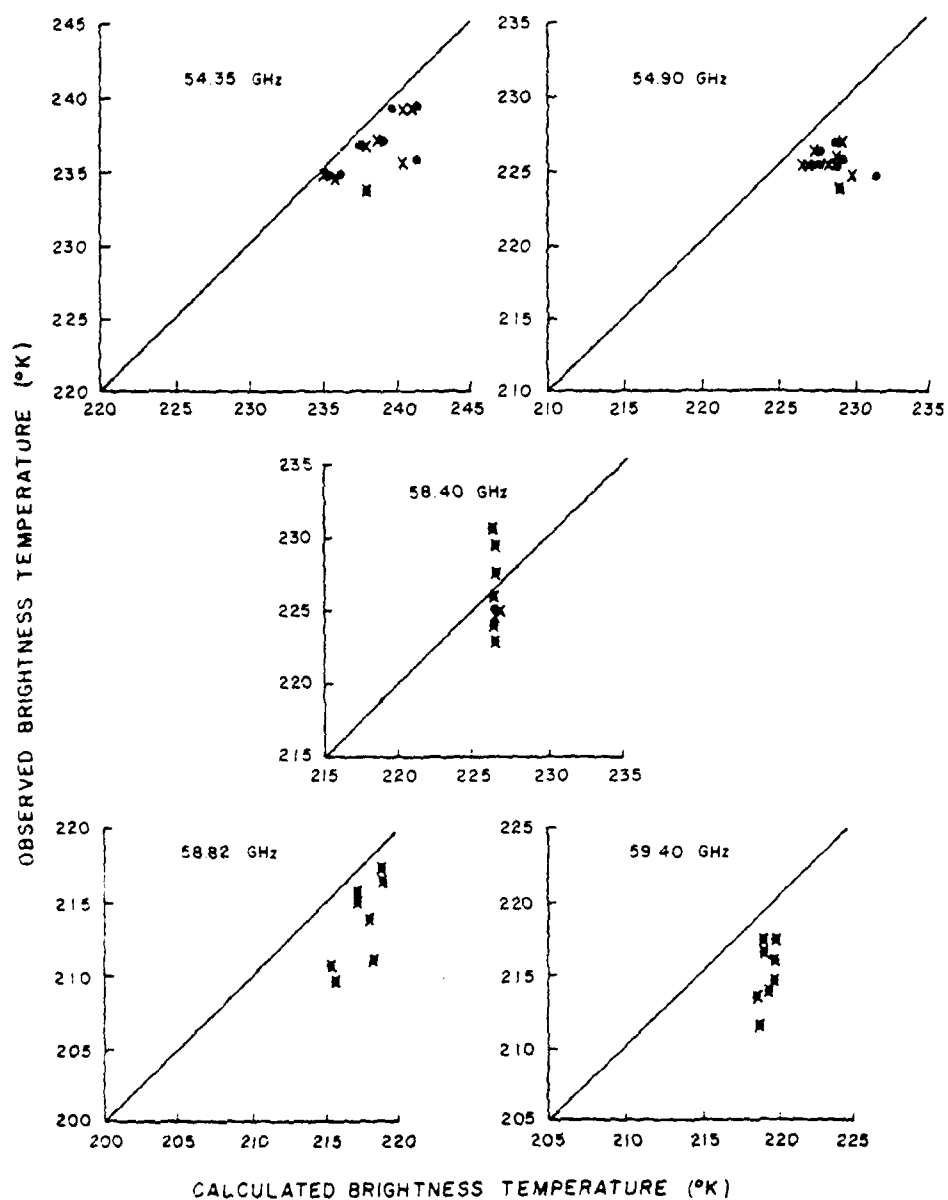
Figure 37. 54.35, 54.90, 58.40, 58.82 and 59.40 GHz calculated versus observed cloudy case brightness temperature. ε=.97, "•" = plane-parallel, "x" = 5th order cylinder.

was modeled by a cylinder covering 30% of the scan footprint. Cloud base was assumed to be the surface and cloud top was at 8 km. The scan angle was 24° and the rainfall rate was assumed to be 5 mm/hr.

3. Huron, SD - 30 Oct. 79. The satellite picture shows an extensive cloud area in the scan. Radar observations are revealing, showing the eastern portion of the scan to have no precipitation. The area covered by precipitation was assumed to be 70%. Cloud tops and bases were from surface to 5 km. The scan angle was 12° and the rainfall rate estimated to be 1 mm/hr.

4. Spokane, WA - 23 Nov. 79. The satellite picture indicates two cloud bands in the field of view. The leading cloud band, from synoptic reports, is believed to be cirrus with some alto-cumulus below. The trailing cloud band has precipitation. The surface temperature is 34°F and it is snowing at Spokane. The cloud modeled had a base at the surface and the top was assumed to be 5 km. The area covered with precipitating cloud was 50% of the total. Rainfall rate was 1 mm/hr and the scan angle was 36°.

5. Dayton, OH - 23 Nov. 79. The satellite picture shows cloud covering nearly all of the scan. Synoptic data reveals that the eastern portion of the cloudiness may be cirrus only. The raining cloud thickness was assumed to be from the surface to 3.5 km and to cover 60% of the scan. The rainfall rate was 1 mm/hr and the scan angle was 24°.

6. Pittsburgh, PA - 23 Nov. 79. Satellite pictures reveal that clouds completely fill the field of view. Radar reports indicate that the extreme eastern and western edges of the scan may be cirrus only.

Therefore, the raining cloud was assumed to cover 80% of the scan. The cloud base was at the surface and tops were assumed to be at 4.0 km. Rainfall rate was 1 mm/hr and the scan angle was 0°.

7. Buffalo, NY - 23 Nov. 79. Satellite picture shows several showers in the scan but no clear organization. Radar reports confirm this. Raining cloud coverage was assumed to be 40% with cloud tops at 4 km. The scan angle was 12° and the rainfall rate was 1 mm/hr.

Scatter diagrams are presented for the precipitating cases in Figures 38 and 39. The diagrams for 50.50 GHz and 53.20 GHz show some interesting results. Generally the cylinder model predicts brightness temperature values that are slightly higher than observed. The plane-parallel results are all lower than the observed values for these frequencies. In two cases, the plane-parallel results were considerably less than the observed while the cylinder results were quite good. This characteristic continues to the frequency with the next higher weighting function peak, 54.35 GHz. These cases correspond to the only two case studies that had rainfall rates greater than 1 mm/hr. The plane-parallel model failed the worst at Dodge City, KS. The other poor case was Omaha, NE. Both cases had 5 mm/hr rainfall rates. Actual rainfall rates were determined by estimating the average rainfall in a scan from the observed rainfall amounts and then dividing that value by the time the radar echoes remained over the area.

Some additional insight may be gained from these studies. The Spokane, WA case supports an argument put forth by Savage (1976) that snowflakes (as opposed to smaller ice crystals found in cirriform clouds which have negligible effect on these microwave frequencies)
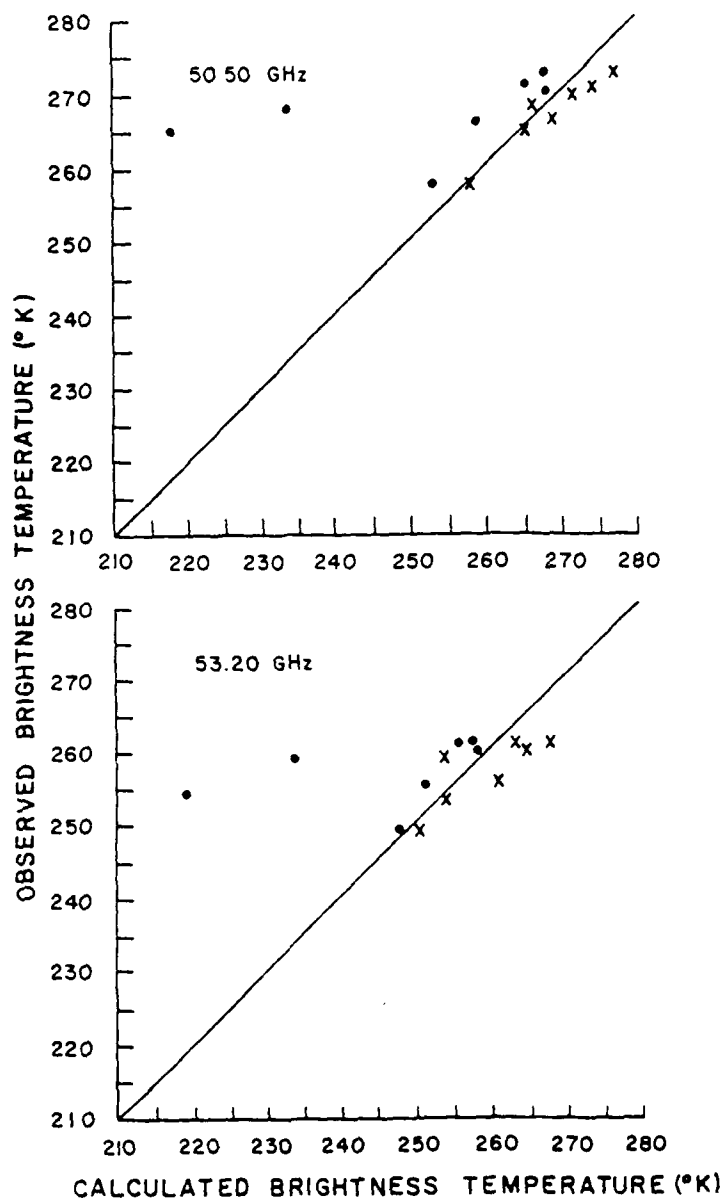
Figure 38. 50.50 and 53.20 GHz calculated versus observed precipi-
            tating case brightness temperatures. ε=.97, "•" =
            plane-parallel, "x" = 5th order cylinder.
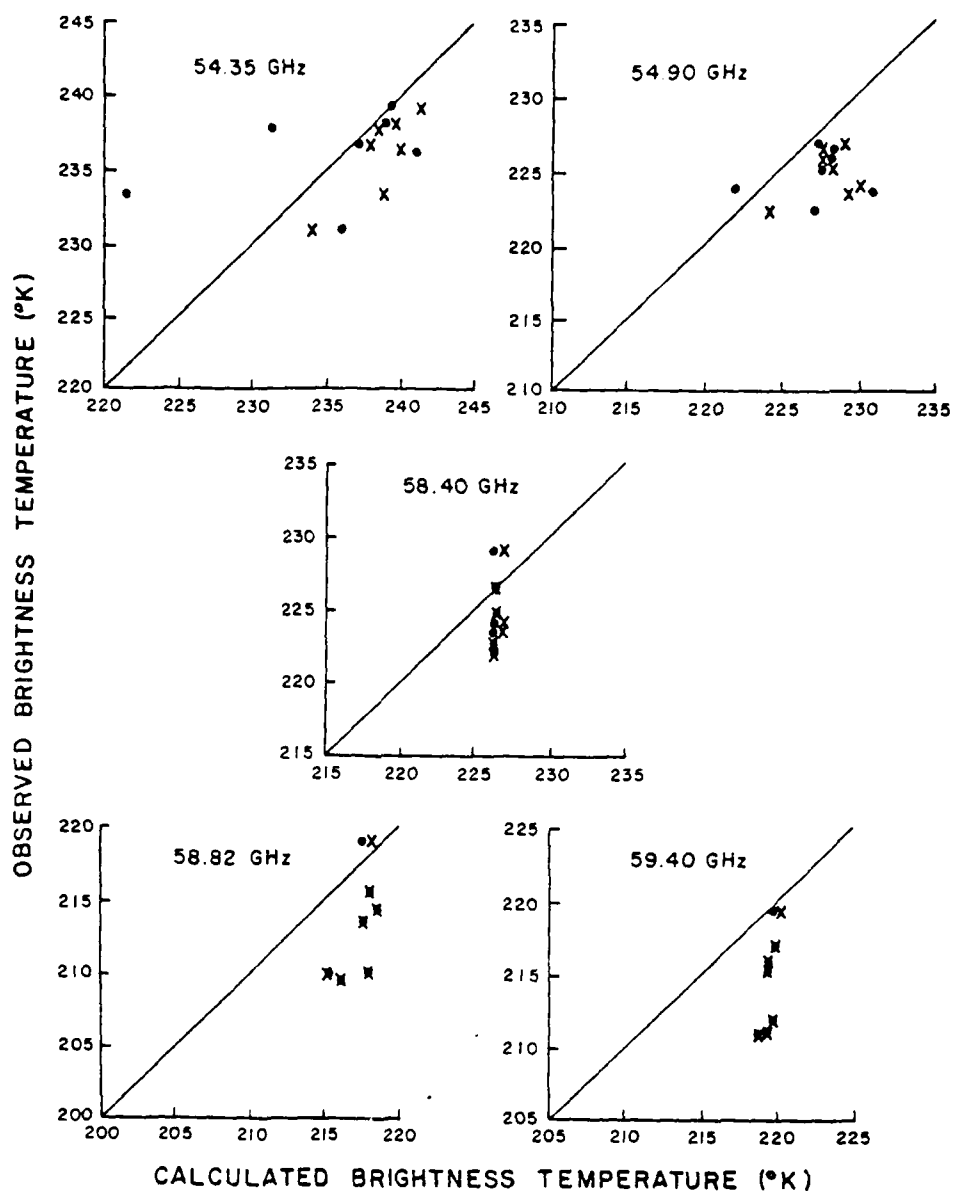
Figure 39. 54.35, 54.90, 58.40, 58.82 and 59.40 GHz calculated versus observed precipitating case brightness temperatures. ε=.97, "·" = plane-parallel, "x" = 5th order cylinder.

have a pronounced effect on microwave radiative transfer. Also, the
question arises as to why the plane-parallel model failed so badly at
the higher rainfall rates. Inspection of the cylinder cloud solution
(not weighted with the clear column for area coverage consideration)
shows values of 243.75 and 252.99° K for Dodge City, KS and Omaha, NE,
respectively, as opposed to the 218.29 and 234.3° K values for the
plane-parallel model. We note that in these two cases, the areal
coverages by precipitation were only 30%. Thus, it seems that a
finite cylindrical model gives a much better approximation than the
plane-parallel model in the computations of the upwelling brightness
temperatures in these cases. Tables 8 and 9 present the numerical
results that are depicted in Figures 36 through 39.

7.3 Temperature Retrieval

The prime objective of the DMSP SSM/T microwave sounders has been
to derive accurate temperature profiles in all weather conditions in
conjunction with numerical weather prediction. In the previous com-
parison program for the computed and observed brightness temperatures,
temperature profiles for selected synoptic cases have been obtained
from the available radiosondes. Thus, it seems interesting and signi-
ficant to examine the accuracy and validity of atmospheric conditions
over land. In this study, we use a statistical method for temperature
recovery intended for operational use by the Air Force Global Weather
Central.

In the statistical approach, it is generally assumed that the de-
rivation of the predicted parameter from the climatological mean may
be expressed as a linear combination of the deviation of the measured

Table 8. Comparisons between observed and calculated
brightness temperatures for precipitation cases.

30 Oct 79		Channels						
		1	2	3	4	5	6	7
72451	OBS	264.81	253.93	233.59	224.04	229.10	214.74	217.15
	CL	265.35	254.47	238.89	230.66	226.89	218.72	219.95
	PP	218.29	219.30	221.40	222.18	226.56	218.73	219.75
72553	OBS	268.02	258.85	238.08	226.97	225.56	213.63	215.38
	CL	266.36	253.89	238.5	229.53	226.72	217.85	219.58
	PP	234.3	234.57	231.57	227.38	226.56	217.85	219.47
72654	OBS	266.12	255.47	236.93	226.7	224.68	215.66	216.16
	CL	268.82	261.67	237.93	228.08	226.75	218.18	219.65
	PP	259.27	251.97	237.39	228.67	226.56	218.15	219.55
23 Nov 79								
72785	OBS	257.55	249.24	230.83	222.77	224.26	219.05	219.49
	CL	258.45	250.81	234.16	224.45	227.15	218.15	220.03
	PP	253.72	248.49	236.17	227.48	226.56	217.87	219.68
72429	OBS	272.26	259.92	236.66	223.75	223.85	209.89	211.86
	CL	276.99	265.14	240.16	229.45	226.99	218.31	219.90
	PP	268.15	258.85	241.39	231.15	226.56	218.29	219.73
72520	OBS	269.30	260.89	239.59	226.19	222.06	210.18	210.91
	CL	271.63	267.88	241.25	228.56	226.56	215.53	218.92
	PP	268.20	258.12	239.46	228.37	226.56	215.53	218.92
72528	OBS	270.62	260.71	238.23	225.80	222.42	209.84	211.26
	CL	274.57	263.38	239.64	228.37	226.65	216.3	219.18
	PP	265.10	256.46	239.30	228.80	226.56	216.22	219.09

Table 9. Comparisons between observed and calculated
brightness temperatures for cloudy cases.

30 Oct 79		1	2	3	Channels 4	5	6	7
	OBS	264.79	253.32	234.78	225.75	224.99	216.94	217.19
72764	CL	266.38	254.0	235.29	227.26	226.88	218.89	219.91
	PP	265.92	253.33	236.37	228.20	226.56	218.89	219.75
	OBS	262.78	255.31	237.11	225.69	227.39	214.89	216.6
72597	CL	266.84	256.51	238.68	228.75	226.64	217.41	219.47
	PP	266.99	256.35	238.96	229.18	226.56	217.37	219.42
	OBS	260.65	255.32	236.84	225.68	225.95	215.47	217.13
72694	CL	270.94	260.93	237.79	227.34	226.67	217.48	219.60
	PP	267.69	255.41	237.77	227.95	226.56	217.42	219.53

23 Nov 79

		1	2	3	Channels 4	5	6	7
	OBS	255.58	251.59	234.78	226.29	224.03	216.58	216.07
72662	CL	264.94	254.69	236.17	227.89	226.65	219.1	219.87
	PP	264.14	252.25	235.87	228.10	226.56	219.11	219.81
	OBS	272.88	261.60	239.34	225.72	224.09	209.68	211.33
72425	CL	279.22	263.19	240.52	229.05	226.75	215.92	219.15
	PP	278.85	263.39	241.54	229.71	226.56	215.76	218.96
	OBS	254.67	251.69	233.50	224.03	223.07	213.95	214.04
72645	CL	266.79	254.86	238.04	229.37	226.56	218.04	219.55
	PP	266.71	254.88	238.17	229.41	226.56	218.04	219.55
	OBS	266.62	258.86	239.20	227.09	229.67	210.43	213.76
76394	CL	274.99	265.63	240.94	229.53	226.56	215.58	218.8
	PP	273.80	259.59	239.55	229.12	226.56	215.58	218.79
	OBS	259.51	257.86	236.37	224.81	230.39	210.93	214.66
72255	CL	268.23	259.56	240.49	230.25	226.99	218.33	219.92
	PP	268.51	258.37	241.62	231.79	226.56	218.22	219.72

data. Upon finding a linear operator which will yield a minimum mean square deviation of the predicted temperature profile from the true temperature profile in a statistical sense, the predicted temperature profile may be obtained. The linear operator, called the predictor matrix, may be expressed in terms of a covariance matrix, which can be constructed experimentally by collecting coincidences of radiances derived from remote sounders with temperature values obtained from direct soundings. In the microwave region, where the surface emissivity varies significantly with land and ocean, it is desirable to remove its effect on the temperature retrieval program so that the predictor matrix could be constructed over all surfaces. This can be done by utilizing the surface channel (Rigone and Strogryn, 1977).

Preliminary results using the statistical method over ocean surfaces are quite good (Captain Joe Gahlinger, personal communication) and a similar method is being research by the National Weather Service. Temperature profile retrievals over land, however, continue to pose problems. As shown by Nipko (1979) using theoretical data, the retrieved temperature profile suffers severe degradation in the presence of precipitating clouds. Precipitating areas may be eliminated quite easily over ocean surfaces. Recall Fig. 12, the 50.50 GHz frequency over a simulated ocean surface with $\varepsilon=.51$. If the window channel brightness temperature is higher than a certain threshold value, there must be a precipitating cloud within the field of view. Over land surfaces, partly because of the variability in the surface emissivity, it is difficult to discern which clouds are precipitating and which are not. An additional point that should be made is that generally

meteorologists and their numerical models would prefer to have temperature profile information in the vicinity of active weather producing storms, precisely the areas that appear to pose difficulties. With these thoughts in mind, the statistical method was applied to the known clear, cloudy and precipitating cases presented earlier in this chapter in hope of shedding further light on the temperature profile recovery problem over land.

The statistical method was applied to the cases studied and the results are presented in Figs. 40 through 42 for four clear, cloudy and precipitating cases. The model yields atmospheric temperatures for mandatory pressure levels of 1000, 850, 700, 500, 400, 300, 250, 150, 100, 70, 50, 30, 20, and 10 mb, thicknesses between the mandatory levels, and the temperature and pressure of the tropopause. The heights of the mandatory levels are computed by stacking the thicknesses onto a forecast 1000 mb height field retrieved from the AFGWC computer system. In these studies the 0000 Zulu height field on the appropriate day was used for stacking purposes.

Figure 40 shows the retrieved temperature profiles for the four clear cases; two on 30 October 1979 and two on 23 November 1979. Except for the Greensboro case, the retrieved temperature profiles when they are compared with nearby radiosonde data appear to be reasonably good in view of the statistical method used. The failure in the retrieval for the Greensboro case seems largely due to the fluctuated temperature profile that occurred in the atmosphere. Generally, we found that the statistical method is working properly when the actual profile is smooth and when no inversion is present. The retrieved temperature profiles under cloudy conditions are illustrated
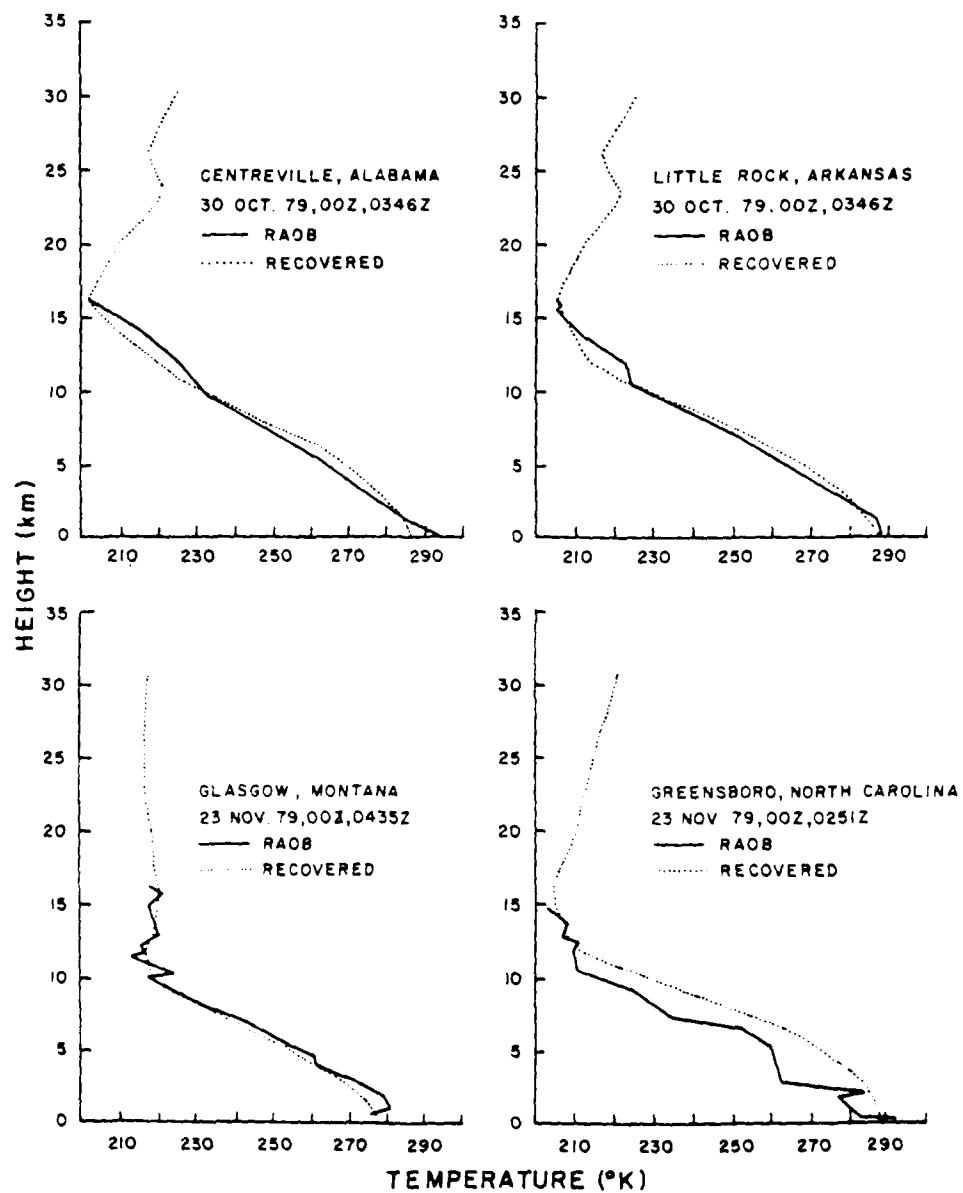
Figure 40. AFGWC statistical temperature retrievals - clear cases.
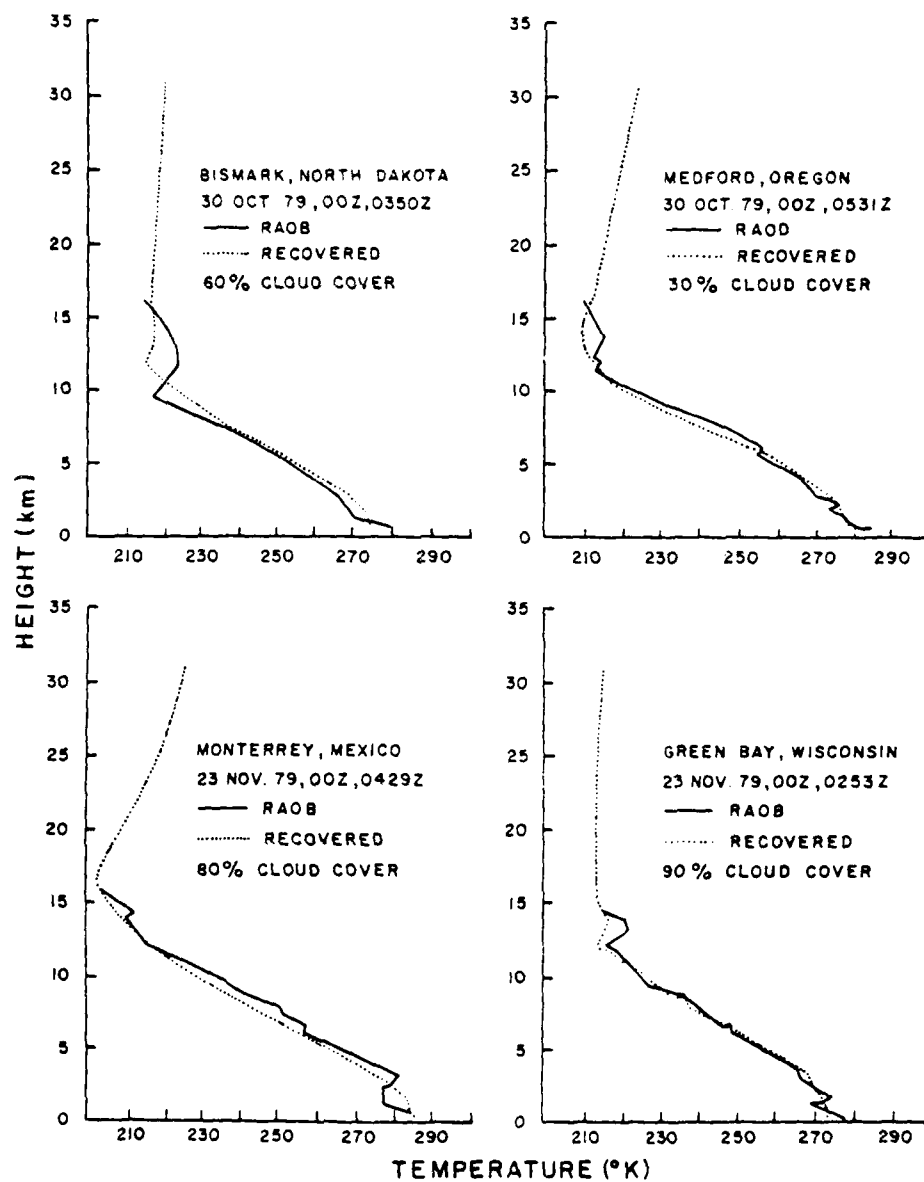
Figure 41. AFGWC statistical temperature retrievals - cloudy cases.
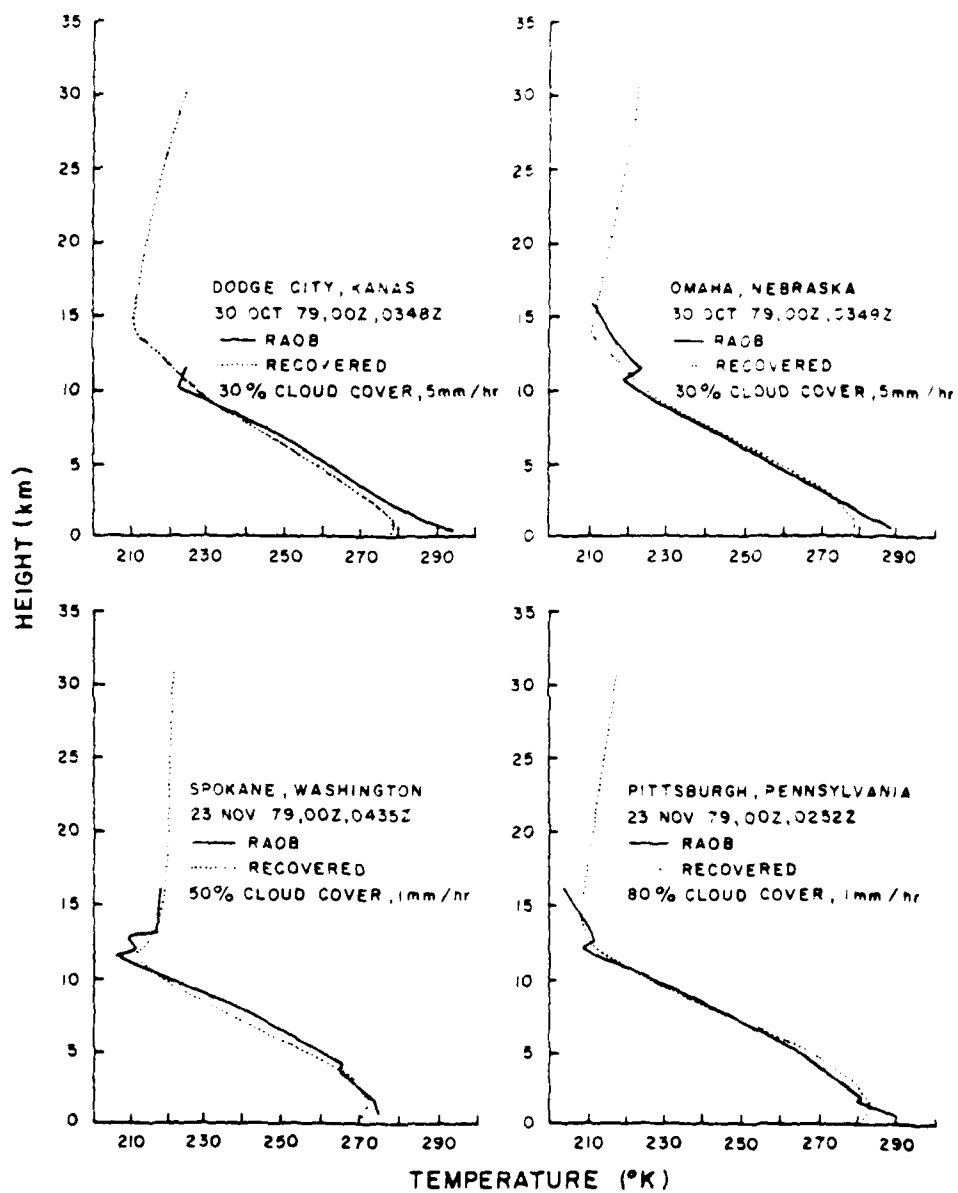
Figure 42. AFGWC statistical temperature retrievals - precipitating cases.

in Fig. 41. Apparently, the temperature profile retrieval program
using the microwave frequencies in the 60 GHz oxygen band is affected
insignificantly by non-precipitating clouds. Compared with the tem-
perature obtained from radiosondes, the retrieved patterns involving
clouds are similar to those under clear conditions. Note that in each
diagram, the percentage of cloud cover is depicted. Generally, the
retrieved and observed (radiosonde) temperatures in clear and cloudy
conditions are within about 5° K. In the final figure (Fig. 42) we
show the retrieved temperature profiles under precipitating conditions.
Again, four cases are presented in this study. Two cases are selected
from 30 October 1979; both have a 5 mm/hr rainfall rate with 30% cloud
cover in the field of view of the SSM/T. In the other two cases,
selected from 23 November 1979, both indicate a 1 mm/hr rainfall rate
but with cloud covers varying from 50% to 80%. The most distinct
feature in the retrieved temperature profiles using the statistical
covariance method for precipitating cases is the significant and con-
sistent deviation from the radiosonde data in the lower boundary layer
where precipitation takes place. In the moderate 5 mm/hr rainfall rate
cases, the differences between the retrieved and radiosonde temperature
profiles near the surface are as large as 10 - 15° K. It should be
noted that precipitation in these two cases cover only about 30% within
the field of view of SSM/T. As for the cases involving 1 mm/hr rain-
fall rate, about 5 - 10° K differences near the ground are observed.

The findings for these precipitation cases using the real SSM/T
data are in general agreement with those described by Nipko (1979) who
performed hypothetical temperature retrieval exercises. In Nipko's
analyses, a plane-parallel microwave radiative transfer model was used

to simulate the brightness temperature at the top of the atmosphere. He assumed a 2 km thick cloud with rainfall rates ranging from 1 mm/hr to 30 mm/hr and used the simulated brightness temperatures from seven SSM/T channels to recover the temperature profile also utilizing the statistical covariance method. The surface temperatures are shown to suffer increased degradation from 10° to 20° K as the rainfall rate increases from 1 mm/hr to 10 mm/hr. The hypothetical analysis that he has carried out, of course, assumes that the cloud covers the entire field of view.

Although the current study employs only four precipitating cases in the analysis and may not be conclusive in view of the limited sample used, it appears that the effect of precipitation on the temperature profile retrieval using microwave frequencies is substantial and significant. Of course, the reliability of the statistical method for the temperature profile retrieval in clear atmospheres should be examined comprehensively and completely utilizing the data that are available in different localities and seasons. In addition, in order to derive the temperature field over the global space, further studies concerning the influence of precipitating clouds on the temperature retrieval in the microwave region seem also warranted.

CHAPTER 8

CONCLUSION

A two-dimensional cylindrical cloud model was constructed for
the purpose of investigating radiative transfer in a finite cloud in
hypothetical and realistic atmospheres. Sensitivity tests were car-
ried out in the infrared 10 um window and the 50-60 GHz microwave re-
gions and results were compared with previous research. In addition,
actual atmospheric case studies were selected from two days and com-
parisons made among the calculated brightness temperature values gen-
erated by the cylinder model and a plane-parallel model, and the
brightness temperatures observed by the SSM/T microwave sounder.
Finally, temperature retrievals were performed using the AFGWC sta-
tistical method and these retrieved profiles were compared to radio-
sonde observations.

In the development of the cylinder model it was found that due
to the properties of the modified Bessel functions, higher order
spherical harmonic approximations to the radiative transfer equation
could be generated. This may be an advantage over the finite cubic
and rectangular cloud models, since it may be difficult to obtain
approximations of greater accuracy than first order.

Comparisons among cubic, plane-parallel and cylinder cloud
models in the 10 um infrared window were made. Emergent intensities
at the cloud top and bottom were presented and it was noted that the

finite cloud models produced zenith and nadir solutions that were larger and smaller, respectively, then the plane-parallel model. Next, a weighted average intensity algorithm was constructed to approximate an observed value at a far distance. Key points gathered from this analysis included the effects of the order of approximation employed in the various models and the manner in which multiple scattering and emission within a finite cloud manifest themselves in increasing amounts of energy emerging from the cloud sides as the cloud optical depth is increased. Finally, an analysis of cloud emissivity indicated that optically thick finite clouds in the 10 μm region may not be considered as black clouds because their emissivity values approach a value less then 1. This indicated that cloud top temperatures of finite clouds may be inferred to be too large in the 10 μm window region.

· Calculations were also performed in a realistic atmosphere by placing the cylinder cloud model in a plane-parallel absorbing and emitting atmosphere. Comparisons were made with the plane-parallel model in the DMSP SSM/T microwave frequencies. Both cloud models behaved in a similar fashion although there were some differences in response noted, especially at smaller optical depths. A weighted average intensity study in the microwave region was conducted. As expected from the results seen in the infrared study, the weighted average intensity leaving the cloud at observation angles greater than 60° increased strongly as the cloud optical depth increased. This was again attributed to the increased effects of multiple scattering and emission within the cloud. Also, multiple scattering effects in the SSM/T frequencies were shown to be significant.

Continuing, an analysis of the cloud solution with a zero incident intensity distribution was carried out. It was found that the cylindrical cloud, in this case, emits isotropically. Finally, cloud emissivity at 50.50 GHz was presented versus cloud optical depth. Although the same trends were exhibited as were seen in the infrared study the cloud emissivity was lower in value for all approximations in the microwave region.

Case studies were performed utilizing DMSP SSM/T sounder data in conjunction with standard meteorological data. Cases were divided into clear and cloudy/precipitating studies. In the clear atmosphere cases, two methods were presented for estimating the surface emissivity. A method utilizing the window channel was employed to estimate the emissivity, and clear column calculations were performed and compared to observed values of brightness temperature. With the exception of 53.20 GHz, calculated values of brightness temperature for clear cases were shown to be larger than observed values. This may be attributed to a systematic error in the source function as it is applied to the remote sensing problem. The 53.20 GHz results are considerably influenced by the Earth's surface. It was conjectured that the surface temperature was underestimated since temperatures reported at standard meteorological instrument shelter heights are not representative of the radiating temperature of the Earth's surface. This surface effect error may balance the source function error in surface-sensitive channels.

Cloudy/precipitating cases were compared with cylinder and plane-parallel model calculations. Calculations in cloudy conditions were used to generate scatter diagrams that were similar to the clear

cases and it was deduced that non-precipitating clouds have very little effect on microwave radiative transfer. Calculations in precipitating conditions were used to generate scatter diagrams that demonstrated the advantages of the cylinder model over the plane-parallel model. Results for both models were reasonable for cases with rainfall rates estimated at 1 mm/hr. For the two cases with a rainfall rate estimated at 5 mm/hr, the plane-parallel model failed while the cylinder model was quite reasonable. These differences were attributed to the model's geometries. It was interesting to note that the greatest failure of the plane-parallel model happened when the precipitating cloud system modeled was most cylinder like.

Finally, an exercise in temperature retrieval was performed using the AFGWC statistical method. Here it was demonstrated that precipitating conditions cause a consistent deviation of the retrieved temperature profile from the observed radiosonde temperature profile in the lower boundary layer - as much as 15° K in 5 mm/hr rainfall rates covering only 30% of the field of view.

APPENDIX

To carry out the operation indicated in Eqs. (5-18) and (5-58), the expansions for the intensity, Eq. (5-11), and for the phase function, Eq. (5-10), are substituted into Eq. (5-17). In this instance, however, we use the two-dimensional representation for intensity, $I(\vec{r},\vec{\Omega})$. Multiplying by the complex conjugate of the spherical harmonic and integrating, Eq. (5-17) may be represented as

$$\int_{4\pi} - \frac{1}{\beta_e} \sin\theta\cos\phi \frac{\partial}{\partial r} \left[\sum_{\ell=0}^{\infty} \sum_{m=-\ell}^{\ell} I_\ell^m(r,\phi_r) Y_\ell^m(\vec{\Omega}) \right] Y_\alpha^{\beta*}(\vec{\Omega}) d\Omega +$$

$$\int_{4\pi} \frac{1}{\beta_e r} \sin\theta\sin\phi \frac{\partial}{\partial\phi r} \left[\sum_{\ell=0}^{\infty} \sum_{m=-\ell}^{\ell} I_\ell^m(r,\phi_r) Y_\ell^m(\vec{\Omega}) \right] Y_\alpha^{\beta*}(\vec{\Omega}) d\Omega =$$

$$\int_{4\pi} \sum_{\ell=0}^{\infty} \sum_{m=-\ell}^{\ell} \left[I_\ell^m(r,\phi_r) Y_\ell^m(\vec{\Omega}) \right] Y_\alpha^{\beta*}(\vec{\Omega}) d\Omega -$$

$$- \frac{\tilde{\omega}_\nu}{4\pi} \int_{4\pi} \int_{4\pi} \sum_{\ell=0}^{\infty} \sum_{m=-\ell}^{\ell} \left[I_\ell^m(r,\phi_r) Y_\ell^m(\vec{\Omega}') \right] \left[\omega_\ell Y_\ell^{m*}(\vec{\Omega}') Y_\ell^m(\vec{\Omega}) \right] d\Omega' Y_\alpha^{\beta*}(\vec{\Omega}) d\Omega$$

$$+ (1-\tilde{\omega}_\nu) \int_{4\pi} B_\nu(T) Y_0^0(\vec{\Omega}) Y_\alpha^{\beta*}(\vec{\Omega}) d\Omega \qquad (A-1)$$

The integrations on the right hand side of Eq. (A-1) may be done straightforwardly. To accomplish the left hand side, the recursion formula, Eqs. (5-15) and (5-16), may be added to produce the term $\sin\theta\cos\phi Y_\ell^m(\vec{\Omega})$, and subtracted to produce $\sin\theta\sin\phi Y_\ell^m(\vec{\Omega})$. The details of the $\sin\theta\sin\phi Y_\ell^m(\vec{\Omega})$ are presented here. First, the constant of integration from the right hand side is multiplied through the equation,

and we may write the term as

$$-\frac{2\alpha-1}{4\pi} \int\limits_{\vec{\Omega}} \frac{1}{\beta_e r} \sin\theta\sin\phi \frac{\partial}{\partial\phi_r} [\sum\sum I_\ell^m(r,\phi_r)Y_\ell^m(\theta,\phi)]Y_\alpha^{\beta*}(\vec{\Omega})d\vec{\Omega}$$

$$(A\text{-}2)$$

Now dissect a portion of this expression as

$$-\frac{\partial}{\partial\phi_r} I_\ell^m(r,\phi_r)Y_\ell^m(\theta,\phi_r-\phi_r) =$$

$$[+ im Y_\ell^m(\vec{\Omega})I_\ell^m(r,\phi_r) - Y_\ell^m(\vec{\Omega})\frac{\partial}{\partial\phi_r} I_\ell^m(r,\phi_r)] . \qquad (A\text{-}3)$$

Inserting Eq. (A-3) into Eq. (A-2) and rearranging, we have

$$-\frac{2\alpha+1}{4\pi} \int\limits_{\vec{\Omega}} \sum\sum \frac{1}{\beta_e r} \sin\theta\sin\vec{\phi}[Y_\ell^m(\vec{\Omega}) \frac{\partial}{\partial\phi_r} I_\ell^m(r,\phi_r)]Y_\alpha^{\beta*}(\vec{\Omega})d\vec{\Omega}$$

$$+\frac{2\alpha+1}{4\pi} \int\limits_{\vec{\Omega}} \sum\sum \frac{1}{\beta_e r} \sin\theta\sin\vec{\phi}[I_\ell^m(r,\phi_r)(im)Y_\ell^m(\vec{\Omega})]Y_\alpha^{\beta*}(\vec{\Omega})d\vec{\Omega}$$

$$(A\text{-}4)$$

Looking only at the first term in Eq. (A-4), we see we have the factor $\sin\theta\sin\phi Y_\ell^m(\vec{\Omega})$ which we have noted can be expressed by subtracting the recursion formula and dividing by 2i. After performing the subtraction we note there are four portions which we write out separately.

Part A is

$$-\frac{2\alpha+1}{4\pi} \int\limits_{\vec{\Omega}} \sum\sum \frac{1}{\beta_e r} \{ \frac{1}{2i} \frac{1}{2\ell+1} (\ell-m-1)^{1/2}(\ell-m)^{1/2} Y_{\ell-1}^{m-1}(\vec{\Omega}) \} Y_\alpha^{\beta*}(\vec{\Omega})$$

$$\cdot \frac{\partial}{\partial\phi_r} I_\ell^m(r,\phi_r)d\vec{\Omega}$$

which may be written as

VITA

Name	Grant Clifford Aufderhaar
Birthdate	August 20, 1948
Birthplace	Celina, Ohio
High School	Memorial High School St. Mary's, Ohio
Universities	United States Air Force Academy Colorado 1966-1970
	Texas A & M University College Station, Texas 1971-1972
	University of Utah Salt Lake City, Utah 1977-1980
Degrees	B. S., 1970 United States Air Force Academy Colorado
	M. S., 1972 Texas A & M University College Station, Texas
Professional and Honorary Societies/Memberships	American Meteorological Society CHI Epsilon PI PHI Kappa PHI
Publications	"Remote Sounding of Cloud Composi- tions from NOAA IV and Nimbus VI Infrared Sounders," 1977 with K. N. Liou, R. G. Feddes and T. L. Stoffel. AFGL-TR-77-0252.

$$= - \frac{1}{i\beta_e r} \ \frac{1}{2(2\alpha+3)} \ (\alpha-\beta+1)^{1/2} \ (\alpha-\beta+2)^{1/2} \ \frac{\partial}{\partial\phi_r} \ I^{\beta-1}_{\alpha+1} \ (r,\phi_r) \ .$$

Part B is

$$= \ \frac{1}{i\beta_e r} \ \frac{1}{2(2\alpha-1)} \ (\alpha+\beta-1)^{1/2} \ (\alpha+\beta)^{1/2} \ \frac{\partial}{\partial\phi_r} \ I^{\beta-1}_{\alpha-1} \ (r,\phi_r) \ .$$

Part C is

$$= + \frac{1}{i\beta_e r} \ \frac{1}{2(2\alpha-1)} \ (\alpha-\beta-1)^{1/2} \ (\alpha-\beta)^{1/2} \ \frac{\partial}{\partial\phi_r} \ I^{\beta+1}_{\alpha-1} \ (r,\phi_r) \ .$$

Part D is

$$= - \frac{1}{i\beta_e r} \ \frac{1}{2(2\alpha+3)} \ (\alpha+\beta+1)^{1/2} \ (\alpha+\beta+2)^{1/2} \ \frac{\partial}{\partial\phi_r} \ I^{\beta+1}_{\alpha+1} \ (r,\phi_r) \ .$$

The second term in Eq. (A-4) also has four portions which may be written

Part A

$$= \frac{2\alpha+1}{4\pi} \int_{\vec{\Omega}} \Sigma\Sigma \frac{im}{\beta_e r} \{ \frac{1}{2i} \frac{1}{2\ell+1} (\ell-m-1)^{i/2} (\ell-m)^{1/2} Y^{m-1}_{\ell-1} (\vec{\Omega}) \}$$

$$\cdot \ Y^{\beta}_{\alpha}(\vec{\Omega}) I^m_{\ell}(r,\phi_r) d\vec{\Omega}$$

which reduces to

$$= \frac{(\beta-1)}{\beta_e r} \ \frac{1}{2(2\alpha+3)} \ (\alpha-\beta+1)^{1/2}(\alpha-\beta+2)^{1/2} \ I^{\beta-1}_{\alpha+1} \ (r,\phi_r) \ .$$

Part B is

$$= -\frac{(\beta-1)}{\beta_e r} \frac{1}{2(2\alpha-1)} (\alpha+\beta-1)^{1/2} (\alpha+\beta)^{1/2} I_{\alpha-1}^{\beta-1} (r,\phi_r)$$

Part C is

$$= -\frac{(\beta+1)}{\beta_e r} \frac{1}{2(2\alpha-1)} (\alpha-\beta-1)^{1/2} (\alpha-\beta)^{1/2} I_{\alpha-1}^{\beta+1} (r,\phi_r)$$

Part D is

$$= \frac{\beta+1}{\beta_e r} \frac{1}{2(2\alpha+3)} (\alpha+\beta+1)^{1/2} (\alpha+\beta+2)^{1/2} I_{\alpha+1}^{\beta+1} (r,\phi_r)$$

Combining the first and second terms in Eq. (A-4), and the $\sin\theta\cos\phi$ terms, and defining A_α^β, B_α^β, C_α^β, D_α^β as before, we arrive at Eq. (5-59). Note that if the intensity, $I(\vec{r},\vec{\Omega})$ is reduced to the one-dimensional case, $I(r,\vec{\Omega})$, then the $\frac{\partial I}{\partial \phi_r}$ term is zero and Eq. (5-59) reduces to Eq. (5-19).

REFERENCES

Arfken, G., 1970: Mathematical Methods for Physicists. New York, Academic Press, 815 pp.

Barrett, A. H. and V. K. Chung, 1962: A method for the determination of high-altitude water vapor abundance from ground-based microwave observations. J. Geophys. Res., 67, 4259-4266

Becker, G. E. and S. H. Autler, 1946: Water vapor absorption of electromagnetic radiation in the centimeter wave-length region. Phys. Rev., 70, 388-398.

Case, K. and P. Zwiefel, 1967: Linear Transport Theory. Reading, Mass., Addison-Wesley Publ. Co., 342 pp.

Chandrasekhar, S., 1950: Radiative Transfer. New York, Dover Publ., 393 pp.

Clark, M. and K. Hansen, 1964: Numerical Methods of Reactor Physics. New York, Academic Press, 340 pp.

Dave, J. V., 1975: A direct solution of the spherical harmonics approximation to the radiative transfer equation for an arbitrary solar elevation. Part 1: Theory. J. Atmos. Sci., 32, 790-798.

_____, 1975: A direct solution of the spherical harmonics approximation to the radiative transfer equation for an arbitrary solar elevation. Part II: Results. J. Atmos. Sci., 32, 1463-1474.

Dave, J. V. and José Canosa, 1974: A direct solution of the radiative transfer equation: Application to atmospheric models with arbitrary vertical nonhomogenieties. J. Atmos. Sci., 31, 1089-1101.

Davies, R., 1978: The effect of finite geometry on the three-dimensional transfer of solar irradiance in clouds. J. Atmos. Sci., 35, 1712-1725.

Davis, J., S. K. Cox and T. McKee, 1979: Vertical and horizontal distributions of solar absorption in finite clouds. J. Atmos. Sci., 36, 1976-1984.

Davison, B., 1957: Sperical harmonics method for neutron transport problems in cylindrical geometry. Can. Jour. of Phys., 35, 576-593.

Diem, M. 1948: Messungen der Grösse von wolkenelementen, II. Met. Rdsch., 1, pp 261.

Diermendjian, D., 1969: Electromagnetic Scattering on Spherical Polydispersions. New York, Elsevier Press, 75-78.

Dunn, R., 1966: Descriptive Micrometeorology. New York, Academic Press, 245 pp.

Falcone, V., 1979: Absorption coefficient programs. (Private communication).

Feddes, R. and K. N. Liou, 1977: Sensitivity of upwelling radiance in Nimbus 6 HIRS channels to multilayered clouds. J. Atmos. Sci. 82, 5977-5989.

Gelbard, E. M., 1968: Spherical harmonics method: P_e and double-P_e approximations. Computing Methods in Reactor Physics, H. Greenspan, et. al., Eds. New York, Gorden and Breach, 271-358.

Gloersen, P., T. Wilheit and T. Schmugge, 1972: Microwave emission measurements of sea surface roughness, soil moisture, and sea ice structure. Fourth Annual Earth Resources Program Review, NASA Programs, Goddard Space Flight Center, Greenbelt Maryland, 8-1, 8-19.

Goertzel, G. and N. Tralli, 1960: Some Mathematical Methods of Physics. New York, McGraw-Hill, 300 pp.

Greenspan, H., C. N. Kelber and T. Okrent, 1968: Computing Methods in Reactor Physics. New York, Gordon and Breach, 589 pp.

Heaslet, M. and R. F. Warming, 1966: Theoretical predictions of radiative transfer in a homogeneous cylindrical medium. J. Quant. Spectrosc. Radiat. Transfer, 6, 751-774.

Heasley, J. N., 1977: Radiative transfer in cylindrical media. J. Quant. Spectrosc. Radiat. Transfer, 18, 541-547.

Hollinger, J. P., 1973: Microwave Properties of a Calm Sea. Naval Research Laboratory Report No. 7110-2, Washington, D. C., 69 pp.

King, G. W., et. al., 1947: Effective microwave absorption coefficients of water and related molecules. Phys. Rev., 71, 433-443.

Liou, K. N., 1973: A numerical experiment on Chandrasekhar's discrete-ordinate method for radiative transfer: Applications to cloudy and hazy atmospheres. J. Atmos. Sci., 30, 1303-1326.

_____, 1975: Applications of the discrete-ordinate method for radiative transfer to inhomogeneous aerosol atmospheres. J. Atmos. Sci., 80, 3434-3440.

_____, 1976: On the absorption, reflection, transmission of solar radiation in cloudy atmospheres. *J. Atmos. Sci.*, *33*, 798-805.

Liou, K. N., R. G. Feddes, T. L. Stoffel, and G. C. Aufderhaar, 1977: *Remote Sounding of Cloud Compositions from NOAA IV and Nimbus VI Infrared Sounders*. AFGL-TR-77-0252, 99 pp.

Liou, K. N. and S. C. Ou, 1979: Infrared radiative transfer in finite cloud layers. *J. Atmos. Sci.*, *36*, 1985-1996.

McKee, T. B. and S. K. Cox, 1976: Scattering of visible radiation by finite clouds. *J. Atmos. Sci.*, *31*, 1885-1892.

Mark, C., 1957: *The Spherical Harmonics Method, I.* CRT-340 (revised), Chalk River, Ontario, 45 pp.

_____, 1957: *The Spherical Harmonics Method, II.* CRT-338 (revised), Chalk River, Ontario, 96 pp.

Marshak, R. E., 1947: Note on the spherical harmonic method as applied to the Milne problem for a sphere. *Phys. Rev.*, *71*, 443-446.

Marshall, J. S. and W. M. Palmer, 1948: The distribution of raindrops with size. *J. Meteor.*, *5*, 165-166.

Mason, B. J., 1971: *The Physics of Clouds*. Oxford, Clarendon Press, p. 108.

Meeks, M. L. and A. E. Lilley, 1963: The microwave spectrum of oxygen in the Earth's atmosphere. *J. Geophys. Res.*, *68*, 1683-1703.

Mie, G., 1908: Beiträge zur optik trüben medien, speziell kolloidaler mettallösungen. *Ann,d. Phys.*, *25*, 377-445.

Nipko, P., 1979: *Effects of Precipitating and Nonprecipitating Cloud Layers on DMSP Microwave Temperature Sounder*. Master's Thesis, Univ. of Utah, Salt Lake City, Utah, 85 pp.

Ou, S. C., 1979: Numerical Integration of Spherical Harmonic Combinations. (Private communications).

Pomraning, G. C., 1964: Variational boundary conditions for the spherical harmonics approximation to the neutron transport equation. *Ann. of Phys.*, *27*, 193-215.

Powers, D., 1972: *Boundary Value Problems*. New York, Academic Press, 238 pp.

Rigone, J. L. and A. P. Stogryn, 1977: Data processing for the DMSP microwave radiometer system. *Eleventh International Symposium on Remote Sensing of the Environment,* Univ. of Michigan Press, 1-9.

Rosenblum, E. S., 1961: Atmospheric absorption of 10-400 Kmcps radiation: summary and bibliography to 1961. *Microwave J.,* 4, 91-96.

Savage, R. C., 1976: The Transfer of Thermal Microwaves Through Hydrometeors. Doctor of Philosophy (Meteorology) Dissertation, Univ. of Wisconsin-Madison, 147 pp.

Saxton, J. A. and J. A. Lane, 1952: Electrical properties of sea water: reflection and attenuation characteristics at v.h.f. *Wireless Engineer,* 29, 269-275

Schmugge, T., et. al., 1974: Remote sensing of soil moisture with microwave radiometers. *J. Geophys. Res.,* 79, 317-323.

Sekhon, R. S. and R. C. Srivastaval, 1970: Snow size spectra and radar reflectivity. *J. Atmos. Sci.,* 27, 299-307.

Sobolev, V., 1975: *Light Scattering in Planetary Atmospheres.* New York, Pergamon Press, 254 pp.

Staelin, D. H., et. al., 1975: Microwave atmospheric temperature sounding: effects of clouds on Nimbus 5 satellite data. *J. Atmos. Sci.,* 32, 1970-1976.

Van Vleck, J. H., 1947: The absorption of microwaves by oxygen. *Phys. Rev.,* 71, 413-424.

Waters, J. W., et. at., 1975: Remote sensing of atmospheric temperature profiles with the Nimbus 5 microwave spectrometer. *J. Atmos. Sci.,* 32, 1953-1969.

Wienberg, A. and E. Wigner, 1958: *The Physical Theory of Neutron Chain Reactors.* Chicago, Univ. of Chicago Press, 810 pp.

Weinman, J. A. and R. Davies, 1978: Thermal microwave radiances from horizontally finite clouds of hydrometeors. *J. Geophys. Res.,* 83, 3099-3108.

END

DATE
FILMED

1-81

DTIC